15th Symposium SiO2, Advanced Dielectrics and Related Devices

Cité du Design, Saint-Etienne (France)

June 23-26th, 2025

Book of Abstracts

Symposium Committees

Symposium Chairs

- Aziz Boukenter, University of Saint-Etienne (UJM), France
- Youcef Ouerdane, University of Saint-Etienne (UJM), France

Organizing Committee

- Antonino Alessi, CEA - University of Palermo, France, Italy
- Hugo Boiron, Exail, France
- Patrice Crochet, Exail, France
- Maxime Darnon, UJM, France
- Matteo Ferrari, UJM, France
- Fiammetta Fricano, UJM, France
- Sylvain Girard, UJM, France
- Emmanuel Marin, UJM, France
- Adriana Morana, UJM, France
- Luca Weninger, UJM, France

Scientific Committee

- Simonpietro Agnello, University of Palermo, Italy
- Antonino Alessi, CEA - University of Palermo, France, Italy
- Jean-Luc Autran, Aix-Marseille University, France
- Mourad Benabdesselam, University of Nice Sophia Antipolis, France
- Thomas Blanchet, CEA, Saclay, France
- Hugo Boiron, Exail, France
- Mohamed Bouazaoui, University of Lille, France
- Aziz Boukenter, University of Saint Etienne, France
- Marco Cannas, University of Palermo, Italy
- Bruno Capoen, University of Lille, France
- Carlo Maria Carbonaro, University of Cagliari, Italy
- Hicham El Hamzaoui, University of Lille, France
- Marc Gaillardin, CEA-DAM-DIF, Arpajon, France
- Franco Gelardi, University of Palermo, Italy
- Luigi Giacomazzi, CNR, Trieste
- Sylvain Girard, University of Saint Etienne, France
- Anne Heymerick, LAAS, Toulouse, France
- Nourdine Kerboub, CNES, Toulouse, France
- Ayoub Ladaci, CEA, Saclay, France
- Damien Lambert, CEA DAM, France
- Mathieu Lancry, University of Paris-Sud, France
- Franck Mady, University of Nice Sophia Antipolis, France
- Layla Martin-Samos, CNR, Trieste, Italy
- Gilles Mélin, Exail, France
- Franco Meinardi, University of Milano-Bicocca, Italy
- Luciano Mescia, Politecnico di Bari, Italy
- Fabrizio Messina, University of Palermo, Italy

- Adriana Morana, University of Saint-Etienne, France
- Nadège Ollier, Ecole Polytechnique, Palaiseau, France
- Youcef Ouerdane, University of Saint Etienne, France
- Philippe Paillet, CEA-DAM-DIF, Arpajon, France
- Alberto Paleari, Università Milano Bicocca, Italy
- Bertrand Poumellec, University of Paris-Sud, France
- Francesco Prudenzano, Politecnico di Bari, Italy
- Pier Carlo Ricci, University of Cagliari, Italy
- Nicolas Richard, CEA-DAM-DIF, Arpajon, France
- Thierry Robin, Exail, Lannion, France
- Alexandre Shluger, University College, London, UK
- Linards Skuja, University of Latvia, Latvia
- Andrea Stesmans, University of Leuven, Belgium
- Anatoly Trukhin University of latvia, Latvia
- Anna Vedda, University of Milano-Bicocca, Italy
- Marilena Vivona, CNR, Catania, Italy
- Anatoly Fedorovich Zazsepin, Ural Federal University, Russia

A RADECS-sponsored Short Course
Multi-Scale, Multiphysics of Advanced Materials for Photonics and Microelectronics

June the 23rd, 2025, Campus Manufacture, Room D03 (Bâtiment D)

8:30 – 9:40	**Opening of Short Course**
Session 1: *From silica glasses to new materials* **(Chair: Youcef Ouerdane, Univ. Saint-Etienne, France)**	
8:40 – 9:30	**From silica to new materials** **Marco Cannas & Simonpietro Agnello, University of Palermo, Italy** Modern nanotechnologies have provided an important impetus for fundamental research on nanostructured systems that exhibit peculiar properties conferred by quantum confinement in the 0D, 1D and 2D dimensions, and by the high value of the specific surface area. Here we present an overview of the studies conducted on silica, i.e. a paradigmatic system for size-dependent properties, and on innovative materials such as graphene, 2D materials (MoS2, tansition metal dichalcogenides), ZnO and SiC, with modulable characteristics in multiple applications.
9:30 - 10:20	**Point defects in silica glass** **Linards Skuja, University of Latvia, Latvia** The impact of point defects on present-day applications of silica glass will be outlined. The principal differences between the nature of point defects in glass and crystal, and their peculiarities in silica glass, compared to other glasses will be discussed. An updated overview on the presently known point defects will be given and the still existing controversies will be addressed.
10:20 – 10 :50	**Break**
Session 2: *Experimental tools and techniques* **(Chair: Linards Skuja, Univ. Latvia)**	
10:50 – 11:30	**Unveiling Defects in Silica Glasses with Electron Paramagnetic Resonance** **Antonino Alessi, CEA, France / University of Palermo, Italy** The lecture illustrates the use of EPR a tool to investigate the defects in silica-based (SiO_2) glasses. EPR enables the detection and structural characterization of intrinsic and extrinsic paramagnetic defects in glasses and it has been largely used to study silica. The lecture will illustrate the main theoretical and practical aspects of this spectroscopic technique giving some example of how it has been or can be used.
11:30 – 12:10	**Steady-State Spectroscopic Techniques**

	Adriana Morana, Univ. Saint-Etienne, France The lecture focuses on the spectroscopic techniques that can be employed to study the electronic and vibrational levels of a molecule. Whereas Raman spectroscopy or Infrared Absorption give information about the structure of the material under test, Optical Absorption and Photoluminescence allow to characterize the optical properties of the material. With a confocal microscope, the spatial distribution of some of the centers in the sample can be also investigated.
12:10 – 12:50	**Reconstructing dynamics initiated by photo-excitation on the nanosecond and femtosecond time scales** **Fabrizio Messina, Univ. Palermo, Italy** The lecture will focus on the use of time-resolved spectroscopic methods, ranging from the nanosecond to the femtosecond scale, to gain information of the characteristic relaxations of solid-state or liquid phase physical systems photo-excited by short pulses of light.
12 :50 – 14 :00	**Break**
Session 3: ***Theoretical tools and techniques*** **(Chair: Nicolas Richard, CEA DAM, France)**	
14:00 – 14:40	**Radiation matter interactions in photonics and microelectronics: theory and tools** **Damien Lambert, CEA DAM, France** In this course, after a brief description of the radiative environments of interest, we introduce the main mechanisms induced during irradiation in materials for photonics and microelectronics, according to the different particles classically encountered. The various methods and numerical tools for simulating these effects are presented.
14:40 – 15:20	**Addressing Defect spectroscopic signatures, formation and interconversion mechanisms: Understanding, modelling and predicting** **Layla Martin Samos, CNR-IOM, Italy** Defects lie at the very heart of modern technology. Whether they're introduced intentionally, sneak in during manufacturing, or emerge under real-world operating conditions, defects play a decisive role in shaping the opto-electronic behavior of semiconductors and insulators. They can boost free-carrier generation, act as efficient recombination centers, serve as pesky charge traps, or even lend materials their color by absorbing and emitting light. Now, over 70 years after the invention of the silicon transistor—and even longer since the debut of silica-based optical fibers—you might think we've figured it all out. Add to that the explosion of High Performance Computing and the rise of "push-button" first-principles modeling, and you'd be forgiven for wondering: why are we still talking about defects? Shouldn't they be a solved problem by now? In this introductory lecture, we'll explore why the answer is a resounding no. We'll present a critical overview of the theoretical and computational frameworks currently used to model and understand defects and their spectroscopic fingerprints. Special

	emphasis will be placed on cutting-edge first-principles methods for predicting optical properties. Throughout, theory and experiment will be placed in direct dialogue—sometimes harmonious, sometimes not—to illuminate both progress and pitfalls in the quest to tame defects.
15:20 – 16:00	**Addressing Defect spectroscopic signatures, formation and interconversion mechanisms: sample applications in silica and silicon** **Layla Martin Samos, CNR-IOM, Italy** In the second part of the short course, we'll dive into practical examples showcasing how the optical fingerprints of defects in silicon and silica keep us computational folks gainfully employed. After all, when it comes to semiconductors and insulators, it's often the "dirt"—not the perfection—that makes things truly interesting.
16:30 – 17:10	**Atomic displacements induced by radiations in materials : simulation methods and basic mechanisms** **Thomas Jarrin, CEA DAM, France** The main methods to simulate atomic displacement induced by radiations are presented, their advantages and limits are clearly stated. The future challenges in the development of those methods are detailed, and insights into the basic mechanisms of defects creation following irradiation are presented for materials of interest for microelectronic applications.
Session 4: *Radiation Effects* (Chair: Aziz Boukenter, Univ. Saint-Etienne, France)	
17:10: – 17:50	**Radiation effects on microelectronics** **Ygor Aguiar, CERN, Switzerland** This course offers an overview of the fundamental concepts underlying radiation-induced failure mechanisms in electronic components operating in harsh environments, including space missions and particle accelerators. Topics will cover both stochastic effects, such as Single-Event Effects (SEEs), and cumulative dose effects. The course will also discuss mitigation strategies, including radiation-hardening-by-design (RHBD) and radiation-hardening-by-process (RHBP), providing insight into approaches for improving electronic system reliability in radiation environments.
17:50: – 18:30	**Radiation effects on optical fibers** **Sylvain Girard, Univ. Saint-Etienne, France** This lecture will discuss how the point defects generated by ionizing radiation in the silica layers constituting the optical fibers will affect their macroscopic properties and performance in harsh environments. We'll discuss how the understanding of those basic mechanisms of defect generation and recombination could be exploited to either improve the radiation hardness of fiber-based solutions or to design radiation sensitive fibers for radiation detection and dosimetry.
End of short course	

15th Symposium SiO2, Advanced Dielectrics and Related Devices

Tuesday, June 24, 2025

8:40 – 9:00	**Conference opening** - Introduction to the SiO2 2025 Conference **Youcef Ouerdane / Aziz Boukenter, Univ. Saint-Etienne**	
9:00 – 9:40	**Invited Talk** - Photoinduced modulation of Quantum Dot Superparticles on the ultrafast time scale - *Fabrizio Messina, Univ. Palermo* (Introduction: Youcef Ouerdane, Univ. Saint-Etienne)	
Session 1: Ultrafast Spectroscopy - **Youcef Ouerdane, Univ. Saint-Etienne**		
9:40 - 10:00	Time resolved mid-infrared absorption in silica: ultrafast heat transfer observed by direct probing of anharmonic vibration - *Vincenzo De Michele, Univ. Saint-Etienne*	p. 18
10:00 – 11:00	**Coffee Break**	
Session 2: Grating Functionalization of materials - **Emmanuel Marin, Univ. Saint-Etienne**		
11:00 – 11:20	Densification evaluation in femtosecond laser modified silica glass of types I, II and III - *Nadezhda Shchedrina, Univ. Paris Saclay*	p. 21
11:20 – 11:40	Enhancing Stability and Radiation Resilience of Narrowband Optical Filters for High Power and Space Applications - *Laurent Lablonde, Exail*	p. 23
11:40 – 12:00	Optical sensor based on a diffraction grating combined with a hydrogenated amorphous silicon layer - *Rosa Darell Olloghe Mandoukou, Univ. Saint-Etienne*	p. 25
12:00 - 13 :40	**Lunch Break**	
13:40 – 14 :20	**Invited Talk** - First-principles identification of paramagnetic centers in irradiated F-doped silica - *Luigi Giacomazzi, CNRS Trieste* - (Introduction: Layla Martin Samos, CNR-IOM)	
Session 3: Radiation induced point defects - **Nadège Ollier, LSI**		
14:20 – 14:40	EPR and optical studies of silica glass implanted by 12C+ and 13C+ ions - *Linards Skuja, Univ. Latvia*	p. 28

14:40 – 15:00	Photobleaching Effects Caused by Ambient Light on the Radiation-Induced Attenuation of Germanosilicate Optical Fibers - *Martin Roche, CEA*	p. 30
15:00 – 15:20	Temperature Effect on the Radiation Response of Graded Index Germanosilicate Multimode Optical Fibers - *Roberto Pecorella, Univ. Saint-Etienne*	p. 32
15:20 – 16:10	**Coffee Break**	
16:10 – 16:50	**Invited Talk** - 1L-MoS2 on SiO2 Photoluminescence Enhancement Via Post-Synthesis Thermal Treatments - *Antonino Madonia, Univ. Palermo* (Introduction: Simonpietro Agnello, Univ. Palermo)	
Session 4: Luminescence Spectroscopy - Marco Cannas, Univ. Palermo		
16:50 – 17:10	Multifunctional Lanthanide-doped Oxyfluoride Nanophosphors for Luminescence Thermometry and Latent Fingerprint Detection - *Hendrik Swart, University of the Free State*	p. 35
17:10 – 17:30	Sol-gel derived Luminescent Coatings Incorporating YVO4:Eu^{3+} Nanocrystals for Narrow-Red Emission - *Arjun Babu, Univ. Clermont*	p. 37
17:30 – 17:50	Optical Performances of Chromophores Embedded in Metal Organic Frameworks for Photonics in Harsh Environments - *Giuseppe Ficarra, Univ. Palermo*	p. 39
Wednesday, June 25, 2025		
8:30 – 9:10	**Invited Talk** - Scintillating sol-gel silica glasses and optical fibers for remote ionizing radiation dosimetry - *Bruno Capoen, Univ. Lille* (Introduction: Youcef Ouerdane, Univ. Saint Etienne)	
Session 5: Radioluminescence – Hugo Boiron, Exail		
9:10 - 9:30	Optical Fiber-based Dosimetry for 15 MeV Proton Beam Monitoring - *Fiammetta Fricano, CEA*	p. 42
9:30 – 9:50	Radiation-Induced Luminescence Study in Different Low-OH Pure Silica Core Optical Fibers - *Selyan Acid, CNES*	p. 44
9:50 – 10:10	Combined theoretical and experimental evaluation of the energy dependence of the radioluminescence phenomenon in Ce-doped optical fibers - *Luca Weninger, Univ. Saint-Etienne*	p. 46
10:10 – 11:00	**Coffee Break**	
Session 6: Advanced technologies and techniques - Philippe Paillet , CEA		
11:00 – 11:20	3D Printing of Silica-based Binary and Ternary Oxide Systems using Two-photon Polymerization - *Halima El Aadad, Univ. Lille*	p. 49

11:20 – 11:40	Bias-Dependent TID Effects and Annealing Recovery in Power COTS GaN HEMTs - *Hadrien Couillaud, CEA*	p. 51
11:40 – 12:00	Electric charges as an apparent governing parameter for electron induced stress relaxation in amorphous silica micropillar - *Guillaume Kermouche, Ecole des Mines*	p. 53
12 :00 - 13 :40	**Lunch Break**	
13 :40 – 14 :20	**Invited Talk** - Photosensitive oxide glass for direct 3D writing of integrated photonic components - *Yannick Petit, Université di Bordeaux* - (Introduction: Matteo Ferrari, Univ. Saint-Etienne)	
Session 7: RadioPhotoluminescence - **Antonino Alessi, CEA, Univ. Palermo**		
14:20 – 14:40	The need of new calibrations for high level dosimetry: Radiophotoluminescence FD-7 dosimeters irradiated with 6 MeV electrons - *Matteo Ferrari, Univ. Saint-Etienne*	p. 56
14:40 – 15:00	Sensitivity degradation and regeneration behavior in silver-doped RPL glass dosimeters under multiple thermal annealing cycles - *Ygor Aguiar, CERN*	p. 58
15:00 – 15:20	Impact of thermal annealing on radiation induced attenuation for radiophotoluminescence glass dosimeters at high X-ray doses - *Aditya Raj Mandal, Univ. Saint-Etienne*	p. 60
15:20 – 15:40	Monte Carlo Simulation dosimetry study of cylindrical FD-7 radiophotoluminescent dosimeters in different radiation environments - *Matilde Avesani, Univ. Saint-Etienne*	p. 62
Poster Session		
15:40 – 18:00	**P1**: Enhanced Spatially-Resolved Optical Fiber-Based Dosimetry Through Optical Frequency Domain Reflectometry (*J. Perrot, Univ. Saint-Etienne*)	p. 65
	P2: Exploiting the Yb2+ Ion Lifetime for Optical Fiber-Based Cryogenic Thermometry (*A. K. Alem, Univ. Saint-Etienne*)	p. 68
	P3: Feasibility of In Vivo Dosimetry in Contact Radiotherapy Using a Germanium-Doped Silica Optical Fiber (*G. Shumilov, Centre Hospitalier Princesse Grace*)	p. 70
	P4: Hybrid sol-gel waveguide sensor for damage detection in aerospace domain (*M. Royon, Univ. Saint-Etienne*)	p. 72
	P5: Influence of OH content and pre-irradiation on the radiation-induced luminescence of pure-silica-core optical fibers (*M. R. Coto Antunez, Univ. Saint-Etienne*)	p. 74

	P6: Optical fibers irradiation at the n_TOF NEAR station at CERN: a Monte Carlo simulation dosimetry study (*M. Avesani, Univ. Saint-Etienne*)	p. 76
	P7: Pulsed X-ray Radiation Responses of Single-Mode and Multimode Fluorine-doped Optical Fibers (*V. De Michele, Univ. Saint-Etienne*)	p. 78
	P8: Radiation response of different types of germanosilicate multimode optical fibers (*A. Travailleur, Polytechnique*)	p. 80
	P9: Radiation Responses of Ultra-Low-Loss/Low Loss Pure-Silica-Core Optical Fibers up to MGy Dose Levels (*G. Ciachera, Univ. Saint-Etienne*)	p. 82
	P10: Radiation-Induced Defects and Structural Modifications in SiO2: Insights from Electron Irradiation (*A. Alessi, Polytechnique*)	p. 84
	P11: The NanoSaintÉtienne platform for surface structuration and functionalization (*A. Meyer, Univ. Saint-Etienne*)	p. 86
	P12: X-ray Radiation Induced Luminescence of a Medium-OH Pure Silica Core Multimode Optical Fiber: Potential and Limitations for Dosimetry Applications (*L. Breccia, Univ. Pavia*)	p. 87
	P13: X-ray Radiation-induced Changes on Er3+ Ions Cross Sections (*A. Facchini, Univ. Saint-Etienne*)	p. 89
	P14: PETRA: an Experimental Platform for X-ray Radiation Testing of Materials and Components (*S. Girard, Univ. Saint-Etienne*)	p. 91
	P15: First On-Line Optical Glasses and crystals Measurements in a Nuclear Research Reactor for a Future Confocal Chromatic Sensor (*M. Agoyan, CEA-UJM*)	p. 93
	P16: CABRI Irradiation Facility (*M. Pouradier, CEA*)	

Thursday, June 26, 2025

8:30 – 9:10	**Invited Talk** - Challenges of using optical fibres for plasma current measurements during burning plasma operation of tokamaks - *Andrei Goussarov* (Introduction: Adriana Morana, Univ. Saint Etienne)	
Session 8: Radiation Effects on Fibers - **Andrei Goussarov, SCK-CEN**		
9:10 - 9:30	Study of optical fibers luminescence for nuclear reactors power measurement - *Marc Pouradier, CEA*	p. 96
9:30 – 9:50	Temperature Dependence on the Radiation Induced Attenuation of Fluorine-Doped Optical Fibers - *Adriana Morana, Univ. Saint-Etienne*	p. 98
9:50 – 10:10	Combined Temperature and Photobleaching Effects on P-doped Optical Fibers - *Allan Travailleur, Polytechnique*	p.100

10:10 – 11:00	**Coffee Break**	
11:00 – 11:40	**Invited Talk** - Cosolvent-free synthesis and characterization of poly(methylsilsesquioxane-codimethylsiloxane) liquids and deep-ultraviolet transparent elastic resins - *Koichi Kajhara, Tokyo Metropolitan University* (Introduction Linards Skuja, Univ. Latvia)	
Session 9: Polarization maintaining optical fibers - **Laurent Lablonde, Exail**		
11:40 – 12:00	From the micro- down to nanostructuration: an access to new polarisation-maintaining silica based optical fibres - *Monika Bouet, Univ. Lille*	p.103
12:00 – 12:20	Radiation Induced Attenuation of Space-grade Polarization-Maintaining Optical Fibers in the UV-Visible Domains - *Hugo Boiron, Exail*	p.105
12:20 – 12:30	**Closure of the SiO2 2025 Conference** **Youcef Ouerdane / Aziz Boukenter, Univ. Saint-Etienne**	
14:00 – 16:00	**Laboratory Hubert Curien Visit**	

Practical Informations

Cité du design

3, rue Javelin Pagnon, 42000 Saint-Etienne

On foot: fifteen minutes from the Place de l'Hôtel de Ville
By bike: self-service bikes
By Tram : Cité du design stop, Tram T1 and T2
By car:

- Parking Zénith (210 spaces, free)
- Rue Javelin Pagnon / Pablo Picasso (55 spaces including 1 disabled, paying)
- Rue Salvador Dali (75 spaces including 1 disabled, paying)
- Place Carnot (48 spaces including 4 disabled, paying)

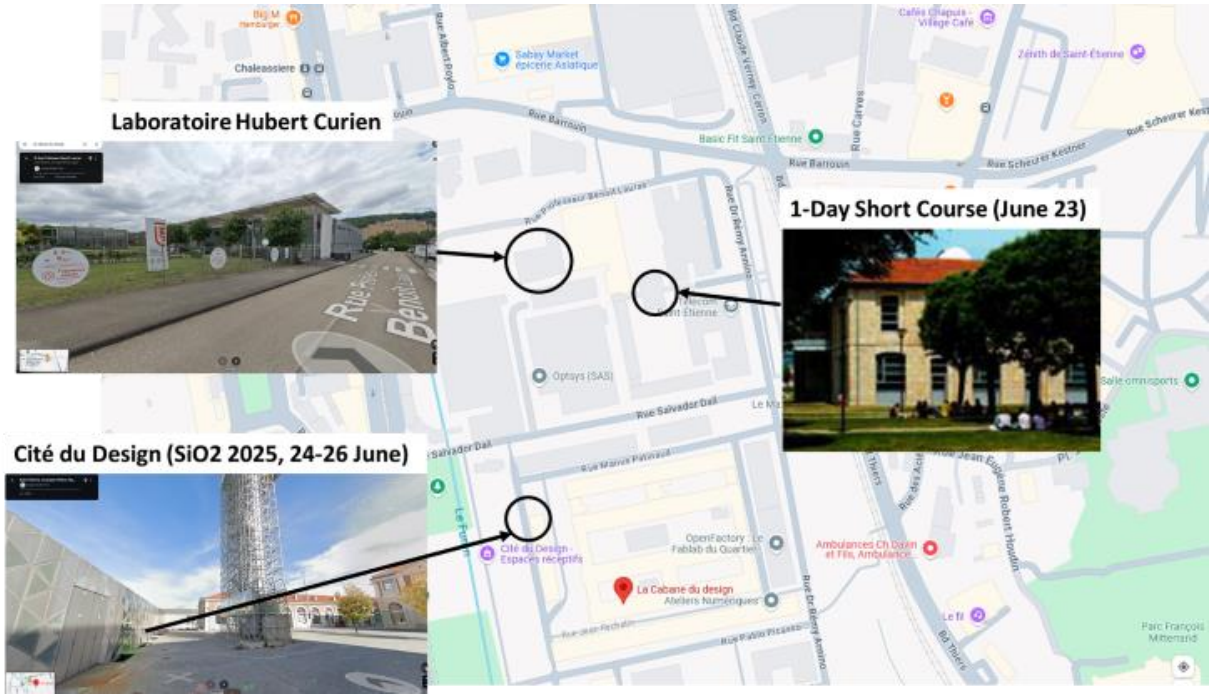

Laboratoire Hubert Curien, UMR CNRS 5516

Bâtiment F 18 Rue du Professeur Benoît Lauras (Campus Manufacture)
42000 Saint-Etienne
France

For the visit of Lab. Hubert Curien, an I.D. will be mandatory

Sponsors

https://www.exail.com/

https://www.andra.fr/

https://master-radmep.org/

https://manutech-sise.universite-lyon.fr/eur-manutech-sleight/

https://www.radecs-association.net/

Participant list

LASTNAME	FIRSTNAME	INSTITUTION
Acid	Selyan	CNES
Agnello	Simonpietro	Università di Palermo, Italy
Agoyan	Marion	Université Jean Monnet - Saint Etienne, France
Aguiar	Ygor	CERN
Alessi	Antonino	Polytechnique, France / Università di Palermo, Italy
Alem	Abrham Kassa	Université Jean Monnet - Saint Etienne, France
Asquini	Anna	STMicroelectronics, France
Aubry	Marine	TRAD, France
Avesani	Matilde	Université Jean Monnet - Saint Etienne, France
Babu	Arjun	Université Clermont Auvergne, France
Benabdesselam	Mourad	Université Côte d'Azur, France
Boiron	Hugo	Exail
Bouazaoui	Mohamed	Université de Lille, France
Bouet	Monika	Université de Lille, France
Boukenter	Aziz	Université Jean Monnet - Saint Etienne, France
Breccia	Letizia	Università di Pavia, Italy
Cannas	Marco	Università di Palermo, Italy
Capoen	Bruno	Université de Lille, France
Ciachera	Geoffrey	Université Jean Monnet - Saint Etienne, France
Correas	Vincent	STMicroelectronics, France
Coto	Mario	Université Jean Monnet - Saint Etienne, France
Couillaud	Hadrien	CEA, France
Darnon	Maxime	Université Jean Monnet - Saint Etienne, France
De Michele	Vincenzo	Université Jean Monnet - Saint Etienne, France
Di Francesca	Diego	CERN
El Aadad	Halima	Université de Lille, France
Facchini	Alberto	Université Jean Monnet - Saint Etienne, France
Ferrari	Matteo	Université Jean Monnet - Saint Etienne, France
Ficarra	Giuseppe	Università di Palermo, Italy
Fricano	Fiammetta	CEA
Gaillardin	Marc	CEA, France
Gasiot	Gilles	STMicroelectronics, France

LASTNAME	FIRSTNAME	INSTITUTION
Giacomazzi	Luigi	CNRS Trieste, Italy
Girard	Sylvain	Université Jean Monnet - Saint Etienne, France
Goussarov	Andrei	SCK-CEN, Belgium
Lambert	Damien	CEA
Kajihara	Koichi	Tokyo Metropolitan University, Japan
Kermouche	Guillaume	Ecole des Mines de Saint-Etienne, France
Madonia	Antonino	Università di Palermo, Italy
Marin	Emmanuel	Université Jean Monnet - Saint Etienne, France
Martin Samos	Layla	CNR-IOM, Italy
Mescia	Luciano	Politecnico di Bari, Italy
Messina	Fabrizio	Università di Palermo, Italy
Meyer	Arnaud	Université Jean Monnet - Saint Etienne, France
Morana	Adriana	Université Jean Monnet - Saint Etienne, France
Ollier	Nadège	Polytechnique, France
Olloghe Mandoukou	Rosa Darell	Université Jean Monnet - Saint Etienne, France
Ouerdane	Youcef	Université Jean Monnet - Saint Etienne, France
Paillet	Philippe	CEA
Pecorella	Roberto	Université Jean Monnet - Saint Etienne, France
Perrot	Jérémy	Université Jean Monnet - Saint Etienne, France
Petit	Yannick	Université de Bordeaux
Pouradier Duteil	Marc	CEA, France
Raj	Aditya	Université Jean Monnet - Saint Etienne, France
Richard	Nicolas	CEA, France
Roche	Martin	Université Jean Monnet - Saint Etienne, France
Royon	Maxime	Université Jean Monnet - Saint Etienne, France
Sadik	Charbel	Université de Lille, France
Shchedrina	Nadezhda	Université Paris-Saclay, France
Shumilov	Gevorg	Centre Hospitalier Princesse Gracen France
Skuja	Linards	University of Latvia, Latvia
Swart	Hendrik	University of the Free State, South Africa
Thery	Thomas	STMicroelectronics, France
Travailleur	Allan	Polytechnique, France
Velour	Arnaud	Université Jean Monnet - Saint Etienne, France
Weninger	Luca	Université Jean Monnet - Saint Etienne, France
Zuccala	Giorgio	STMicroelectronics, France

Tuesday, June 24th

Session #1

Ultrafast Spectroscopy

Youcef Ouerdane, Univ. Saint-Etienne

Time resolved mid-infrared absorption in silica: ultrafast heat transfer observed by direct probing of anharmonic vibrations

V. De Michele*, A. Tsaturyan*, J. Andrade**, M.-O. Winghart**, E. Kachan*, E. Nibbering**, C. D'amico*, J.-P. Colombier*, A. Mermillod-Blondin**, R. Stoian*

*Université Jean Monnet Saint-Etienne, Laboratoire Hubert Curien, F-42023, Saint-Etienne, France
** Max-Born Institute - Berlin (Germany)

ABSTRACT

The achievement of super-resolution at sub-100 nm scales in wide band-gap materials critically depends on the ability to rapidly quench energy, thereby enhancing energy confinement. In particular, precise control over the rate of thermal transfer and the influence of thermomechanical effects is essential for confining feature sizes well below the optical diffraction limit, making heat and its transport dynamics a central issue in laser-based material processing. In this context, our approach offers a direct investigation into ultrafast heat transport phenomena in laser-irradiated dielectric materials, aiming to reveal the interplay between electronically driven excitation and collisional activation of vibrational modes.

PACS Keywords: femtosecond pulses; laser microstructuring, nonlinear absorption; mid-infrared; Silica.

1 INTRODUCTION

Precise control over laser-induced material structuring demands a deep and comprehensive understanding of the fundamental mechanisms that govern light–matter interactions on ultrafast timescales [1]. This involves not only characterizing how materials absorb laser energy, but also elucidating the cascade of subsequent processes—spanning femtoseconds to picoseconds—that lead to energy redistribution and ultimately to permanent modifications in the material structure [2]. At the core of these processes are the ultrafast electronic excitations triggered by intense laser fields, which initiate a complex relaxation sequence involving both electronic transitions and vibrational responses. The interplay between these pathways determines the nature and extent of the induced modifications, whether transient or permanent, localized or extended. In this framework, attention has been focused on the use of mid-infrared (MIR) light, which allows to interact directly with infrared-active vibrational modes of the lattice, offering unique opportunities for selective and efficient energy deposition [3].

Here, we want to propose an innovative approach that leverages selective probing of vibrational modes in the MIR spectral region to investigate electron–phonon coupling dynamics under non-linear excitation conditions in bulk glassy materials. By driving the irradiated region far from equilibrium, with sub-picosecond time resolution, we aim to directly monitor fundamental mechanisms underlying light-matter interaction in strong fields, exploring the vibrational activation through the direct observation of the phonon dynamics.

2 EXPERIMENTAL SETUP

The proof of principle of our method were conducted on amorphous silica, as model material for transparent dielectrics. To explore the characteristic time for electron-lattice energy exchange, we investigated the Si-O-Si antisymmetric stretching overtone localized at approximately 4415 nm. This feature was chosen due to its relevance in the main structural changes of silica glass and its sensitivity to the distribution of the Si–O–Si bond angle [4], manifesting a clear dependence by the sample temperature (Figure 1) [5]. Furthermore, being an overtone, our measurements will be particularly sensitive to the anharmonicity of the atomic potential, allowing us to follow charge-induced potential distortions.

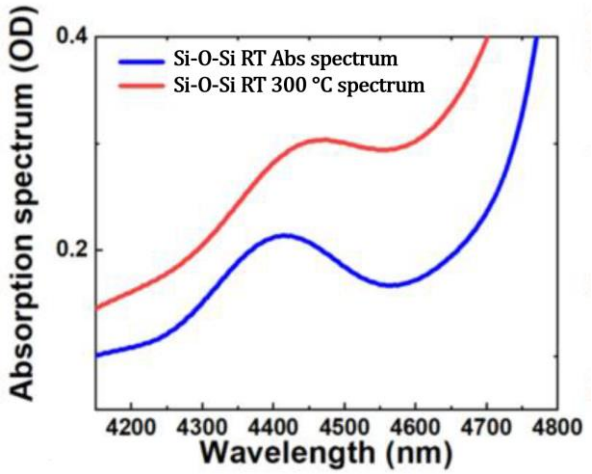

Figure 1. RT (Blue line) and 300 °C (Red line) Si-O-Si antisymmetric stretching overtone absorption band.

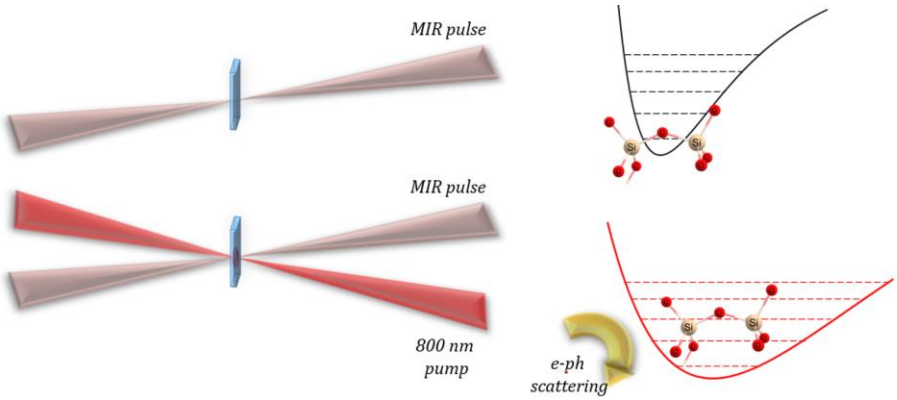

Figure 2

To monitor the laser-induced vibrational activation—in this case, the dynamics of the absorption band centered around 4415 nm—we used an ultrashort mid-infrared probe beam (pulse duration: 200 fs, centered at 4450 nm), following excitation by a 40 fs pump pulse (centered at 800 nm) at intensities near the optical breakdown threshold. By tracking the rapid temporal evolution of the transient absorption (TA) dynamics, information on the temperature rise can be obtained as a function of the pump–probe delay.

3 DISCUSSION

The novelty of our approach lies in the strategic investigation of vibrational activation. The identification of distinct vibrational markers on ultrafast timescales offers a powerful means to address a key question: how does the matrix respond to ultrafast electronic excitation? Our aim is to detect and directly interrogate vibrational signatures as local probes of structural dynamics. By employing a time-resolved technique, we seek to investigate the kinetics of energy transfer to the matrix, distinguishing between thermal and non-thermal vibrational activation processes.

By tracking the rapid temporal evolution of the transient absorption spectrum (i.e., the difference between the excited and ground-state absorption), with sub-picosecond time resolution, we can identify spectral broadening and/or shifts in characteristic vibrational modes. This enables real-time probing of electronically induced lattice distortions as well as collisional vibrational activation (Figure 2), thereby allowing us to determine both the relevant timescales and the speed of the processes—how quickly the matrix responds, thermally or electronically, to a sudden energy input.

Furthermore, by combining experimental observations with first-principles quantum molecular dynamics simulations of the photoelectronic process, we can disentangle electronic from molecular effects and distinguish between electronic and thermal mechanisms. Thanks to its innovative focus on vibrational coupling, this approach not only sheds light on electron-phonon coupling dynamics in strongly correlated materials but also provides a tool to probe crystalline polymorphs and phase transitions under volumetric excitation.

To demonstrate the feasibility of this method, we initially explored the characteristic timescales of electron-lattice energy exchange in amorphous silica. The technique, however, is designed to be extended to other strongly coupled materials, particularly crystalline ones such as quartz and sapphire, for studying polymorphism and volume-induced phase transitions.

In amorphous silica, one particularly promising vibrational marker is the Si–O–Si antisymmetric stretching overtone at ~4415 nm, which is sensitive to both temperature changes and local potential variations. Our preliminary findings reveal a surprisingly rapid evolution of this vibrational band on sub-picosecond timescales, indicating a faster-than-expected vibrational activation (within a few picoseconds) [6]. This ultrafast response suggests a vibrational activation mechanism different from conventional electron-phonon scattering, supporting the hypothesis of a nonthermal, laser-induced rearrangement of the polarized matrix.

This methodology can be readily extended to other local vibrational markers within glassy matrices, highlighting the potential of our approach as a powerful tool for analyzing electron-phonon interactions in disordered materials.

REFERENCES

[1] R. Stoian and J.-P. Colombier, Nanophotonics 9, 4665-4688 (2020).
[2] R. Stoian, Adv. Opt. Technol. 12:1237524 (2023).
[3] M. Rini et al, Nature 449, 72-74 (2007).
[4] H. Kakiuchida et al., J. Appl. Phys. 93, 777-779 (2003).
[5] G. Navarra et al, J. Non-Cryst. 355, 1028-1033 (2009).
[6] M. V. Fischetti, Phys. Rev. Lett. 53, 1755-1758 (1984).

Tuesday, June 24th

Session #2

Grating Functionalization of materials

Emmanuel Marin*, Univ. Saint-Etienne*

Densification evaluation in femtosecond laser modified silica glass of types I, II and III

Shchedrina N.[1,2], Ollier N.[2], Sosa M.[1,3], Lancry M.[1]
1- Institut de Chimie Moléculaire et des Matériaux d'Orsay, Université Paris-Saclay, France
2- Laboratoire des Solides Irradiés, École polytechnique-CEA-CNRS, France
3- Université Paris-Saclay, CEA, List, 91120 Palaiseau, France

* nadezhda.shchedrina@universite-paris-saclay.fr

ABSTRACT

Ultrafast laser interactions can induce a wide variety of localized modifications within the volume of glass materials, such as Type I, II and III. In this work, we investigate the levels of densification associated with these modification types at the nanoscale, as well as their underlying mechanisms. Advanced characterization techniques, including scattering scanning near-field optical microscopy (s-SNOM) and nano-Fourier transform infrared (nano-FTIR) spectroscopy, are employed to resolve spectral shifts and structural rearrangements within the laser-modified volumes at the nanoscale.

PACS Keywords: fs-lasers, densification, silica glass

1 INTRODUCTION

Focusing ultrashort laser pulses can induce localized modifications within the volume of glass that are typically categorized into different types (e.g., Types I, II, III, A, X, etc.) [1]. Type I is characterized by an isotropic index change mostly due to volume changes and point defects, Type II exhibits anisotropic index changes due to nanograting formation, and Type III involves the formation of nano- and micro-voids surrounded by a densified shell. The properties and applications of these laser-induced modifications depend critically on both the laser parameters (such as energy, pulse duration, repetition rate, wavelength, etc.) and the material properties, such as band gap, viscosity, density, fictive temperature, heat capacity, and thermal conductivity.

These modifications induce significant changes in the glass's optical, mechanical, and thermal properties by altering its structure. In this study, we focus on the nanoscale densification processes in silica glass associated with the main transformation types (Types I, II, and III) using advanced techniques such as scattering scanning near-field optical microscopy (s-SNOM) and nano-Fourier transform infrared (nano-FTIR) spectroscopy performed at Synchrotron Soleil.

Although previous studies have confirmed densification in all three types of femtosecond laser-induced volume modifications in silica using Raman microspectroscopy [2], mechanical property measurements [2,3], and refractive index assessments [4], the densification levels and the underlying mechanisms remain uncertain. Also, these estimations lack the nanoscale resolution. To address this, we employ nano-FTIR and IR s-SNOM techniques to probe the asymmetrical stretching vibrations of the Si–O–Si bonds, which are directly linked to density changes [5]. This approach enables us to translate observed shifts in the IR band positions into precise density estimations and to gain insight into the mechanisms, such as thermal quenching, defect formation, and high-pressure effects, etc., that drive the densification processes in each modification regime.

2 METHODOLOGY

We investigated three silica samples, each corresponding to one of the fs-laser induced modification types: Type I, Type II, and Type III. These modifications were inscribed using specific laser parameters to induce the desired structural changes. Type I modifications were generated in Suprasil CG silica glass using 800 nm, 160 fs pulses at 0.23 µJ/pulse with a 100 kHz repetition rate, a writing speed of 100 µm/s, and a numerical aperture (NA) of 0.6. Type II modifications were formed in Suprasil CG silica at 1030 nm, 250 fs, 1 µJ/pulse, 100 kHz, 10 µm/s, NA = 0.6. Type III modifications were created in GeO_2-doped SMF-28e single-mode optical fibers (Corning) using 515 nm, 170 fs pulses at 30 nJ/pulse, a single-shot exposure, and NA = 1.4. After laser inscription, all samples were cleaved to expose the XY cross-sectional plane of the modified regions for analysis.

Subsequently, s-SNOM measurements were performed at Synchrotron Soleil (SMIS beamline) to obtain amplitude and phase maps at selected wavenumbers (Figure 1). We focused on 1120 cm^{-1} and 1130 cm^{-1}, corresponding to the Si–O–Si asymmetric stretching absorption band in silica glass, which is highly sensitive to permanent strain. When densification occurs, this band undergoes a redshift, leading to a decrease in amplitude (as the measurements move on the right shoulder of the spectrum) and variations in the phase spectra (either increases or decreases), depending on the

chosen wavenumber and its position relative to the shifted band. Then, we measured nanoscale infrared spectra (nano-FTIR) using s-SNOM to directly probe local vibrational changes at nanoscale (Figure 2).

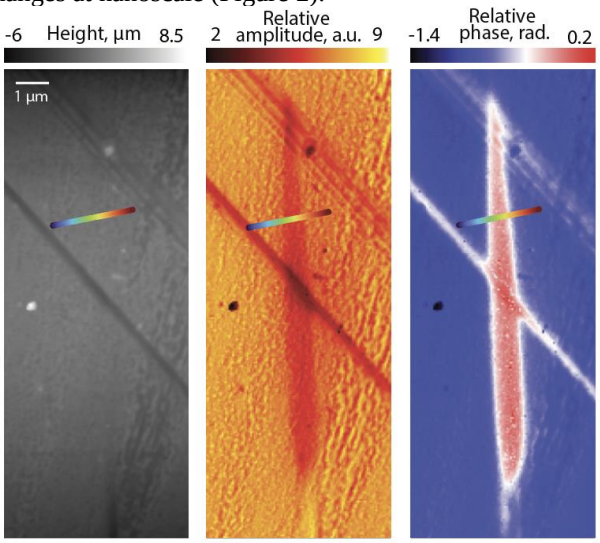

Figure 1: S-SNOM images of the sample with Type I fs-laser modification. The AFM surface topography is presented alongside the near-field amplitude and phase maps at 1130 cm^{-1}; Lines on the maps indicate the linescan measurements presented in Figure 2.

3 RESULTS AND DISCUSSION

We measured nano-FTIR amplitude and phase spectra both inside and outside the laser-modified regions, converting the observed IR band shifts into density estimations using a well-established linear relationship between the Si–O–Si asymmetric stretching band position and silica density [5]. In all investigated samples, the redshift of this band confirms significant densification across Type I, Type II, and Type III modifications. For Type I, a shift of about 7 cm^{-1} (Figure 2) corresponds to ~3–4% densification. For the densification mechanism, defect-driven structural modification (e.g., involving E′ centers and NBOHC) combined with thermal quenching likely contributes to the final densified state.

Type II modifications exhibit more complex, periodic shifts that mirror the alternating densified and porous layers of nanogratings, with overall densification reaching 8–13% [6]. These higher values suggest a combined effect of elevated temperatures and presence of pressures, up to approximately 10-15 GPa as estimated from shock-wave models and the high-pressure Hugoniot relationship, which drive the densification in Type II.

For Type III modifications, which involve micro- or nano-void formation, the surrounding shell exhibits a densification of roughly 6%. Although initial shock-induced pressures may transiently exceed tens of gigapascals before being moderated by plasma shielding, the subsequent temperature rise (due to the strain relaxation wave) leads to partial structural relaxation and a lower densification. This outcome aligns with both hydrostatic and shock-wave pressure studies, where immediate post-shock densities are higher but relax due to increased temperature.

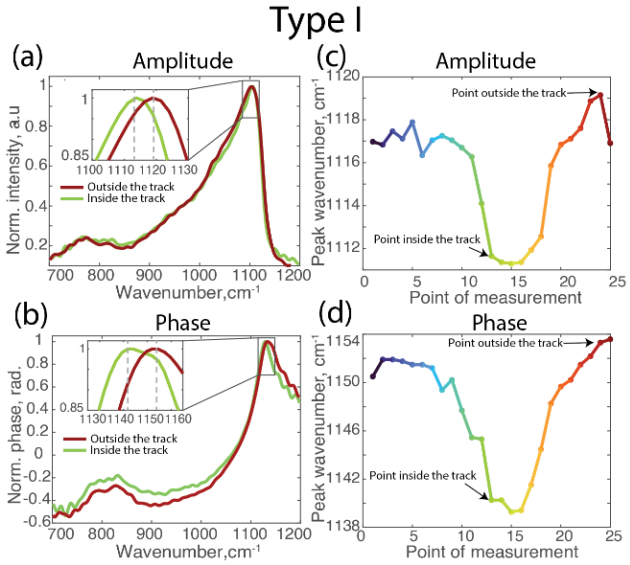

Figure 2: Nano-IR measurements for Type I: a) synchrotron nano-FTIR amplitude and (b) phase spectra for pristine material and irradiated area inside of the laser track; (c) amplitude peak position and (d) phase peak position along the line profile.

Acknowledgments: We acknowledge the support of the SMIS beamline from synchrotron SOLEIL.

REFERENCES

1. Stoian, R. Volume Photoinscription of Glasses: Three-Dimensional Micro- and Nanostructuring with Ultrashort Laser Pulses. *Appl. Phys. A Mater. Sci. Process.* **2020**, *126*
2. Champion, A.; Bellouard, Y. Direct Volume Variation Measurements in Fused Silica Specimens Exposed to Femtosecond Laser. *Opt. Mater. Express* **2012**, *2*, 789.
3. Vlugter, P.; Bellouard, Y. Elastic Properties of Self-Organized Nanogratings Produced by Femtosecond Laser Exposure of Fused Silica. *Phys. Rev. Mater.* **2020**, *4*
4. Bricchi, E.; Klappauf, B.G.; Kazansky, P.G. Form Birefringence and Negative Index Change Created by Femtosecond Direct Writing in Transparent Materials. *Opt. Lett.* **2004**, *29*, 119–121.
5. Tan, C.Z.; Arndt, J.; Xie, H.S. Optical Properties of Densified Silica Glasses. *Physica B Condens. Matter* **1998**, *252*, 28–33.
6. Shchedrina, N.; Nemeth, G.; Borondics, F.; Ollier, N.; Lancry, M. Nano-FTIR Spectroscopy Reveals SiO2 Densification within Fs-Laser Induced Nanogratings. *Nanoscale Adv.* **2024**, *6*, 5164–5170.

Enhancing Stability and Radiation Resilience of Narrowband Optical Filters for High Power and Space Applications

Lablonde L. *, Pinsard E.*, Le Grand C. *, Le Masson R. *, Boiron H. *, Robin T.*, Marin E.**, Morana A.**
*Exail, rue Paul Sabatier, 22300 Lannion
** Laboratoire Hubert Curien, Université Jean Monnet
18 Rue Professeur Benoît Lauras, 42000 Saint-Étienne

ABSTRACT

Phase-shifted ultra-narrowband fiber Bragg gratings (PS-FBGs) exhibit significant sensitivity to optical power, which can impair their performance in demanding environments. In this study, we present the design and material optimization of PS-FBG-based filters capable of maintaining spectral stability up to 100 mW of injected optical power. We further investigate their radiation resilience by subjecting them to X-ray exposure up to 8.5 kGy(SiO_2), simulating space-like conditions.

Keywords: narrowband filter, phase-shifted FBG, RIA, fiber optic sensor

1 INTRODUCTION

Fiber Bragg gratings (FBGs) are widely deployed in fields such as healthcare, aerospace and defense, leveraging their optical properties for sensing and spectral filtering applications. Phase-shifted fiber Bragg gratings (PS-FBGs), in particular, provide highly selective bandwidths [1], enabling their use in laser line filtering, RF-over-fiber-links, and quantum systems[2]. However, their deployment in high-power or space environment requires addressing key limitations, especially their sensitivity to photo-thermal effects and radiation-induced changes. This study focuses on optimizing the intrinsic stability of PS-FBGs under extreme conditions, by analyzing factors such as fiber pre-treatment, inscription conditions, and index modulation profile. Our objective is to develop PS-FBGs that remain stable at optical powers up to 100 mW. X-ray exposure tests were conducted to evaluate radiation resistance, and packaging solutions were proposed to improve power stability and add functionality.

2 FILTER DESIGN AND CHARACTERIZATION

Filters with 1 GHz bandwidth filters were inscribed on Exail PM fiber (IXF-PMF-1550-125-P-012) whereas 4–5 GHz filters were fabricated on Corning SMF28e+ fiber (Fig.1). These filters, centered around 1.55 µm, were carried out using a phase mask dithering technique and a pulsed UV laser beam. The PM filter, with a Lorentzian shape, was created by incorporating a π phase shift at the center of a 7 mm grating with a coupling coefficient of $\kappa = 7\ cm^{-1}$. The flat-top passband and enhanced out-of-band rejection of the 4–5 GHz filter were achieved by introducing two π phase shifts at 1.25 mm and 3.75 mm along a 5 mm grating with $\kappa = 12.6\ cm^{-1}$. Phase shifts must be precisely adjusted, if needed via local CO_2 laser post-treatment, to ensure a ripple-free passband. All filters exhibit transmission rejection greater than 20 dB outside the passband and a −3 dB stopband wider than 60 GHz. Filters were thermally passivated for 8 hours at 120°C prior to characterization.

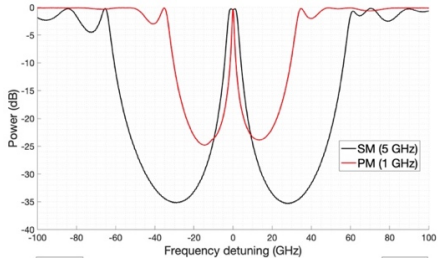

Fig. 1: Transmission spectrum measurement of the filters

Photo-inscription induces absorption at the signal wavelength, which increases proportionally to the grating's coupling coefficient and whose slope depends on the inscription conditions, fiber type, and pre-treatment. This absorption converts to heat, particularly near the phase-shift regions where optical energy accumulates. The theoretical intensity distribution I(z) at the Bragg wavelength λ_B for a uniform π phase-shifted grating of length L is given by:

$$I(z) \propto \cosh^2[\kappa(z-L/2)] \qquad (1)$$

with $\kappa = \pi \cdot \Delta n \cdot \Gamma / \lambda_B$, where Δn is the refractive index modulation, and Γ is the optical mode overlap factor. Due to the intensity peak and the grating's thermal sensitivity, the passband wavelength shifts more than the stopband.

3 RESULTS AND DISCUSSION

PS-FBG fabrication revealed several factors influencing power sensitivity. We compared sensitivity slopes obtained from various fabrication combinations, involving three pre-treatment conditions, two index modulation profiles in the grating, and three photo-inscription conditions. The latter mainly varied the writing laser wavelength for type I-UV

FBGs (called 1,2 and 3). Profile variations involved introducing or omitting an index modulation "blank" at the phase shift to reduce local optical intensity. Fiber pre-treatment included hydrogen (B), deuterium (C) or no (A) loading before inscription. In total, twenty-one fabrication combinations were tested. We developed a characterization setup to study the photo-thermal effect using a quasi-static scanning method relied on a tunable laser source, a wavelength meter and an InGaAs photodiode. Fig. 2 shows an example of the recorded spectra, around a filter bandpass, for different powers injected into the PS-FBG, which was suspended in still air to capture the component's intrinsic sensitivity. The right triangle shape of the response corresponds to the laser signal's "push effect" on the bandpass, which becomes more pronounced as the tunable laser wavelength approaches, from the short wavelength side [3], the filter bandpass, due to the intensity enhancement.

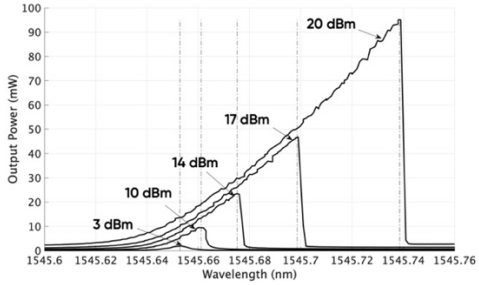

Fig. 2: Bandpass drift vs. input power (3-20 dBm) for standard PS-FBG.

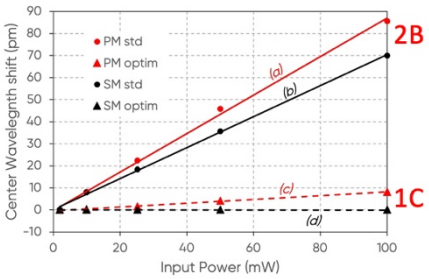

Fig. 3: Power sensitivity of most (1C) vs. least (2B) stable PM and SM filters.

Combinations involving standard FBG fabrication method (pre-treatment B) resulted in the highest sensitivities for both SM and PM fibers, with average slopes of 0.33–0.73 pm/mW and 0.95–1.21 pm/mW, respectively. The optimal combination (1C) yielded the lowest power sensitivity: below 0.05 pm/mW for SM filters and between 0.06 and 0.09 pm/mW for PM filters (Fig. 3). Two packaging solutions were developed to further reduce power sensitivity while enabling wavelength tunability and thermal compensation, ensuring stable continuous-wave operation up to 100 mW. The impact of radiation on PS-FBG optical response was also investigated. X-ray exposure can reduce reflectivity, shift the passband wavelength, or cause passband distortion. These effects depend not only on the fiber and fabrication conditions but also on irradiation parameters [4]. Such variations can degrade system performance and are difficult to predict without experimental data. We exposed three PS-FBGs to X-rays at a total dose of 8.5 kGy(SiO_2), with a dose rate of 40 mGy/s(SiO_2) at room temperature. During exposure, we observed a quasi-linear redshift of the central wavelength (Fig. 4), with a slope of ~2 pm/kGy for the most power-stable filters, lower than that of conventional filters. No passband distortion was observed for any of the three components.

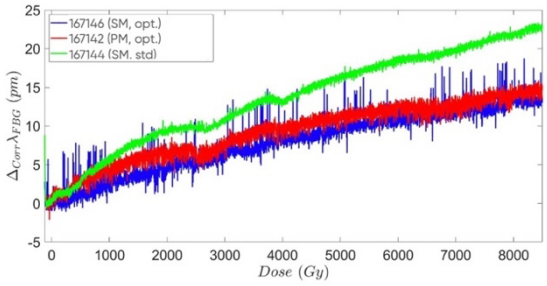

Fig. 4: Central wavelength shift during X-ray exposure.

4 CONCLUSION & PERSPECTIVES

This work demonstrates that PS-FBGs can be engineered for high-power and space applications through careful control of material parameters, including fiber composition, pre-treatment, and index modulation. The resulting narrowband filters show improved photothermal stability and reduced radiation sensitivity, with stable operation up to 100 mW and tolerance to multi-kGy radiation doses. These findings support their integration into next-generation photonic systems in harsh environments.

The present work was supported under a R&T project from CNES (contract n°R-S22/TC-0007-117).

5 REFERENCES

[1] G. P. Agrawal, et al., "Phase-shifted fiber Bragg gratings and their application for wavelength demultiplexing", *IEEE Photonics Tech. Lett.*, vol.6, no.8, 995–997 (1994).

[2] Y. Qin, et al., "Dual-channel and reconfigurable microwave photonic filter based on Dpol-DMZM and PS-FBG", *2021 Photon. & Electrom. Research Symposium*, 1559 (2021).

[3] J. H. Chow, et al., "Photothermal effects in passive fiber Bragg grating resonators", *Opt. Lett.*, vol.30, no.7, 708–710 (2005)

[4] A. Morana, et al., "Radiation-response of distributed feedback Bragg gratings for space applications", *IEEE Trans. Nucl. Sci.*, vol.67, no.1, 284–288 (2020);

Optical sensor based on a diffraction grating combined with a hydrogenated amorphous silicon layer

R. Olloghe Mandoukou[*], I. Verrier[*], M. Royon[*], M. Darnon[*], D. Jamon[*], A. Meyer [*], L. Dubost[**], W. Ravisy [**], G. El Haber [**], Y. Jourlin[*]

[*]Laboratoire Hubert Curien UMR 5516
42023 Saint-Etienne, France
[**]HEF IREIS
42160 Andrézieux-Bouthéon, France

ABSTRACT

The use of optical sensors has grown considerably, both in air quality control applications and in the detection of biological species. The design of optical sensors based mainly on diffraction gratings generally requires probing the structured metal surface from above. This approach, subject to the use of plasmon surface resonance (SPR), can prove limiting, as the reflected signal can be disrupted by absorption or scattering of the signal as it passes through the various gases or solutions to be analyzed. This is why, to counter this problem, a dielectric approach has been envisaged, proposing to probe from above. To achieve this, a very high-index layer that is transparent at the wavelengths of use is required, hence the choice of hydrogenated amorphous silicon. The grating combined with this thin film generates resonances and energy transfers between the diffracted 0 and -1 orders used for our detection [1-4].

PACS Keywords: Resonant diffraction grating, dielectric waveguides, hydrogenated amorphous silicon, energy transfer, optical sensor

1 INTRODUCTION

The role of optical sensors based on diffraction gratings is becoming increasingly important in the scientific-community, thanks to their wide range of environmental and biological applications. These applications are usually based on the exploitation of plasmonic effects using metallic diffraction gratings under TM polarization. Among them, the so-called “energy transfer” phenomenon between the two 0th and -1st orders was highlighted in previous studies [1, 3-4] where the plasmon modes are excited by the incident wave (Figure 1). This method has been used to detect changes in the refractive index of the medium to be tested and forms the basis of the sensor.

a)

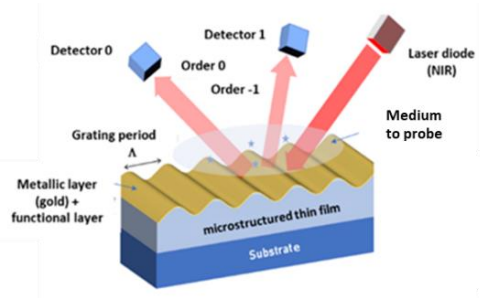

b)

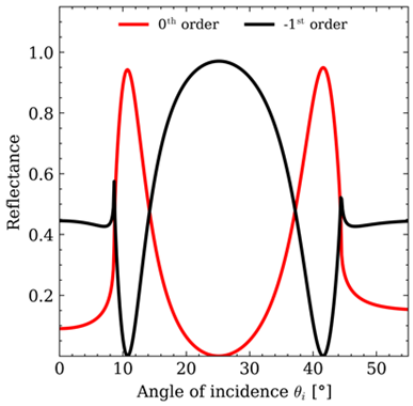

Figure 1: (a) Diagram of the transducer operating from the top. (b) Energy transfer between the 0th and the 1st reflected orders via excitation of a plasmon by a metallic diffraction grating [3].

However, the signal passing through the medium to be analyzed (gas or biological solution) may be subject to disturbances such as scattering or absorption, thus limiting sensor performance. Hence the dielectric approach, which proposes probing from below to overcome this constraint, is here considered. To achieve this, it is important to meet a number of requirements, such as the use of a very high index

layer that is also transparent in the near infra-red wavelengths range. Hydrogenated amorphous silicon (a-Si:H) proved to be a suitable material. This new configuration is illustrated in Figure 2.

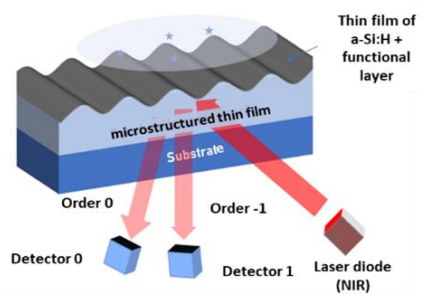

Figure 2: Principle of a transducer exploiting waveguide modes in optical switch configuration using a-Si:H grating illuminated from the bottom.

This second configuration (Figure 2) compared to the Figure 1 has the advantage of operating from the bottom of the transducer, using the very high refractive index material with very low absorption, and of obtaining waveguide resonances that are still largely unexploited.

2 SENSOR OPERATION USING THE ENERGY TRANSFER

This section attempts to explain in more detail the use of the energy efficiencies as a sensor. In order to understand how behaves this sensor, we refer to the plasmonic model illustrated in figure 3.

Figure 3(a) shows the typical curve of an energy transfer when the surrounding medium is air (n=1). We can observe an energy transfer between the 0th and -1st orders depending on the angle of incidence. One interesting point is that for two particular angles (Θl and Θr,) the diffraction efficiencies are similar (around 50 %). However, by changing the medium to be probed, for instance water (n = 1.33) as illustrated in figure 3(b), the energy transfer between the 2 diffracted orders slightly changes: at Θl and Θr, the diffraction efficiencies are no longer equal. Thus, the signal difference (Δ) provides information about the index variation and the species to be characterized.

a)

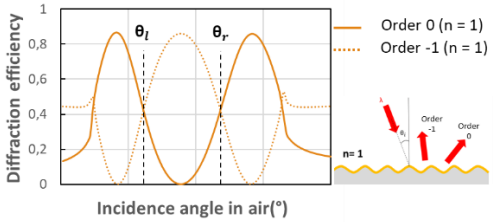

b)

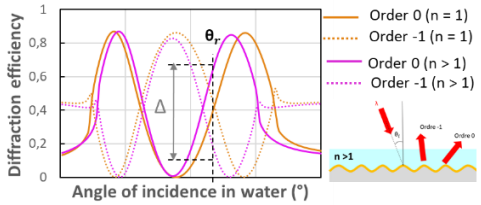

Figure 3: (a) Energy transfer between the 0th and the 1st reflected order in the air (b) Energy transfer between the 0th and the 1st reflected order in the water [4].

In the bottom-up approach envisaged in our study, the same procedure was followed: first, angular measurements in air were compared to simulation using data provided by sample characterization (Figure 4). This was followed by refractive index variation measurements to validate the proof-of-concept as it will be presented afterwards.

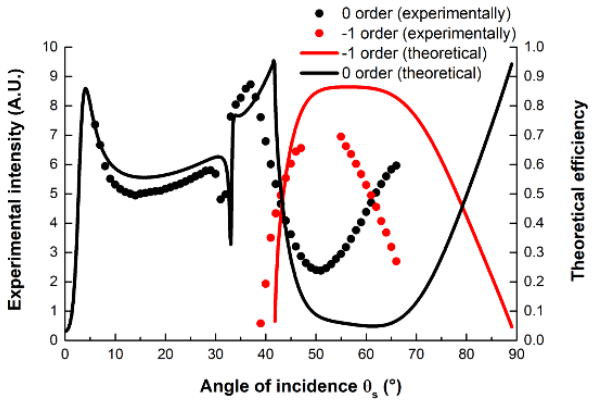

Figure 4: Energy transfer between the 0th and the 1st reflected order by the a-Si:H grating in the air (theoretically and experimentally).

REFERENCES

[1] J. Sauvage-Vincent, Y. Jourlin, V. Petiton *et al.*, "Low-loss plasmon-triggered switching between reflected free-space diffraction orders," Opt. Express, 22(11), 13314 (2014).

[2] O. Parriaux, and Y. Jourlin, "Lossless 0th and −1st order switching by dual-excitation of grating waveguide mode," J. Opt., 21(7), 075603 (2019).

[3] H. Bruhier, I. Verrier, J. Brunet, *et al.*, "Theoretical investigation of refractive index detection limit in the Surface Plasmon Resonance-triggered switch effect," IEEE Sensors Journal, **24**(24), 40659 (2024).

[4] E. Laffont, N. Crespo-Monteiro, P. Berini, *et al.*, "Development of a new plasmonic transducer for the detection of biological species," Optical Sensing and Detection VII, (2022).

Tuesday, June 24th

Session #3

Radiation induced point defects

Nadège Ollier, LSI

EPR and optical studies of silica glass implanted by $^{12}C^+$ and $^{13}C^+$ ions.

Madara Leimane*, Anders Hallén**, Linards Skuja*
*Institute of Solid State Physics, University of Latvia, Riga, Latvia
**KTH —Royal Institute of Technology, Kista, Sweden

ABSTRACT

Carbon impurities in SiO_2 are important for various technologies. They are caused by synthesis of silica glass from silicon-organic materials or by oxidation of SiC wafers in semiconductor device processing. This paper reports carbon-related defects introduced in silica by implantation of $^{12}C^+$ (I=0) or $^{13}C^+$ (I=1/2) ions with 50 keV or 300 keV energies. Optical and infrared absorption, luminescence, and EPR spectra were studied. A comparison between $^{12}C^+$ and $^{13}C^+$ ion-implanted samples allows to separate E'-centers and ^{12}C – related signal with g = [2.0006, 2.0032, 2.0035]. $^{13}C^+$-implanted samples show two new doublets separated by 9.5 mT and by 21.7 mT. They are tentatively attributed to 3-fold silicon-bonded carbon radical ($Si_3{\equiv}C^{\bullet}$) and Si-bonded CO_2 radical ($O_3{\equiv}Si^+\text{-}CO_2^{\bullet}$).

PACS Keywords: silica glass, carbon doping, ion-implantation, EPR, hyperfine coupling

1 INTRODUCTION

The properties of carbon impurities in silica glasses and amorphous SiO_2 oxide layers are of interest because of an increased reliance on carbon-containing silicon-organic raw materials for industrial synthesis of SiO_2 glasses, the presence of carbon in various SiO_2 nanostructures, sol-gel synthesized glasses and ink-jet printing inks. In power electronics, carbon impurities adversely affect the quality of SiO_2 oxide layers in SiC-based electronics. There are numerous studies of compounds with large C concentrations, e.g., Si oxycarbide glasses, C nanoparticles in silica, "organosilicas". However, the initial incorporation of separate C atoms in silica glass matrix is still not well-understood. In this work, carbon ^{12}C and its magnetic isotope ^{13}C are introduced in silica by ion implantation and studied by optical and EPR spectroscopy. Optical and, in particular, EPR evidence points to at least 5 distinct carbon-related structures in C-implanted silica.

2 EXPERIMENTAL

High purity synthetic silica samples manufactured by Ohara, Heraeus, Asahi Glass, Tosoh Quartz with hydroxyl group (Si-O-H) concentration in the range between $2{\times}10^{18}$ cm^{-3} and $1{\times}10^{20}$ cm^{-3}, 2 sides optically polished, thickness between 0.5 and 1 mm were used. They were implanted by $^{12}C^+$, $^{13}C^+$ and Ne^+ ions with energies 50, 75 and 300 keV and fluences between 1 $\times10^{15}$ and $3{\times}10^{16}$ ions/cm^2 at room temperature. Two different implantation energies, 50 keV and 300 keV were selected for carbon ions in order to assess the possible effects of different C ion distribution densities, and to distinguish between the chemical effects of carbon doping and radiation damage. The depth of radiation damage was estimated by SRIM-2013 program as ~200 nm and 900 nm from the surface, respectively. Several control samples were implanted by 75 keV Ne^+ ions to distinguish between carbon-doping and radiation damage effects.

The samples were studied by VIS-UV and vacuum UV optical absorption (OA), photoluminescence (PL) emission and excitation (PLE), X-band electron paramagnetic resonance (EPR), and Fourier transform infrared (FTIR) absorption methods. All measurements were done at the room temperature.

3 RESULTS AND DISCUSSION

Optical absorption (OA) spectra of implanted samples show peaks at 5.03 eV, 5.71 eV, and 7.6 eV, characteristic to divalent Si ("SiODC(II)"), E'-centers, and oxygen vacancies ("SiODC(I)"), respectively. Several weak peaks between 2 and 5 eV can be traced to the interference fringes due to the reflection from the inner boundary of the damaged layer having an increased refraction coefficient. Considering the small thickness of the irradiation damage layers, the OA peaks are very intense, e.g., 737 cm^{-1} and 504 cm^{-1} for SiODC(II) in samples implanted by 10^{16} cm^{-2} 50 keV and 300 keV C ions, respectively. This corresponds to ~10^{19} centers/cm^3, it exceeds >100 times the concentration of SiODC(II) in the most O-deficient commercial silica glasses. The concentration of oxygen vacancies SiODC(I), estimated from the 7.6 eV OA band, exceeds 10^{20} cm^{-3}. The ODC concentration is ~ 4 times less upon equivalent irradiation by Ne ions, indicating the role of carbon in creating O deficiency. The presence of non-bridging oxygen hole centers (NBOHC) is indicated by PL spectra, however, the corresponding UV OA bands are evidently too weak to be resolved. Distinct OA bands, specifically related to C atoms are not found. Instead, a broad and intense background, monotonously raising towards the absorption edge near 8 eV is present. Its intensity grows with increasing C-implantation

dose and reaches high values of 5×10^4 cm^{-1} @7.8 eV for 3×10^{16} C$^+$/cm^2 implanted sample. It can be assigned to formation of C clusters.

Photoluminescence (PL) spectra of both Ne- and C-implanted samples show bands of intrinsic defects NBOHC (1.9 eV) and SiODC(II) (2.6 eV and 4.4 eV) upon excitation at 5 eV. C-implanted samples show an additional band at 2.14 eV. It has a broad excitation band in entire VIS-UV spectral range with the first (weak) peak at 2.4 eV, and strongest peaks at 5.0 and 5.8 eV. The carbon-related PL spectrum is evidently heterogeneous, emitted by PL centers with continuously distributed properties. When excitation energy is varied in the 2.2 eV – 3.2 eV range, the peaks of PL emission spectra shift accordingly with a Stoke's shift of ~0.3-0.5 eV. This property is consistent with a formation of different-sized clusters. Formation of luminescent C clusters in SiO_2:C systems is suggested in many studies, e.g. [1], an overview can be found in ref. [2].

Infrared absorption spectra of carbon-implanted samples show weak bands with peaks at 2136 cm^{-1} and 2339 cm^{-1}, which correspond to the stretching vibration of CO and antisymmetric stretching of CO_2 molecules, respectively. These bands are absent in Ne-implanted samples. The intensity of the bands grows without saturation up to the highest ion dose 3×10^{16} cm^{-2}. The concentration of CO_2 molecules then reach 5×10^{19} cm^{-3} in the irradiated layer, indicating that a significant fraction of oxygen atoms, displaced by formation of $>10^{20}$ cm^{-3} SiODC(I), are scavenged by C ions. The areal density of CO_2 molecules is 1×10^{15} cm^{-2}, indicating that ~3% of 3×10^{16} cm^{-2} ions, implanted in this sample, form CO_2 molecules.

Electron paramagnetic resonance (EPR) spectra of all implanted samples show signal of E'$_\gamma$ -centers (g=2.0007). Compared to E'-centers in neutron-irradiated silica, they are broadened and have much faster relaxation times: saturation starts at 500 times higher microwave power (~500 μW). Their volume concentration exceeds ~10^{18} spins/cm^3 in Ne-implanted samples.

^{12}C-implanted samples show an additional EPR signal at g~2.003, which grows with increasing the ion dose and becomes dominant at 3×10^{16} ions/cm^2. By subtracting the remnants of E'-center signal and fitting using EasySpin MatLab toolbox [3] the principal g values are found as [2.0006, 2.0032, 2.0035]. Signals in this g-factor region are typical for many SiO_2: C systems [4,5]. Apart from a weak 7.4 mT doublet from H(I) centers, the signals were similar in high-OH and low-OH samples.

In samples implanted by magnetic (I=1/2) ^{13}C isotope, the EPR signal drastically changes. The central part of the carbon-related signal at g~2.003 disappears, leaving only a broadened E'-center signal. Instead, two weak doublets with splitting of 21.7 mT and ~9.5 mT appear. They belong to two distinct centers featuring hyperfine coupling to a single ^{13}C nucleus. Such hf doublets in SiO_2-carbon compounds have not been previously reported. However, in EPR studies of SiO_2 surfaces, a growth of 21.8 mT doublet upon reversible adsorption of $^{13}CO_2$ molecules on surface E'-centers (silicon dangling bonds) was observed [6]. Its g-values [1.9980, 2.0016, 2.0027] are close to values [1.9999, 2.0001, 2.0034], obtained by EasySpin simulation from our data for 21.7 mT doublet. Hence, it can be assigned to formation of glass network bound $Si^+CO_2^-$ radicals in the implanted region.

There is some uncertainty in the accurate shape of the 9.5 mT doublet because of overlap with other signals. It has an asymmetric shape, characteristic to the case of nearly equal isotropic and anisotropic hyperfine constants. It can be approximately simulated by g=1.9980 and hyperfine parameters a=3.70 mT, b=3.10 mT. Out of the reported data on SiO_2:C, the closest is the EPR signal of a dangling bond on a surface carbon, bound to 3 silicons in SiO_2 network, a $(\equiv Si_3)$-C$^\bullet$ radical [5].

The intensities of both doublet signals are significantly smaller than the intensity of the "central" (g~ 2.003) signal in ^{12}C-implanted samples, which disappears in ^{13}C-implanted samples. Most probably, a large part of the paramagnetic centers become broadened beyond detection due to hyperfine coupling to multiple ^{13}C nuclei in carbon clusters containing paramagnetic dangling bond. Along with the OA and PL data, this is in accord with the general notion that, at least at the employed relative large ion fluences, the majority of implanted carbon ions forms clusters.

Acknowledgements. Support from France-Latvia bilateral mobility grant LV-FR/2025/3 OSMOZE, Latvian Science Council project lzp-2024/1-0676 and Ion Technology Centre at Uppsala University is acknowledged.

REFERENCES

[1] A. Vasin, D. Kysil, O. Isaieva, G. Rudko, D. Virnyi, S. Sevostianov, V. Tertykh, Y.P. Piryatinski, S. Starik, L. Vaccaro, M. Cannas, V. Lysenko, A. Nazarov, Effect of Hydration Procedure of Fumed Silica Precursor on the Formation of Luminescent Carbon Centers in SiO_2:C Nanocomposites, Physica Status Solidi (a). 216,1800560 (2019).

[2] C.M. Carbonaro, R. Corpino, M. Salis, F. Mocci, S.V. Thakkar, C. Olla, P.C. Ricci, On the Emission Properties of Carbon Dots: Reviewing Data and Discussing Models, J. Carbon Res. 5, 60, (2019) .

[3] S. Stoll, A. Schweiger, Journal of Magnetic Resonance. 178, 42–55, (2006).

[4] V. Nikas, S. Gallis, M. Huang, A.E. Kaloyeros, A.P.D. Nguyen, A. Stesmans, V.V. Afanas'ev, Appl. Phys. Lett. 104, 061906, (2014).

[5] V.A. Radzig, A.A. Ischenko, Carbon in silica, Kinet Catal. 52, 316–329, (2011).

[6] G. Hochstrasser, J.F. Antonini, Surface states of pristine silica surfaces: I. ESR studies of E_s' dangling bonds and of CO_2^- adsorbed radicals, Surface Science. 32, 644–664, (1972).

Photobleaching Effects Caused by Ambient Light on the Radiation-Induced Attenuation of Germanosilicate Optical Fibers

Martin Roche[(1)(2)], Adriana Morana[(1)], Selyan Acid[(1)(3)(4)], Emmanuel Marin[(1)], Aziz Boukenter[(1)], Youcef Ouerdane[(1)], Damien Lambert[(2)], Philippe Paillet[(2)], Sylvain Girard[(1,5)].

[(1)] Laboratoire Hubert Curien, Université de Saint-Etienne, 42000, Saint-Etienne, France.
[(2)] CEA, DAM, CEA-DIF, F-91297 Arpajon, France
[(3)] CNES, 31400 Toulouse, France
[(4)] TRAD, 31670 Labège, France
[(5)] IUF, Paris, France

ABSTRACT

We demonstrate the influence of the ambient lightning on the X-ray radiation-induced attenuation (RIA) in the visible to infrared domains of germanosilicate optical fibers. RIA spectra and kinetics are then discussed depending on the illumination conditions in terms of point defects.

PACS Keywords: Ge-doped optical fibers, photobleaching, radiation effects, radiation-induced-attenuation.

1 INTRODUCTION

One among the major challenges for fiber-based technologies implementation in radiation environments concerns their transmission performance degradation due to the RIA [1]. RIA is caused by the generation of radiation-induced point defects in the silica-based core and cladding of the optical fiber, where the guided modes propagate. These point defects have optical absorption bands peaking over the whole spectrum from the infrared (IR) to the ultraviolet (UV) domains [2]. The related RIA levels and kinetics are affected by intrinsic (composition, geometry, manufacturing process) and extrinsic (probing wavelength and power, irradiation conditions, temperature) fiber parameters [3]. Optical fibers doped with germanium in their core are commonly used in telecommunications field. P-free Ge-doped fibers demonstrate a relative tolerance to radiations in the near-IR (NIR) domain, allowing their employment in harsh environments characterized by moderate dose levels (typically <100 kGy(SiO_2)) [3], [4].

Nevertheless, as already pointed out, RIA measurements can be affected by many parameters. To date, the effect of the probing light power or the influence of an additional bleaching signal has been investigated [5], [6]. Ge-doped optical fibers have been proven to be sensitive to the photobleaching (PB) effect. This phenomenon results in an RIA reduction as the injected optical energy allow recombination of radiation-induced defects. However, it has been recently demonstrated that even ambient-light can photobleach the RIA of Ge-doped optical [7], [8]. With the present study, we want to give new insights about this effect by discussing the natures of involved point defects through spectral RIA measurements.

2 EXPERIMENTAL SETUP

Irradiation experiments were performed at room temperature at the Moperix facility at LabHC, a 100kV X-ray tube with a Tungsten delivering photons with a mean energy of ~40 keV. The sample is a Ge doped fiber with a 6.33 µm core diameter, 125 µm pure silica cladding and is coated with polyimide. Fiber sample lengths from 0.3 and 30 m were coiled and exposed to a LED Flat Light. This commercial lamp was selected for its ability to vary color and intensity, enabling us to investigate the effects on the PB in more details (*the emitted spectra have been characterized and will be presented at the symposium*). RIA spectra in the visible and IR domain were measured thanks to Deuterium-Halogen white light sources and appropriate spectrometers. The dose rate was fixed at 250 mGy(SiO_2)/s during a 2.77 h irradiation in order to reach a dose of 2.5 kGy(SiO_2). The light was always ON, except for 20 min during the recovery part in order to study the stability of the involved defects. A control experiment (without light) was also performed.

3 RESULTS & DISCUSSION

Figure 1 reports the RIA spectra measured at the end of the irradiation for different experiments in which the LED was OFF or ON with blue, red, green, white color (surface emitted power close to 5 W). The bleaching of the color centers is perceptible over the whole investigated spectral range, especially with the white and blue LEDs. In agreement with [7], shorter wavelengths induce more PB effect. Concerning the visible wavelength spectrum: RIAs of the Blue and White LED experiments are relatively close (less than 15 % of difference). Those conditions induce a recovery of 60 % of transmission performances compared

with the control experiment. Red is much less effective, down to 30 % of recovery. In an interesting way, we could notice a change of NIR RIA shape with the white LED. This is directly associated with the nature and stability of the absorbing defects. Therefore, *for the symposium*, we will identify the defects that are generated by the X-rays with RIA decompositions as the sum of several Gaussian OA bands, in a similar way as previous studies [9], [10].

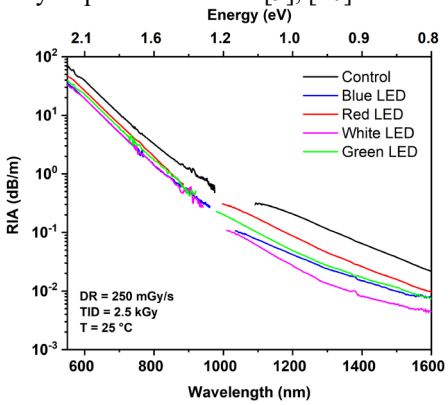

Figure 1: Spectral RIA measured at 2.5 kGy with LED ON (various colors) and LED OFF (control experiment).

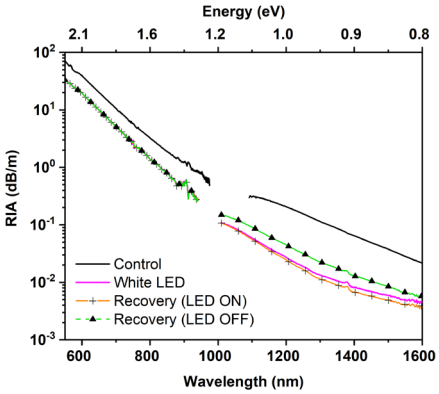

Figure 2: Spectral RIA measured at 2.5 kGy and during recovery with White LED ON and OFF.

Then, we select white LED RIA results, due to its highest PB effects, and compare in Figure 2 the RIA spectra measured at the end of irradiation and during the recovery phase for both the LED ON and OFF. Concerning the NIR spectral range, the action of turning OFF the LED during the recovery increases the RIA, reaching a higher level than the one reached at the max dose. This highlights the metastability of the involved defects in our irradiation conditions and PB effects. On the contrary, defects absorbing in the visible range appear as more stable regardless of the LED status.

Another way to analyze the results is to analyzing the 1550 nm RIA kinetics during the irradiation, as done in Figure 3. The white LED results show a RIA decrease about 90 % compared to the control experiment. Even the red LED is also quite effective by reducing the RIA about 30 %

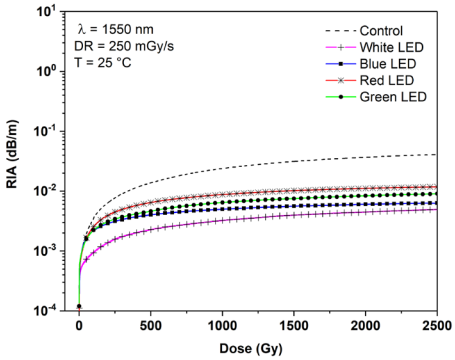

Figure 3: Online RIA kinetics at 1550 nm as a function of the dose recorded for different ambient lightning conditions.

4 CONCLUSIONS

Our study provides some additional knowledge about the effects of ambient lightning impact on RIA in Ge-doped optical fibers. These results support previous investigations as even a low energy spectrum (red LED) can induced some photobleaching (PB) effects. We recommend then to perform irradiation qualification test in dark conditions to minimize PB effects and ensure to measure RIA in the worst case scenario. For the symposium, more results will be presented and analyzed, including some Gaussian decompositions to further study the involved Ge-related defect natures and properties. More experiments will be also performed on other commercial Ge-doped optical fibers.

REFERENCES

[1] S. Girard *et al.*, "Radiation Effects on Silica-Based Optical Fibers: Recent Advances and Future Challenges," *IEEE TNS*, vol. 60, no. 3, pp. 2015–2036, Jun. 2013.

[2] E. J. Friebele and D. L. Griscom, "Color Centers in Glass Optical Fiber Waveguides," *MRS Online Proceedings Library*, vol. 61, p. 319, 1985.

[3] S. Girard *et al.*, "Overview of radiation induced point defects in silica-based optical fibers," *Rev. Phys.*, 4, 100032, 2019.

[4] M. Roche *et al.* "Combined Photobleaching and Temperature Effects on 1550 nm RIA of Germanosilicate Optical Fiber" *IEEE TNS,* 70(8) 1951–1957, 2023.

[5] F. Fricano *et al.*, "Photobleaching Effect on the Sensitivity Calibration at 638 nm of a Phosphorus-Doped Single-Mode Optical Fiber Dosimeter," *Sensors*, vol. 24, no. 17, 5547, 2024.

[6] G. Li Vecchi *et al.*, "In-situ regeneration of P-doped optical fiber dosimeter," *Opt. Lett.*, vol. 45, no. 18, p. 5201, Sep. 2020.

[7] C. Campanella *et al.*, "Influence of Ambient Light on the Radiation-Induced Attenuation of Germanosilicate Optical Fibers in the Visible and Near-Infrared Domains," *IEEE TNS*, vol. 70, no. 4, pp. 562–567, Apr. 2023.

[8] M. Roche *et al.*, "Very Low to High Dose Rate Irradiation Response of a Single-Mode Optical Fiber at Telecom Wavelengths," abstract submitted to the NSREC 2025.

[9] A. Morana *et al.*, "Origin of the visible absorption in radiation-resistant optical fibers," *OMEX,* 3(10), 1769–1776, 2013.

[10] A. Morana *et al.*, "Extreme Radiation Sensitivity of Ultra-Low Loss Pure-Silica-Core Optical Fibers at Low Dose Levels and Infrared Wavelengths," *Sensors*, 20(24), 24, 2020.

Temperature Effect on the Radiation Response of Graded Index Germanosilicate Multimode Optical Fibers

R. Pecorella[*], A. Morana[*], A. Boukenter[*], M. Cannas[**], Y. Ouerdane[*], and S. Girard[*]

[*] Laboratoire Hubert Curien : Université Jean Monnet
Saint-Étienne, France
[**]Dipartimento di Fisica e Chimica dell'Università degli Studi di Palermo
Palermo, Italy

ABSTRACT

We study how temperature affects the radiation response of commercially available graded index (GI) germanosilicate multimode optical fibers (MMOFs), under continuous X-ray exposure.

PACS Keywords: point defects, optical fibers, radiation-induced attenuation, radiation effects, temperature

1 INTRODUCTION

Since their discovery, optical fibers (OFs) have become increasingly prevalent across a wide range of applications, including medicine, sensing and dosimetry. Among these, telecommunication is arguably the domain where OFs are most dominant today. For high-speed network installations, multimode optical fibers (MMFs) are often the most cost-effective option, whereas single-mode (SM) fibers offer superior bandwidth performance and support for longer transmission distances. While the multimodal nature of these fibers amplifies the dispersion issue and strongly reduces the achievable bandwidth, precise control of the refractive index profile, designed to equalize the group velocities of the guided modes, mitigates these effects. Such fibers are known as Graded-Index (GI) MMFs, and five distinct standards have been established, ranging from OM1 to OM5 [1]. For deployment in harsh radiation environments, such as those encountered in the nuclear industry or high-energy physics, it is essential to assess the radiation response of OFs. Under ionizing radiation, the primary phenomenon that degrades their performance is radiation-induced attenuation (RIA), which corresponds to an increased signal loss caused by the formation of point defects in the pure or doped silica core and cladding of the fibers [2]. The radiation response can vary significantly depending on irradiation conditions, including the nature of the particles, total dose, and dose rate. Temperature also plays a critical role in determining system performance. Operating temperatures can span a wide range, from the extremely low temperatures encountered in space missions to the high ones expected in next-generation nuclear power plants, where sensors must function reliably at up to 800°C for reactor core monitoring. In this work we compare the RIA levels of the OM fibers at different temperatures, under continuous X-Ray exposure.

2 MATERIALS AND METHODS

The samples analyzed in this study are GI-MM silica-based optical fibers with germanium-doped cores, conforming to the OM1 through OM5 standards. OM1 has a core size of 62.5 µm, it can support up to 10 Gbit Ethernet at lengths of up to 33 meters and it commonly uses a LED light source. The remaining OM fibers all have a 50 µm core diameter, and as the classification progresses from OM2 to OM5, they offer increasing bandwidth capacity and reduced signal attenuation.

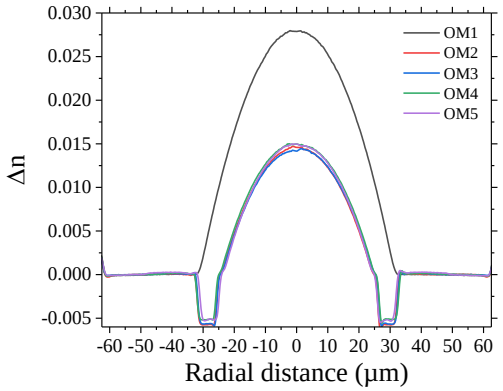

Fig. 1. Refractive index profiles of the OM1 through OM5 optical fibers.

Fig. 1 shows the refractive index profiles of the fibers under test (FUD). OM1 is the only fiber with a distinct profile, due to a higher concentration of germanium in the core and the absence of fluorine as a codopant. The latter, present in the other fibers, induces a dip in the refractive index at approximately 25 µm from the core center.

To measure the RIA during continuous X-rays irradiation at different temperatures, the FUT were arranged in a monolayer coil on a heating/cooling plate set to either -40°C, 35°C or 80°C. All the irradiation runs were performed at a dose rate of 6 Gy(SiO_2)/s, up to a total ionizing dose (TID) of ~109 kGy, at the Idefix facility at the Hubert Curien Laboratory in Saint-Etienne, France. Signal detection was

carried out using halogen and deuterium light sources with spectrometers covering the visible and near-infrared ranges.

3 RESULTS AND DISCUSSION

The online RIA measurements conducted on all the samples revealed two distinct groups of radiation response: OM1, and the other fibers. Therefore, to simplify the analysis, only OM1 and OM2 fibers are considered in the following discussion. Fig. 2 presents, on a semi-logarithmic scale, the RIA of these two fibers as a function of the X-ray dose and the time following the end of irradiation, measured at 1310 nm, one of the typical telecommunication windows, at three different temperatures.

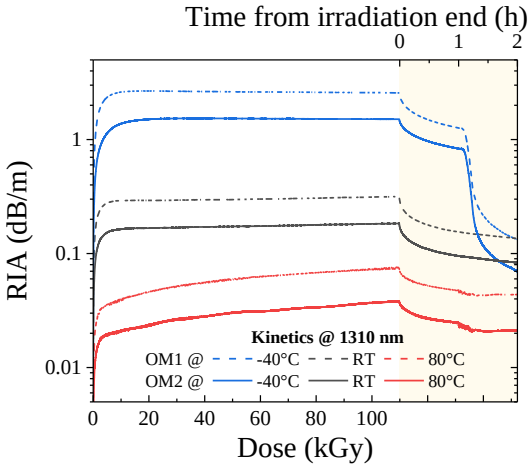

Fig. 2. RIA kinetics at 1310 nm of the OM1 (dashes) and OM2 (lines) fibers at three different temperatures (- 40°C in blue, RT in black and 80°C in red), during and after the irradiation (yellow shaded part) up to a TID of 109 kGy.

It shows a clear dependence of RIA on irradiation temperature, with lower temperatures resulting in higher RIA values. Specifically, when performing the irradiation at -40°C, the induced attenuation at the end of the exposure (~109 kGy) increases by a factor of 8 for both OM1 and OM2 fibers compared to RT. Conversely, at 80°C, the attenuation decreases by a factor of 4 relative to RT. Furthermore, at this temperature, the RIA increases more slowly toward a plateau, compared to the other conditions, likely due to a bleaching effect induced by the higher temperature, which competes with the radiation-induced generation of defects. During the recovery phase, following the end of irradiation, indicated by the faded yellow area in Fig. 2, all RIA curves decrease by varying percentages depending on temperature and wavelength (not shown in this abstract). Notably, when the temperature rises from −40°C to approximately room temperature, the RIA drops significantly, reaching levels comparable to those observed after the irradiation at RT. This behavior suggests that the defects responsible for the absorption are unstable at room temperature.

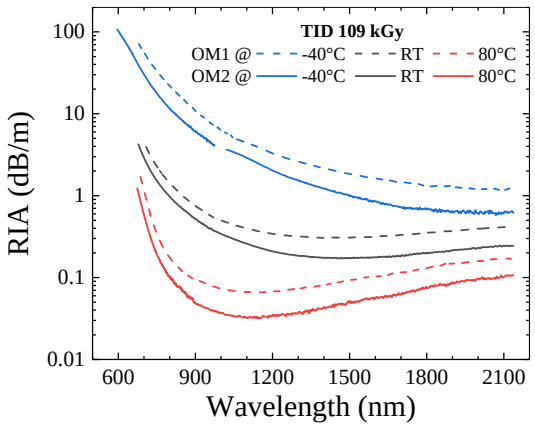

Fig. 3. RIA spectra of the fibers OM1 (dashes) and OM2 (lines) at a TID of 109 kGy, at three temperatures: -40°C in blue, RT in black and 80°C in red.

Fig. 3 shows the RIA spectra of the OM1 and OM2 samples at 109 kGy, measured at the three investigated temperatures. Across both the visible and infrared ranges, the temperature dependence is consistent with the trend observed at 1310 nm. It should also be noted that the RIA is significantly higher in the visible range compared to the IR range. We will perform a detailed analysis via spectral decomposition to better understand the origin of the attenuation across different wavelengths and temperatures.

4 CONCLUSION

The samples studied in this work are Ge-doped GI-MM silica optical fibers conforming to the OM1 through OM5 standards. To investigate the temperature dependence of their radiation response, we performed online spectral RIA measurements in both the visible and infrared ranges at a dose rate of 6 Gy(SiO_2)/s, up to a TID of 109 kGy, at −40°C, RT and 80°C. Consistent with the findings of Morana et al. [3] on single-mode Ge-doped optical fibers, we observed that lower temperatures result in higher signal attenuation, while higher temperatures lead to lower RIA levels. To gain a deeper understanding of the underlying physical mechanisms and point defects, a spectral decomposition of the RIA will be carried out in the final version of this paper.

REFERENCES

[1] https://www.zion-communication.com/Differences-between-OS1-OS2-OM1-OM2-OM3-OM4-and-OM5-id3002360.html, Accessed on: November 18, 2024.

[2] S. Girard et al., “Recent advances in radiation-hardened fiber-based technologies for space applications,” J. Opt., vol. 20, no. 9, p. 093001, 2018.

[3] A. Morana et al., “Temperature Dependence of Low-Dose Radiation-Induced Attenuation of Germanium-Doped Optical Fiber at Infrared Wavelengths,” IEEE Trans. Nucl. Sci., vol. 69, no. 3, pp. 512–517, 2022.

Tuesday, June 24th

Session #4

Luminescence Spectroscopy

Marco Cannas, Univ. Palermo

Multifunctional Lanthanide-doped Oxyfluoride Nanophosphors for Luminescence Thermometry and Latent Fingerprint Detection

H. C. Swart*, G. B. Nair, S. Tamboli

* Department of Physics, University of the Free State, P. O. Box 339, Bloemfontein 9300, South Africa.

ABSTRACT

Lanthanide-doped nanophosphors have shown versatile applications in multifarious sectors. In this study, lanthanide-doped oxyfluoride phosphors were synthesized using microwave-assisted hydrothermal route and investigated for their applications in luminescence thermometry and latent fingerprint detection (LFP). LaOF:Yb^{3+},Tm^{3+} upconversion nanophosphors (UCNPs) exhibited blue and near-infrared (NIR) upconversion luminescence (UCL) under a NIR 980 nm excitation. These UCNPs exhibited temperature-dependent UCL, which was exploited for remote thermometry in the temperature range of 303 – 473 K using the fluorescence intensity ratio (FIR) technique. Meanwhile, YOF:Tb^{3+},Eu^{3+} nanophosphors showed their elegance in LFP detection on multiple surfaces with complex appearance and diverse colors. With their color-tuning features, YOF:Tb^{3+},Eu^{3+} nanophosphors provided higher image contrast and high spatial resolution of the fingerprint ridges, revealing most of the details categorized under levels 1, 2 and 3. These two findings underline the potential of lanthanide-doped oxyfluoride nanophosphors as multifunctional materials for remote luminescence thermometry and high-contrast multispectral LFP detection.

PACS Keywords: Lanthanides, oxyfluorides, thermometry, latent fingerprint detection, photoluminescence.

INTRODUCTION

Upconversion nanoparticles (UCNPs) can convert two or more low-energy photons into one high-energy photon by a non-linear optical process called upconversion luminescence (UCL). These UCNPs have a wide range of applications in the field of bio-imaging [1,2], bio-markers [3], thermometry [4,5] etc. Nanophosphors containing a pair of lanthanide ions such as Yb^{3+}-Tm^{3+}/ Yb^{3+}-Er^{3+}/ Yb^{3+}-Ho^{3+} showed UCL by absorbing near infrared (NIR) photons and emitting visible photons. Fluorides ($NaYF_4$/YF_3) and oxyfluorides (LaOF/YOF) possess low phonon energies, wide energy bandgaps and high chemical and physical stability, which makes them suitable and efficient host for achieving UCL [6]. Herein, we have prepared LaOF:Yb^{3+}, Tm^{3+} UCNPs using the microwave-assisted hydrothermal method for remote thermometry application by exploring their temperature-dependent UCL properties. These UCNPs acted as a probe to sense the temperature remotely. Fluorescence intensity ratio (FIR), which is ratio of the UCL intensities of two thermally-coupled (TCL) or non-coupled (NTCL) energy levels, varied with the surrounding temperature. Variation of FIR with respect to temperature was used for sensing the temperature change.

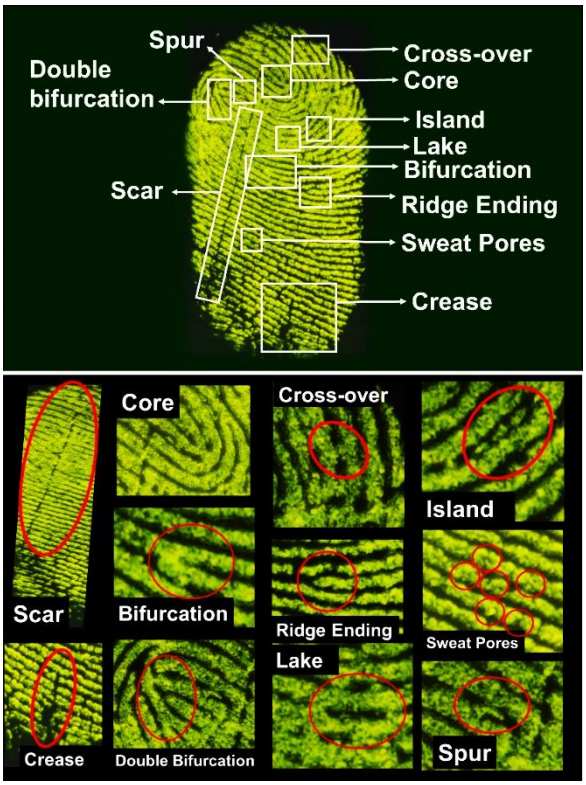

Figure 1: Levels 1, 2, and 3 features of an LFP developed using YOF:0.01 Tb^{3+}, 0.002 Eu^{3+} nanophosphor on a glass substrate and illuminated under a 254 nm UV lamp [7].

Down-shifting (DS) color-tunable YOF:Tb^{3+}, Eu^{3+} nanophosphor was also prepared by the same approach. These nanophosphors exhibited high photoluminescence quantum yield (PLQY) approximately unity. Their color tuning feature was explored to detect the latent fingerprints (LFPs) generated on multi-surfaces with complex topology, as shown in Figure 1. As shown in Figure 2, these color tunable nanophosphors absorbed photons in the ultraviolet (UV) region and emitted in the visible region ranging from green to yellow to red depending on the ratio of Tb^{3+} to Eu^{3+} concentration. Although many reports on the LFP detection using singly doped phosphors are available in the literature, the color-tunable feature of these nanophosphors provides an added advantage through ultra-sensitive detection of LFPs with reduced background interference on colored substrates.

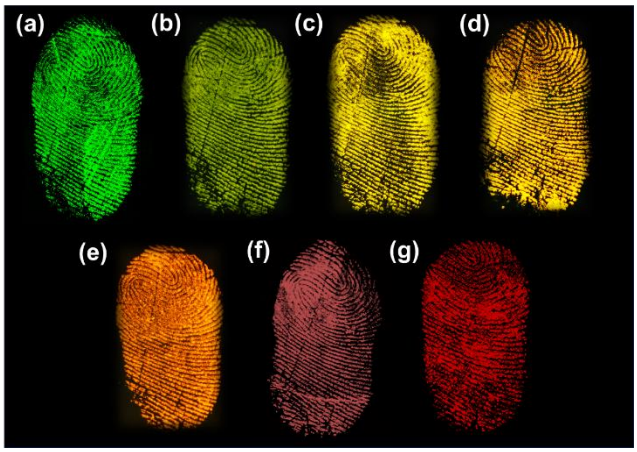

Figure 2: Digital photographs of LFPs illuminated under a UV lamp showing the color tunable feature of YOF: 0.01 Tb^{3+}, *x* Eu^{3+} nanophosphors, where (a) *x* = 0, (b) *x* = 0.001, (c) *x* = 0.002, (d) *x* = 0.005, (e) *x* = 0.01, (f) *x* = 0.02 and (g) YOF: 0.01 Eu^{3+} [7].

Particle size control is also an essential criterion to use nanophosphors for various applications. Nanoparticles of oxyfluorides can be grown in different shapes and sizes, such as rods, spheres or cubes, depending on the method of synthesis [8]. The synthesis method plays a crucial role in obtaining uniform particle size distribution of nanophosphors. In this work, we have selected microwave-assisted hydrothermal synthesis method to prepare LaOF:Yb^{3+}, Tm^{3+} UCNPs and YOF:Tb^{3+}, Eu^{3+} nanophosphors. This method gives advantages of both microwave as well as hydrothermal processes. Microwave radiation enables dielectric heating of the molecule which ensures uniform chemical reaction through the reacting mixture which leads to uniform particle size distribution. In a short period of time, high temperature and pressure can be attained. The synthesized LaOF:Yb^{3+}, Tm^{3+} UCNPs and YOF:Tb^{3+}, Eu^{3+} nanophosphors were characterized by different characterization techniques such as X-ray powder diffraction (XRPD), Field-emission scanning electron microscopy (FE-SEM) and Diffuse Reflectance spectroscopy (DRS) for structural, morphological and optical studies. UCL and downshifting photoluminescence (DSPL) spectra were recorded for LaOF:Yb^{3+}, Tm^{3+} UCNPs and YOF:Tb^{3+}, Eu^{3+} nanophosphor, respectively, for determining their fluorescence properties. These materials have shown potential advancements in the fields of remote thermometry and forensic applications through their redefining luminescence characteristics.

REFERENCES

[1] X. Wu, Y. Zhang, K. Takle, O. Bilsel, Z. Li, H. Lee, Z. Zhang, D. Li, W. Fan, C. Duan, E.M. Chan, C. Lois, Y. Xiang, G. Han, ACS Nano 10 (2016) 1060–1066.

[2] Y. Liang, R. An, P. Du, P. Lei, H. Zhang, Nano Today 48 (2023).

[3] A. Hlaváček, Z. Farka, M.J. Mickert, U. Kostiv, J.C. Brandmeier, D. Horák, P. Skládal, F. Foret, H.H. Gorris, Nat. Protoc. 17 (2022) 1028–1072.

[4] G.B. Nair, S. Tamboli, R.E. Kroon, H.C. Swart, Mater. Today Chem. 29 (2023) 101463.

[5] A. Pandey, V.K. Rai, V. Kumar, V. Kumar, H.C. Swart, Sensors Actuators B Chem. 209 (2015) 352–358.

[6] R. Li, L. Li, W. Zi, J. Zhang, L. Liu, L. Zou, S. Gan, New J. Chem. 39 (2015) 115–121.

[7] S. Tamboli, G.B. Nair, R.E. Kroon, L.J.B. Erasmus, H.C. Swart, Dalt. Trans. 53 (2024) 11736–11749.

[8] T. Grzyb, M. Węcławiak, T. Pędziński, S. Lis, Opt. Mater. (Amst). 35 (2013) 2226–2233.

Sol-gel derived Luminescent Coatings Incorporating $YVO_4:Eu^{3+}$ Nanocrystals for Narrow-Red Emission

Arjun Babu*, François Réveret*, Federico Cisnetti*, Kevin Lemoine*, Damien Boyer*

* *Université Clermont Auvergne, Clermont Auvergne INP, CNRS, Institut de Chimie de Clermont-Ferrand (ICCF), F-63000, Clermont-Ferrand, France*

1. INTRODUCTION

In recent years, the emergence of luminescent coatings with exceptional quantum yield has marked a pivotal advancement in the pursuit of miniaturizing optical systems like LED lighting and display devices [1]. Herein, we have studied the influence of NPs size on the optical properties of luminescent coatings. To this end, two types of $YVO_4:Eu^{3+}$ NPs, with average diameters of 10 nm and 340 nm, were synthesized by two different hydrothermal processes [2,3]. This lanthanide ions doped vanadate is well-known to produce a strong narrow red emission upon UV excitation. Furthermore, an inorganic-organic hybrid material was developed using the sol-gel synthesis method. The precursor sol was prepared through the hydrolysis and condensation of 3-glycidoxypropyltrimethoxysilane (GPTMS) combined with zirconium propoxide, which was chemically stabilized using acetylacetone as a complexing agent. Afterwards, these $YVO_4:Eu^{3+}$ NPs were incorporated in this hybrid material with different loading rates and then luminescent coatings were achieved by spin-coating these suspensions onto glass substrates. Finally, the angular emission distribution was analyzed to estimate the photons trapped inside the structure depending on the surface roughness and the NPs size.

PACS Keywords: $YVO_4:Eu^{3+}$ nanoparticles, hydrothermal synthesis, hybrid material, sol-gel, luminescent coatings

2. EXPERIMENTAL SECTION

2.1. Synthesis of $YVO_4:Eu^{3+}$ Nanoparticles

Eu-doped YVO_4 nanoparticles were synthesized by two different hydrothermal protocol. In the first synthesis (S1-synthesis), a solution containing Y, Eu, and citrate was mixed with Na_3VO_4 at pH 13 and aged at 90°C. The mixture was then hydrothermally treated at 180°C for 15 hours, followed by centrifugation, washing, and drying to obtain the final product (S1-nanoparticles) [2]. In the second synthesis (S2-synthesis), Y and Eu precursors were hydrothermally treated at 200°C for 1 hour. The product was purified using etidronic acid under acidic conditions, followed by alkalization, centrifugation, washing, and drying (S2-nanoparticles) [3]. Various doping concentrations of 0% (undoped), 5% and 15% by using two different synthesis protocol.

2.2. Synthesis of hybrid material

Hybrid material was synthesized using sol-gel method. 3-Glycidyloxypropyltrimethoxysilane was hydrolyzed in ethanol with hydrochloric acid to form sol 1. Separately, zirconium tetra-n-propoxide was stabilized with acetylacetone in ethanol and added to sol 1, stirred overnight to obtain sol 2, which was stored at 5°C [4].

3. RESULTS AND DISCUSSION

3.1. Characterization of S1- and S2-Nanocrystals

The synthesized S1 and S2-$YVO_4:Eu^{3+}$ nanoparticles were structurally and morphologically characterized using XRD, Raman, FTIR analyses and TEM analysis. Eu^{3+} concentration was evidenced by elementary analysis and Rietveld refinement. The average diameter of the S1 and S2 nanoparticles were calculated to be 340 nm and 10 nm (**Figure 1**).

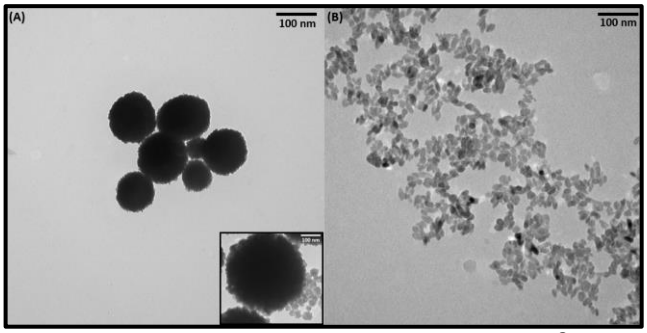

Figure 1. (A) TEM Images of S1 and S2-$YVO_4:Eu^{3+}$ NCs.

The emission spectra are dominated by strong $^5D_0$-$^7F_{2,4}$ electric-dipole transitions at 619 nm and 698 nm, respectively, intensified by the D_{2d} site symmetry of Eu^{3+} (**Figure 2**). Weaker $^5D_0$-$^7F_{1,3}$ magnetic-dipole transitions also appear. In the excitation spectra, a broad absorption

band appears between 250 and 375 nm in the narrow band UVB range, corresponding to charge transfer excitation from the oxygen ligands to the central vanadium atom in the VO_4^{3-} groups [5].

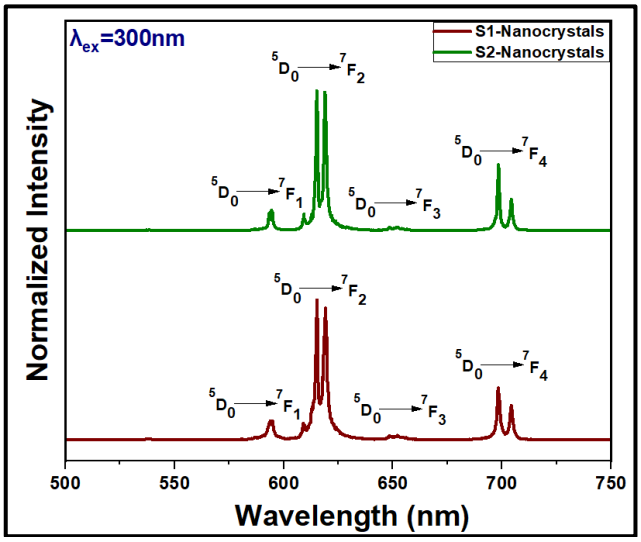

Figure 2. Emission spectra of S1- and S2- nanocrystals

Quantum yield studies were conducted to assess the efficiency of the synthesized nanocrystals (NCs). The external photoluminescence quantum yield (ePLQY) of S1-$YVO_4:Eu^{3+}$(5 %) and S2-$YVO_4:Eu^{3+}$(5 %) NCs were 27.2% and 43.9%, respectively. Interestingly, the smaller S2 NCs showed higher ePLQY, aligning with decay data. This improvement is likely due to better crystallinity and lesser surface defects, even without thermal treatment.

3.2. Characterization of luminescent coatings

The preparation of the hybrid material through a sol-gel process and the subsequent fabrication of luminescent coatings are realized with loading concentration of 2 wt.% and 5 wt.% in $YVO_4:Eu^{3+}$ NCs (**Figure 3**). The process ensures uniform distribution of nanocrystals within the hybrid matrix. Their thickness was determined by profilometry and micro-reflectivity measurements. Furthermore, the effect of mass loading and nanoparticle size on the optical properties of luminescent films was also investigated by conducting photoluminescence and UV-visible spectroscopies. Coatings exhibit bright red emission, confirming effective incorporation of $YVO_4:Eu^{3+}$ NCs. Homogeneity of luminescent coatings assessed using a video colorimeter.

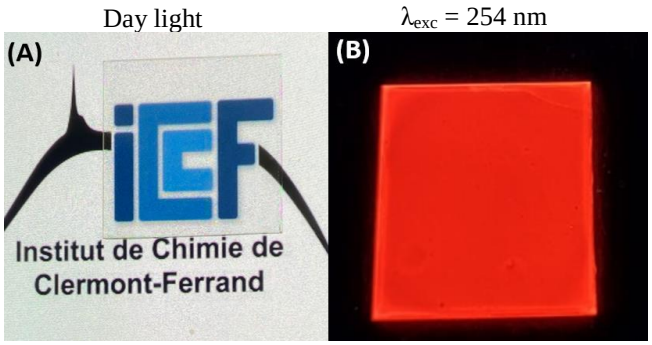

Figure 3. (A) Image of prepared transparent hybrid material coating and (B) Image of nanophosphor encapsulated coating.

4. CONCLUSION

In this study, we developed and characterized luminescent coatings by embedding $YVO_4:Eu^{3+}$ nanocrystals into a hybrid sol-gel matrix. We examined how variations in nanocrystal size and synthesis conditions influence their optical properties, aiming to optimize performance for potential photonic applications. The study concludes with insights into the trade-offs between transparency, quantum yield, and luminescence intensity in luminescent coatings. Future research aims to enhance photon scattering and reduce losses through innovative strategies. Smaller nanoparticles (S2) show higher ePLQY due to improved crystallinity and ligand protection. Larger nanocrystals (S1) exhibit reduced photon leakage and higher luminescence intensity. Future strategies include integrating metallic nanoparticles to enhance photon scattering and minimize guiding losses.

REFERENCES

[1] Huayna Terraschke et.al , *Chem. Rev*. 2015, 115, 20, 11352–11378.
[2] Chen.et.al Phys. Chem. Chem. Phys., 2010, 12, 7775.
[3] K. Riwotzki et.al. J. Phys. Chem. B 1998, 102, 10129.
[4] Toide et.al. J Sol-Gel Sci Technol 104, 478 (2022).
[5] Arnaud Huignard et.al, J. Phys. Chem. B 2003, 107, 6754-6759.

Optical Performances of Chromophores Embedded in Metal Organic Frameworks for Photonics in Harsh Environments

G. Ficarra[*], V. De Michele[**], R. Pecorella[**], L. Weninger[**], Y. Ouerdane[**], M. Cannas[*], F. Messina[*], A. Boukenter[**], A. Sciortino[*] and G. Buscarino[*]

[*]Department of Physics and Chemistry "Emilio Segrè", University of Palermo, Via Archirafi 36, 90123, Palermo, Italy
[**]Université Jean Monnet, CNRS, IOGS, Laboratoire Hubert Curien UMR 5516, 42000, Saint-Etienne, France

ABSTRACT

Fluorescent organic dyes are extremely useful and versatile for a wide range of applications. However, their long-term use, especially in harsh environments, is limited by stability issues. These problems can be addressed by encapsulating dyes within hosting platforms, such as Metal-Organic Frameworks (MOFs), which are well known for their sorption capacity and stability, even in extreme environments. In the present work, we investigate the optical properties of Rhodamine B and green emitting Carbon nanodots, when combined with Zr-based MOF-808. Finally, we showed that these nanocomposites maintain their optical properties even after exposure to UV, X-rays, and proton beam, positioning them as promising candidates for photonics applications in harsh environments.

PACS Keywords: Fluorescent organic dyes, Metal Organic Frameworks, Shielding effects, Photonics applications

1 INTRODUCTION

Fluorescent organic dyes are known for their accessibility, low cost, and versatility in various fields such as sensing, imaging, dye-sensitized solar cells, etc. However, their prolonged use, especially in extreme environments, is significantly hindered by stability issues. A possible approach to overcome these issues is to encapsulate the chromophores within hosting platforms that impart their intrinsic stability properties to the guest molecules [1].

Metal-organic frameworks (MOFs) are a class of hybrid porous nanocrystals composed of organic ligands that coordinate metaloxoclusters. The presence of pores imparts to MOFs significant values of internal surface area ($10^2\ m^2/g$), which ensures remarkable particle trapping properties [2]. The encapsulation of chromophores within the cavities of MOFs enables the creation of novel emitting nano systems, leveraging the stability and shielding properties of MOFs. Moreover, the trapping strategy effectively suppresses aggregation caused quenching (ACQ), a phenomenon that typically prevents many chromophores from exhibiting solid-state emission, thereby opening new opportunities for photonic applications. Some studies in the literature report MOFs that retain their crystalline structure when exposed to ionizing radiation [3]. Leveraging these studies, we have combined Rhodamine B (RhB) molecules and Carbon Nanodots (CDs) within the cavities of MOF-808, investigating the optical performance of these composite nano systems after exposure to UV radiation, X-rays, and proton beams. We studied the optical properties using steady-state and time-resolved spectroscopy techniques and estimated the absolute Quantum Yield (QY) of the materials exposed to radiation to compare the efficiency of their photoluminescent properties. The photostability exhibited by these guest@host systems holds significant promise for sensing applications in extreme environments. Alternatively, they may be integrated into Dye-Sensitized Solar Cells, offering potential for enhanced performance in such devices [4].

2 EXPERIMENTAL

Steady-state and time-resolved photoluminescence measurements were recorded using an intensified charge-coupled device (CCD) camera. The excitation wavelengths could be varied using a tunable laser system composed of an optical parametric oscillator (OPO) pumped by a Q-switched Nd:YAG laser, delivering 5 ns pulses at a repetition rate of 10 Hz, with an energy of 0.1 mJ. The same laser source was used to perform UV irradiation, while simultaneously monitoring the optical response *in situ*. The optical properties of the materials exposed to X-ray and proton beam radiation were evaluated after irradiation. The X-ray irradiation was performed at a dose rate of 5 Gy(SiO_2)/s, reaching three different total ionizing doses (TID) at LabHX facility at the Hubert Curien Laboratory in Saint-Etienne, France. Proton beam irradiation was carried out at the Centro Nacional de Aceleradores (CNA) in Seville, Spain. The incident protons had an energy of 15 MeV and were

delivered at a constant rate. The exposure time was varied, ranging from 10 to 1000 s, to modulate the total dose.

3 RESULTS

We investigated the effects of encapsulating RhB molecules inside MOF pores when the sample is irradiated with intense UV laser light. Monitoring *in situ* the emission

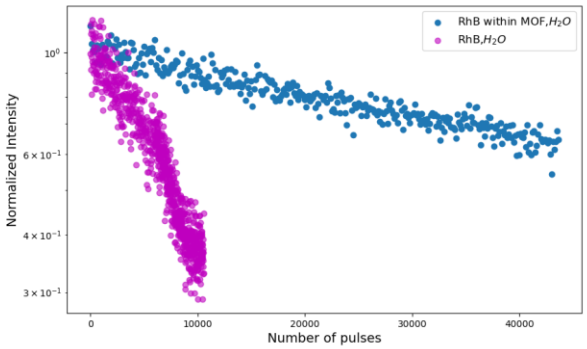

Figure 1: Photobleaching kinetics of bare RhB (pink dots) and RhB encapsulated within the cavities of MOF-808 (blue dots).

peak at 595 nm of RhB during irradiation with 280 nm laser pulses, we verified that free RhB molecules in water undergo a photobleaching process as a function of the number of pulses (Figure 1). For the bare dye in water, the number of pulses required to reduce the intensity by a factor of 1/e is approximately 4600, whereas RhB embedded within the MOF-808 matrix, acting as a shield, requires around 41000 pulses to experience the same reduction. The encapsulation of RhB inside the MOF pores enhances its resistance to UV irradiation.

We checked for the photostability of CDs when embedded within MOF-808 after proton beam irradiation. We collected steady-state luminescence spectra as a function of the radiation dose (Figure 2). The emission spectra obtained exhibit a peak centered at 515 nm. Upon normalizing the spectra to the area under the peak, it can be concluded that the shape of the emission remains unaffected by proton irradiation and is independent of the deposited dose.

Time-resolved photoluminescence studies revealed that the decay kinetics of the emission peak are also independent of the radiation dose and follow the same behavior as the untreated samples. Absolute quantum yield (QY) should be estimated to verify whether the emission efficiency remains unchanged regardless of the total ionizing dose (TID).

The same optical characterization experiments were performed for RhB within the cavities of the MOF-808. The calculation of the absolute quantum yield (QY) demonstrated a clear shielding effect of the MOF, even in the case of X-ray irradiation.

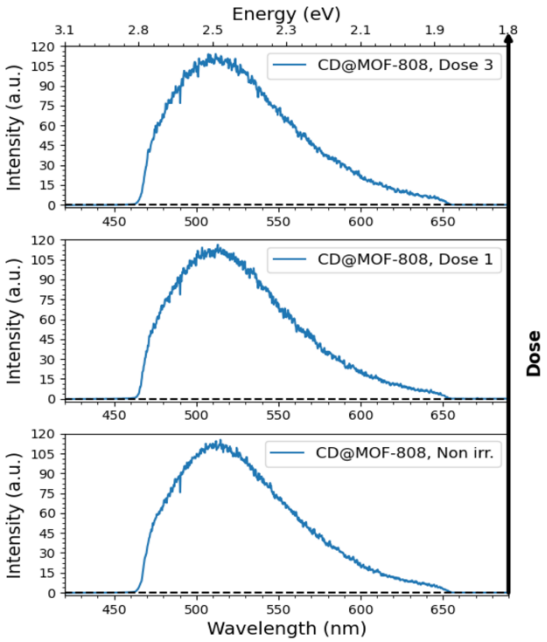

Figure 2: Photoluminescence spectra of CDs@MOF-808 excited at 430 nm as a function of dose. Starting from the bottom are reported the emission of non-irradiated samples, lower and higher dose.

4 CONCLUSIONS

In the present study, we investigated the potential benefits of encapsulating organic chromophores within the cavities of MOFs. By incorporating RhB and CDs into MOF-808, we developed novel luminescent nanosystems that exhibit solid-state luminescence properties, owing to the suppression of ACQ. Our results demonstrate that the MOF matrix provides photoprotection to the encapsulated chromophores against UV, X-ray, and proton beam irradiation, thus making these systems particularly promising for applications in sensing or dye-sensitized solar cells under extreme conditions.

REFERENCES

[1] M. Vellaichamy et al., *Liquid Crystals*, 50, 953-956, 2023.

[2] M. Fairley et al., *Chemistry of Materials*, 33, 9285-9294, 2021.

[3] J. L. C. Rowsell et al., *Microporous and Mesoporous Materials*, 73, 3-14, 2004.

[4] M. Grätzel., *Journal of Photochemistry and Photobiology C: Photochemistry Reviews*, 4, 145-153, 2003

Wednesday, June 25th

Session #5

Radioluminescence

Hugo Boiron, Exail

Optical Fiber-based Dosimetry for 15 MeV Proton Beam Monitoring

F. Fricano[*], L. Weninger[*], A. Morana[*], A. Romero Maestre[**], P. Martin Holgado[**], J. De Martin Hernandez[**], Y. Morilla Garcia[**], D. Lambert[***], P. Paillet[***], H. El Hamzaoui[****], B. Capoen[****], M. Bouazaoui[****], E. Marin[*], Y. Ouerdane[*], A. Boukenter[*], S. Girard[*†]

[*]Université Jean Monnet Saint-Etienne, Laboratoire Hubert Curien, F-42023, Saint-Etienne, France
[**]Centro Nacional de Aceleradores, Universidad de Sevilla E-41092 - Sevilla (Spain)
*** CEA, DAM, DIF, 91297 Arpajon, France
****Univ-Lille, CNRS, UMR8523 - PhLAM F-59000 Lille, France
†Institut Universitaire de France (IUF) 75005 Paris, France.

ABSTRACT

This abstract presents the first results regarding the possibility of monitoring a low energy 15 MeV proton flux at the Centro Nacional de Aceleradores (CNA) cyclotron proton facility, offering improved precision and real-time monitoring through the use of radioluminescent optical fibers.

PACS Keywords: optical fibers, radioluminescence, proton, dosimetry

1 INTRODUCTION

Among the main challenges in the field of dosimetry is the ability to measure particle fluxes—such as those found in nuclear reactors or particle accelerators—with high precision and in real-time. One of the most promising technologies for this purpose is optical fibers, which offer numerous advantages, including ease of use, simple setup, and straightforward calibration procedures. By exploiting radiation-induced effects in optical fibers—such as Radiation induced Attenuation (RIA) and Radiation Induced Luminescence (RIL) produced by ionizing radiation—it is possible to correlate them with the impacting ionizing particles fluxes [1]. Promising results have already been reported for both proton and neutron monitoring in various facilities as the ones in TRIUMF [2] and ENEA [3]. In this study, we propose the use of optical fibers as an advanced dosimetric system for the Centro Nacional de Aceleradores (CNA) facility, where a proton beam line is available for several research activities, spacing from materials science, biomedicine and environmental science [4].

In this study, we propose the use of RIL-based sensors as cerium (Ce)-doped optical fibers. Monte Carlo simulations have already demonstrated the establishment of electronic equilibrium at 15 MeV, despite the compact size of the proposed sensor [2]. Pre-treatment strategies, such as pre-irradiating the fibers, have shown several benefits, including enhanced sensitivity to flux variations. This justifies a direct comparison with pristine, never-irradiated fibers, to highlight the effects of cumulative ionizing dose and to provide insight into their long-term performance for extended operational use.

2 MATERIALS & METHODS

The tested samples are silica-based optical fibers in which cerium ions were incorporated using the sol-gel technique [5], performed by the PhLAM Laboratory of Lille (France). The fiber presents a ~125 µm diameter pure silica core, whose the 52 µm inner diameter was doped with 0.07 wt% of Ce. They are coated with a first low refractive index material, to ensure the light guidance in the silica core, and with a second coating, to enhance their mechanical strength. Specifically, we tested one pristine sample (never exposed to radiation) and one pre-irradiated sample, which had been exposed to X-rays up to a Total Ionizing Dose (TID) of 500 kGy(SiO_2).

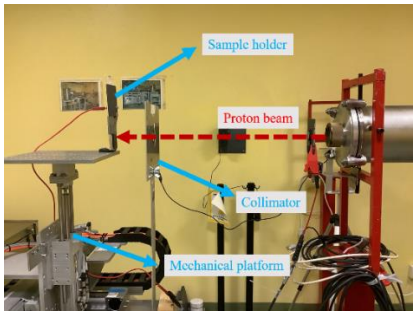

Figure 1: Schematic setup in the CNA irradiation chamber.

2.1 Proton beam facility

The measurements were carried in the CNA (Sevilla, Spain). The protons are produced by a cyclotron machine able to accelerate protons up to 15 MeV. The extracted beams are dedicated to radioisotopes production or, as in our case, to the research beam line. The produced protons reach the irradiation chamber where we put the samples on a dedicated and manageable platform. In Figure 1 is shown the general scheme in the irradiation chamber. The beam passing through the collimator is perfectly homogeneous within an

area of 15 mm in diameter, but it can be considered uniform over an area up to 2 cm in diameter. The collimator act also as electric counter to have the information about the proton flux. The fluence is deduced as simple multiplication of the flux by the run duration time.

2.2 RIL setup

The 2 cm-long samples were put on the previously mentioned sample holder and aligned with the collimator-beam axis through mechanical adjustments of the mobile platform. Within the same irradiation spot, it was possible to place two fibers in parallel, allowing for a simultaneous study of their responses. The pigtails spliced to each probe were connected to dedicated signal transmission cables, optimized for signal transport along the bunker of the irradiation chamber to the acquisition system. The latter consisted of two photomultiplier tubes (PMTs) capable of collecting photons in the visible range. Using two identical detectors, we simultaneously monitored pristine and pre-irradiated fibers under the same conditions. We followed the RIL kinetics using a gate time of 200 ms.

3 RESULTS & DISCUSSION

Figure 2 shows an example of the normalized RIL on both fibers for five runs acquired under different proton fluxes. These were not selected in a specific order other than to test the flux monitoring capability at a fixed energy of 15 MeV. During individual runs, the signal is not constant but exhibits several small fluctuations caused by an unknown periodicity of the facility. In the final article, this periodic signal will be analyzed to estimate its frequency and provide additional insight into the real-time monitoring capabilities. The normalization highlights slight differences between the two sensors that may arise from physical effects such as the bright burn effect or attenuation caused by RIA at higher flux levels (and thus higher dose rates). Parallel monitoring indeed allows us to distinguish between variations due to changes in the facility beam flux—which affect both fibers equally—and those caused by the different pre-irradiation doses of the two fibers. In Figure 3, the RIL levels measured during all the runs of the irradiation campaign are correlated with the proton flux values provided by the facility. More data points are available for the pre-irradiated fiber because it was also used as a reference in additional runs involving comparisons with other differently doped fibers, whereas the pristine fiber was tested in parallel only with its pre-irradiated counterpart. The data have been corrected to account for the effect of the attenuator placed in the acquisition chain to not reach the saturation value of the PMTs. The response appears linear for both fibers, allowing a linear fit to be performed and thus enabling the calibration of the fiber.

We obtained a sensitivity of 3.5×10^{-3} counts p^{-1} cm^2 for the pristine fiber and almost the double, 6.8×10^{-3} counts p^{-1} cm^2, for the pre-irradiated one, evidencing the enhanced sensitivity due to pre-irradiation. In the final article, the calibration performed on the same probes under X-rays will be discussed.

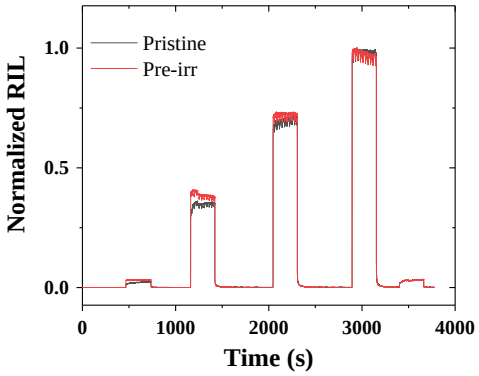

Figure 2: Normalized RIL for few random runs acquired under different proton fluxes.

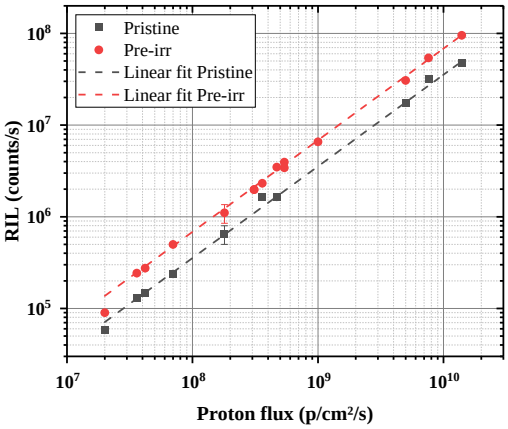

Figure 3: RIL signal as a function of the proton flux values provided by the CNA facility.

4 CONCLUSIONS

We introduced the concept of using optical fibers to measure the 15 MeV protons flux, offering a potential real-time solution for dosimetry at the CNA facility. The final article will present a more in-depth study of the advantages and limitations of such fiber dosimetry for low-energy beam monitoring, in particular by extrapolating the range of flux and energies that it should be possible to cover.

REFERENCES

[1] S. Girard, IEEE Trans. Nucl. Sci. (2024).
[2] F. Fricano *et al.*, IEEE Transactions on Nuclear Science 71 (2024) 1829–1836.
[3] L. Weninger *et al.*, Results in Optics 19 (2025) 100807.
[4] M. A. Respaldiza *et al.*, Nuclear Instruments and Methods in Physics Research Section B: Beam Interactions with Materials and Atoms 266 (2008) 2105–2109.
[5] H. El Hamzaoui *et al.*, Mater. Res. Express 3 (2016).

Radiation-Induced Luminescence Study in Different Low-OH Pure Silica Core Optical Fibers

Selyan Acid[*,**,***], Adriana Morana[**], Nourdine Kerboub[*], Marine Aubry[***], Julien Mekki[*], Jeremy Guillermin[***],Maxime Darnon[**], Youcef Ouerdane[**], Aziz Boukenter[**], Sylvain Girard[**,****]

[*]French Space Agency (CNES), 31400, Toulouse, France
[**]Laboratoire Hubert Curien UMR5516, Université Jean Monnet,42000, Saint-Etienne, France
[***]TRAD Test & Radiations,31670, Labège, France
[****]Institut Universitaire de France (IUF),75005, Paris, France

ABSTRACT

This work investigates the influence of pre-irradiation and Numerical Aperture (NA) on the radiation-induced luminescence (RIL) signal of low-OH pure silica core (PSC) optical fibers (OFs) tested under X-rays. RIL intensity increases with both the NA and the pre-irradiation dose (up to 2 MGy). The measured RIL is related to two emitting centers: Oxygen Deficient Centers (ODC(II), ~450 nm) and Non-Bridging Oxygen Hole Centers (NBOHC, ~650 nm). The impact of using these fibers as transport fibers for scintillating Cerium-doped OF will also be discussed at the symposium in the context of fiber dosimeter optimization.

PACS Keywords: radiation-induced luminescence, optical fibers, numerical aperture, pre-irradiation, dosimetry.

1 INTRODUCTION

Silica (SiO_2)-based Optical Fibers (OFs) are increasingly employed in harsh environments such as space [1], nuclear power plants [2] or particle accelerators [3] due to their reliability and adaptability to diverse environmental requirements. They are deployed in various applications, including dosimetry and telecommunications. Under radiation exposure, the radiation response of SiO_2-based OFs mainly depends on their doping profile, core composition, and manufacturing processes [4]. Two major radiation effects have to be considered: Radiation-Induced Attenuation (RIA), resulting from the optical absorption (OA) bands of radiation induced point defects and Radiation-Induced Luminescence (RIL), which results from the recombination of electron-hole pairs at recombination centers due to the addition of pre-existing emitting centers in the core of the OFs or from the excitation of radiation-induced defects. While the RIL signal from the sensitive probe is valuable for real-time dosimetry at a given location [5], the stem effect —i.e., the luminescence generated into the transport fiber—can compromise the dose rate (DR) measurement based on the RIL signal of interest [6]. Investigating the interaction between these effects is crucial to develop robust OFs-based sensors. Key factors such as the transport fiber's previous exposure to ionizing radiation (pre-irradiation) and its numerical aperture are investigated during this study to better understand their influence on light collection efficiency and the RIL signal stability.

2 MATERIALS AND METHOD

To investigate the RIL signal generated by Pure Silica Core (PSC) transport fibers, we tested three commercial low-OH OFs with different Numerical Apertures (NA): 0.12, 0.15 and 0.22. All fibers feature the same geometry, with a 105 µm PSC and a 125 µm cladding. The variation in NA is assumed to result from their F-doping levels in the cladding, which can be tuned to change the core-cladding refractive index difference while keeping the core composition identical [7]. Each OF sample was pre-irradiated at: 250 kGy, 1 MGy and 2 MGy. To collect simultaneously the RIL spectrum of these fibers and the RIL intensity, 5 cm-long sections of these pre-irradiated PSC fibers were fusion-spliced at both ends to pristine transport fibers taken from the same three original spools. One end of each sample was connected to a spectrometer while the other side was connected to a Photomultiplier Tube (PMT). The RIL signal generated by the samples was investigated under 40 keV mean energy fluence X-rays. The dose rates studied ranged from 40 mGy(SiO_2)/s to 1.1 Gy/s. To limit the contribution of the transport fibers, they were shielded from X-rays. In a second part of the study, we investigated the RIL signal generated by three samples of 2 cm-long Cerium-doped OFs under the same previous conditions using the three PSC fibers with different NAs as transport fibers. This allows us to assess the influence of the transport fiber NA on the RIL detection within the acquisition chain.

3 RESULTS AND DISCUSSIONS

All the tested PSC fibers present RIL, the RIL intensity is higher for higher NA as expected by a more efficient guidance of the generated photons. Figure 1 compares the RIL dose rate dependence for the 3 fibers pre-irradiated at 1 MGy, showing a linearity that could also be exploited for dosimetry. The response of pristine fibers is not linear. Figure 2 shows the RIL spectra measured from four samples with a NA of 0.22, pre-irradiated at 3 different doses, plus the non-irradiated (pristine) sample for a dose rate of 1.1 Gy(SiO_2)/s. Two main emission bands are identified, ~450

nm and ~650 nm, corresponding to the luminescence bands of Oxygen Deficient Centers (ODC(II)) and Non-Bridging Oxygen Hole Centers (NBOHC) [4].

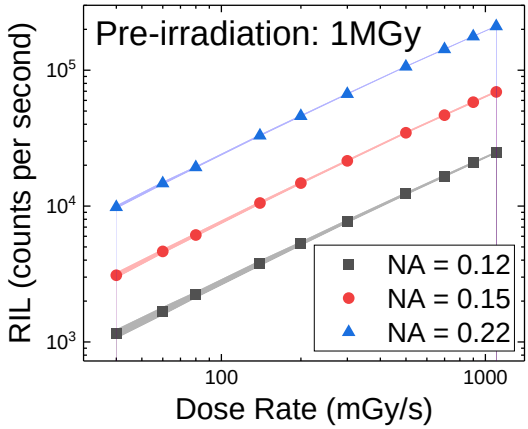

Figure 1: RIL dose rate dependence of the 3 PSC OF pre-irradiated at 1 MGy(SiO_2).

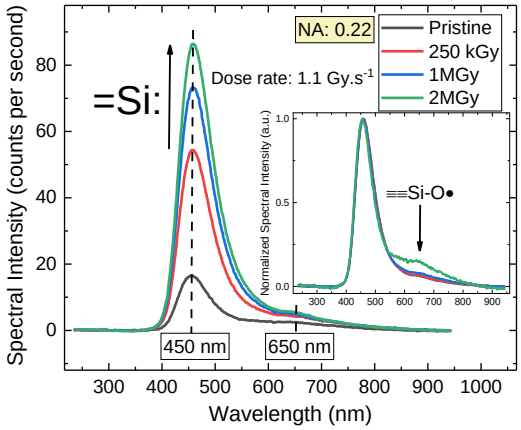

Figure 2: RIL of four 5 cm-long PSC OFs (NA = 0.22) with different pre-irradiation conditions under 40 keV X-rays at 1.1 Gy/s. Inset: Comparison of normalized RIL spectra.

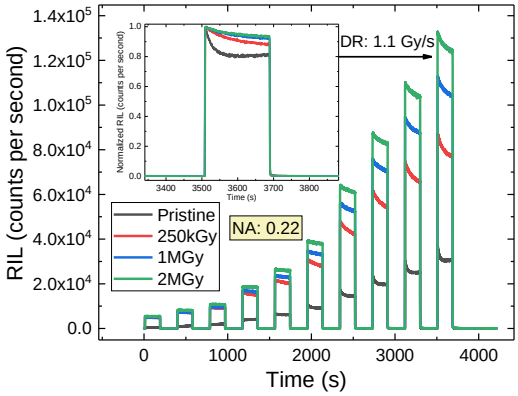

Figure 3: PMT response of RIL intensity at different dose rates for NA = 0.22 pure silica core OF with varying pre-irradiation doses. Inset: Normalized PMT response at the highest studied dose rate.

A clear increase in RIL intensity is observed with increasing pre-irradiation dose, particularly evident at 450 nm. This suggests two possible mechanisms. Either additional ODC(II) defects are created during X-ray pre-irradiation, in addition to those already present from manufacturing, or alternative deep traps competing with ODC(II) for charge trapping are filled by the pre-irradiation leading to a higher RIL efficiency. The second hypothesis sounds more realistic, as usually ODC(II) are not easily generated under irradiation. In addition, at the highest pre-irradiation dose (2 MGy), a noticeable enhancement of the RIL at 650 nm is observed, indicating that the NBOHC defects accumulate and will contribute more at high doses. A similar effect is observed for fibers with lower NA (0.12 and 0.15) with a lower RIL intensity (results to be reported at the symposium). Figure 3 shows that the RIL intensity increases with pre-irradiation and DRs. Moreover, analysis of the normalized RIL intensity at the highest dose rate shows that pre-irradiation improves the quality of the dose rate measurement. It reduces the slight RIL decrease observed during constant dose rate irradiation, possibly by minimizing a contribution from RIA. To further explore the impact of the NA on the collected RIL signal, the results of an additional study using a 2 cm-long Ce-doped OF sample and the PSC OFs as transport fibers will be presented. This will allow us to quantify how the PSC OFs could contribute to the stem effect and determine the best architectures of fiber dosimeters to reduce the stem impact.

REFERENCES

[1] M. Roche *et al.*, 'Solar Particle Event Detection With the LUMINA Optical Fiber Dosimeter Aboard the International Space Station', *IEEE Trans. Nucl. Sci.*, vol. 71, no. 8, pp. 1580–1588, Aug. 2024, doi: 10.1109/TNS.2024.3368137.

[2] P. Ferdinand, S. Magne, and G. Laffont, 'Optical fiber sensors to improve the safety of nuclear power plants', presented at the Asia Pacific Optical Sensors Conference 2013, M. Yang, D. Wang, and Y.-J. Rao, Eds., Wuhan, China, Oct. 2013, p. 89242G. doi: 10.1117/12.2033922.

[3] D. D. Francesca *et al.*, 'Qualification and Calibration of Single-Mode Phosphosilicate Optical Fiber for Dosimetry at CERN', *J. Lightwave Technol.*, vol. 37, no. 18, pp. 4643–4649, Sep. 2019, doi: 10.1109/JLT.2019.2915510.

[4] S. Girard *et al.*, 'Overview of radiation induced point defects in silica-based optical fibers', *Reviews in Physics*, vol. 4, p. 100032, Nov. 2019, doi: 10.1016/j.revip.2019.100032.

[5] S. Girard *et al.*, 'Radiation Effects on Silica-Based Optical Fibers: Recent Advances and Future Challenges', *IEEE Trans. Nucl. Sci.*, vol. 60, no. 3, pp. 2015–2036, Jun. 2013, doi: 10.1109/TNS.2012.2235464.

[6] S. O'Keeffe *et al.*, 'A review of recent advances in optical fibre sensors for in vivo dosimetry during radiotherapy', *Br J Radiol*, vol. 88, no. 1050, p. 20140702, Jun. 2015, doi: 10.1259/bjr.20140702.

[7] E. M. Dianov *et al.*, 'Fluorine-doped silica optical fibres fabricated using plasma-chemical technologies', presented at the Optical Fibre Sensing and Systems in Nuclear Environments, R. Van Geen, F. Berghmans, and M. C. Decreton, Eds., Mol, Belgium, Dec. 1994, pp. 53–57. doi: 10.1117/12.198641.

Combined theoretical and experimental evaluation of the energy dependence of the radioluminescence phenomenon in Ce-doped optical fibers

L. Weninger[*], A. Meyer[*], A. Morana[*], D. Lambert[**], Y. Ouerdane[*], A. Boukenter[*], E. Marin[*] and S. Girard[*†]

[*] Université Jean Monnet Saint-Etienne, Laboratoire Hubert Curien UMR 5516, F-42023, Saint-Etienne
[**] CEA, DAM, DIF, F91297 Arpajon, France
[†] Institut Universitaire de France (IUF) 75005 Paris, France.

ABSTRACT

We combined in this study two fiber optic dosimetry techniques based on the Radiation-Induced Attenuation (RIA) and Radiation-Induced Luminescence (RIL) phenomena to investigate the X-ray energy dependence of the RIL via Monte-Carlo Geant4 simulation tools.

PACS Keywords: dosimetry, optical fibers, silica, X-rays

1 INTRODUCTION

Over the years, simulation tools, mainly based on Monte-Carlo codes have been developed with the aim of understanding the effect ionizing radiation has on matter and, consequently, on devices and materials. [1] Among others, these tools can be used to understand the influence of shielding or packaging materials on the sensibility of dosimeters. Optical fibers are very promising for dosimetry thanks to their low-complexity and large range of dose or dose rate monitoring capability. [2] The two main macroscopic phenomena that have been investigated over the years for dosimetry purposes, Radiation-Induced Attenuation (RIA) and Radiation-Induced Luminescence (RIL) have already proven to be very reliable under a number of conditions [3,4]. The RIA characteristic of P-doped fibers depends only on the Total Ionizing Dose (TID) and not on the type of incident radiation nor its energy. [2] On the other hand, this has yet to be confirmed for the fibers used for dose rate measurement based on RIL. To study the RIL dependence on the X-ray energy, we combine RIA and RIL-based dosimeters to measure TID induced by X-rays with different spectral distributions, and compare it with the TID estimated via Monte-Carlo simulations with Geant4.

2 MATERIALS AND METHODS

2.1 Dosimetry setup

The setup is composed of a monochromatic RIA setup, using a 20-meters long P-doped (10 wt%) single-mode optical fiber, and a double RIL setup, using two samples of the same Ce-doped (0.16 wt%) multi-mode fiber (2-cm and 50-cm long). The dimensions of the fibers, also used for the Geant4 simulations, are reported in Table I. The monochromatic RIA configuration is composed of a source at 1535 nm and two photodiodes. One to monitor the source and the other for measuring the signal transmitted through the fiber under test. The ratio of these two intensities gives the real-time measurement of the total attenuation of the fiber. Knowing the initial losses and the length of the radiation sensitive fiber, we can have a real-time RIA measurement. Finally, as P-doped fibers have been calibrated across multiple radiation types and energies, we can use their sensitivity factor at 1535 nm of 4 dB km^{-1} Gy^{-1} to estimate the TID in real-time. On the other hand, the dual RIL setup simply entails two photomultiplier tubes to measure the RIL signal from the Ce-doped samples.

Sample	Core Ø	Cladding Ø	Coating Ø
P 20 m	10 µm	125 µm	250 µm
Ce 2 cm	102 µm	No	No
Ce 50 cm	102 µm	125 µm	242 µm

Table 1: Dimensions of the tested fibers.

2.2 Experimental Setup

To test their capability to measure the real-time dose rate given by X-rays, the three fibers were placed close together inside the LabHX facility at Lab. Hubert Curien (Saint Etienne, France) under different irradiation conditions. To obtain these, each measurement was composed of 14 irradiation sequences (20s long, with 40s in-between). Each step used a different tube voltage between 10 and 220 kV, to modify the emitted X-ray spectrum. This procedure was then repeated at different tube currents (0.2, 2, 20 mA), to study the dynamic range of the dosimeters, and adding Al shields with different thicknesses (1-5 mm) to further modify the energy spectrum by cutting their low-energy part.

2.3 Geant4 simulations

The geometry of the experiment was simulated with Monte-Carlo-based tools. SpekPy was first used to generate the X-ray spectra corresponding to the experimental conditions listed in the previous section. Geant4 was then used to estimate the dose/fluence characteristic of the three optical fibers, following the procedure used in [1]. Each of the samples were modeled as concentric cylinders with the diameters reported in Table I. The composition of each fiber

was also adapted to emulate the real samples. The convolution of the data obtained with the two tools is an estimate of the dose rate (in Gy(SiO_2)/s) seen by the three fibers across all the conditions.

3 RESULTS AND DISCUSSION

The X-ray spectra simulated via SpekPy with three tube voltages and either with or without 5 mm Al filter are shown in Fig. 1. These curves show how the spectra are impacted by the two parameters. While the tube voltages increase the maximum X-ray energy, without affecting the shape at lower one, the use of an Al filter mostly impacts the lower energy part of the spectrum. The latter effectively cuts the influence of the lower energy characteristic X-rays, main contributor to the deposited dose in such a thin volume. [1] The inset shows the geometry of the two fibers (Ce 50 cm and P 20 m) as simulated within Geant4.

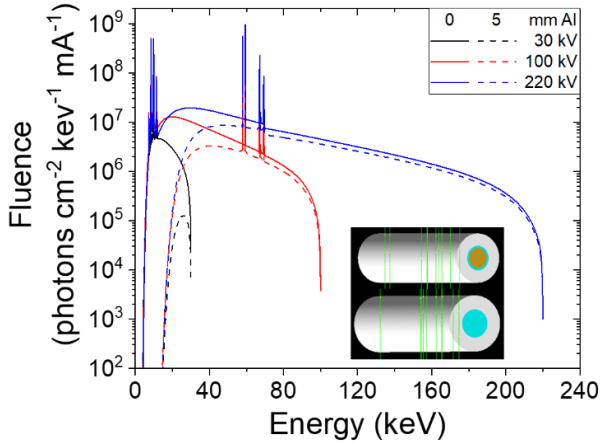

Fig. 1: Examples of X-ray spectra simulated with SpekPy at different voltages, with (line) and without (dash) a 5 mm Al filter. The inset shows the 3D models of the two fibers used for the Geant4 simulations. Above is the Ce fiber and below is the P-doped fiber.

On the measurement side, Fig. 2 reports the dose rate evaluation from both the RIL and the RIA (derivative) measurements for one irradiation case (20 mA, no Al). The latter is directly reported as a real-time dose rate measurement. All three fibers are clearly capable of measuring the investigated dose rates. This figure also proves the interest in using both dosimetry methods: on one side, we can appreciate the higher dynamic and faster response of the RIL system, while on the other lays the capability of performing calibrated dose measurements of the RIA-based sensor when sufficient doses are achieved. Estimating the RIL intensity at each dose rate, across all measurements (0-5 mm Al filtering, 0.2 to 20 mA tube current), and plotting it against the simulated dose rate for the RIL 50 cm sample gives the master curve given in Fig. 3. Across all the experiments, the relation between RIL and dose rate is clearly linear, suggesting an independence of the RIL signal from the X-ray energy.

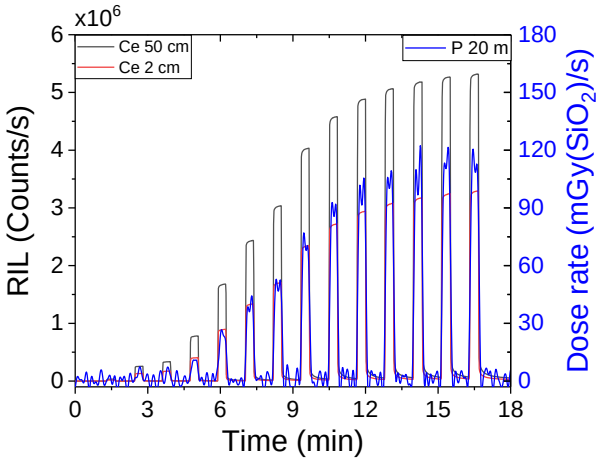

Fig. 2: Kinetics of the RIL of the two Ce-doped fibers and of the dose rate measured with the P 20m sample for the measurement at 20 mA and without aluminum filtering.

The deviations from this relation are the largest when no Al filtering was applied (~30%), which indicates a possible overestimation of the low-energy X-rays in our simulations.

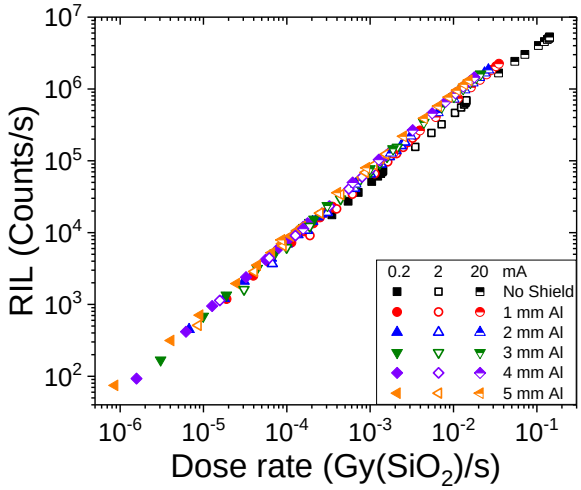

Fig. 3: RIL signal vs simulated dose rate across all irradiation conditions.

4 CONCLUSION

This abstract shows the promise of the proposed method, combining the proven capabilities of the two fiber-based dosimetry techniques and the simplicity of simulating SiO_2 cylinders to confirm that the RIL of fibers is energy independent. For the final paper, different models and physics engines will be investigated on the simulation side to further improve the compatibility with the measurements for the presentation and the final article.

REFERENCES

[1] A. Meyer *et al.*, Radiation 3 (2023).
[2] S. Girard *et al.*, IEEE TNS 72 (2025).
[3] L. Weninger *et al.*, RIO 19 (2025).
[4] D. Di Francesca *et al.*, IEEE TNS 65 (2018).

Wednesday, June 25th

Session #6

Advanced technologies and techniques

Philippe Paillet, CEA

3D Printing of Silica-based Binary and Ternary Oxide Systems using Two-photon Polymerization

Halima El Aadad*, Hicham El Hamzaoui*, Yves Quiquempois* and Marc Douay*

* Univ. Lille, CNRS, UMR 8523 - Physique des Lasers Atomes et Molécules (PhLAM), F-59000 Lille, France.

ABSTRACT

We report on a successful preparation of new hybrid photoresists based on a binary SiO_2-CaO or a ternary SiO_2-CaO-P_2O_5 sol, suitable for 3D printing via two-photon polymerization (2PP). Complex microstructures were 3D printed and sintered up to 700 °C. After sintering at 500 °C, the Fourier transform infrared spectroscopy (FTIR) spectra showed the disappearance of the characteristic bands associated with the organic phase, and the presence of bands characteristic of the binary and the ternary oxide systems. The scanning electron microscopy (SEM) images showed different morphologies of agglomerated nanoparticles for ternary and binary systems.

PACS Keywords: additive manufacturing, two-photon polymerization, silica-based hybrid photoresists, sol–gel process, binary and ternary oxides.

1 INTRODUCTION

Additive manufacturing (AM) technologies are introducing new opportunities for the fabrication of advanced materials. One of the most promising methods is two-photon polymerization (2PP) 3D printing. Indeed, it offers several advantages, such as the ability to produce objects with high resolution with flexible and complex geometries [1,2]. Silica glass is among the most studied systems, thanks to its unique physico-chemical properties such as high chemical purity, thermal resistance, excellent optical transmission, and chemical durability [3]. The 2PP 3D printed silica glasses are suitable for different applications such as micro-sensing [1] and optoelectronics [4]. However, various network-forming oxides or modifiers, such as P_2O_5 or CaO, can be incorporated inside the silica matrix to modify its properties [5]. These compositions offer opportunities for applications in various fields such as biomedicine [6]. However, it is difficult to form complex structure with bioglasses due to their stuffiness and brittleness [7]. Moreover, a spatial resolution down to submicrometer scale is still necessary to enhance the precision of scaffold manufacturing [8]. In the present study, we aim to demonstrate as proof of concept the possibility of 2PP 3D printing of scaffolds with submicron features, using two renowned oxide systems, namely SiO_2-CaO and SiO_2-CaO-P_2O_5.

2 EXPERIMENTAL

We have developed new silica hybrid photoresists based on a combination of an organic acrylate resin and an inorganic sol of a binary SiO_2-CaO or a ternary SiO_2-CaO-P_2O_5 system. The 3D printing of the microstructures was performed on fused silica substrates, using the Photonic Professional GT+ printer from Nanoscribe.
Once the 3D printing was complete, a development step was required to remove the unpolymerized photoresist. This consisted of immersing the substrate in propylene glycol monomethyl ether acetate for 10 min followed by isopropanol for 5 min. Finally, the printed microstructures were heat treated under air at 700 °C.

3 RESULTS

Figure 1 shows examples of 3D printed microstructures using both binary (a) and ternary (b) hybrid photoresists, before and after heat treatment at 700 °C. The choice of sintering temperature was based on the results of the TGA analysis. After sintering, we observed that all the microstructures retained their shapes (Figure 1) with slight deformation. Furthermore, we stress that binary microstructures showed higher thermal resistance to sintering at 700 °C compared with those of the ternary system. This result could be related to the presence of phosphorus in the composition of the ternary system. Furthermore, 3D objects with submicrometer features were produced, as shown in Figure 1. The resolutions reached for the binary and ternary systems were 350 nm and 235 nm, respectively. Moreover, a scaffold pore size of about 355 nm was also obtained, which has never been achieved using other 3D-printing techniques, to the best of our knowledge. These results show that our approach can be used to develop adapted 3D scaffold structures for biomedical applications where scaffolds with small pore sizes are needed [9].

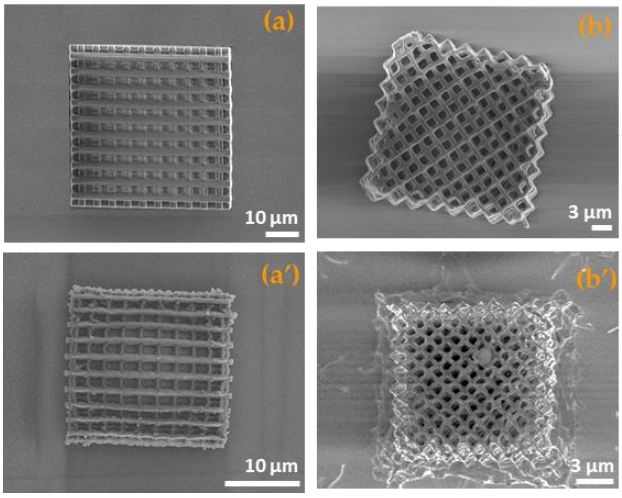

Figure 1. 3D-printed microstructures of binary (a) and ternary (b) systems before (a–b) and after heat treatment at 700 °C (a′–b′), respectively.

SEM analysis revealed different morphologies depending on the composition of the material. In the case of the ternary system, it showed that it was made of an agglomeration of finer particles with an average particle size of about 20 nm. However, regarding the binary system, it is formed of agglomerated particles with irregular shapes and a rough texture with an average particle size of about 60 nm.

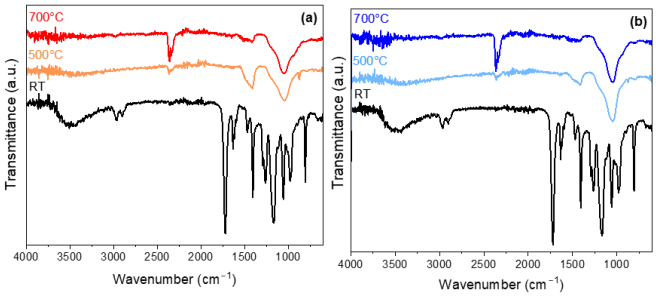

Figure 2. FTIR spectra of UV-treated hybrid photoresists before and after heat treatment at 500 and 700 °C for 1 h: (a) SiO_2-CaO and (b) SiO_2-CaO-P_2O_5.

The FTIR spectra of the hybrid photoresists before and after heat treatment at 500 and 700 °C are shown in Figure 2. Absorption bands associated with the organic phase in the UV-treated hybrid photoresists were observed. After heat treatment at 500 °C, we observed the disappearance of these bands, and the FTIR spectra showed those characteristics of the SiO_2-CaO binary or SiO_2-CaO-P_2O_5 ternary systems (Figure 2a and b).

4 CONCLUSION

New hybrid photoresists suitable for 2PP additive manufacturing of multicomponent oxide systems were successfully synthesized via a combination of organic resin and sol–gel sols.

It was found that the 3D-printed microstructures endure a sintering temperature up to 700 °C leading to 3D scaffolds with submicrometer features and a resolution of about 235 nm with pore size of about 355 nm. After sintering at 700 °C, it was shown that the obtained binary (SiO_2-CaO) and ternary (SiO_2-CaO-P_2O_5) oxide systems, incorporating carbonate groups, present different morphology. Our results open the way towards precise control of bioglass scaffold fabrication with tremendous design flexibility. With their lower temperature sintering, these oxides systems present a potential for the development of localized metallization interesting for other fields such as microelectronics and plasmonics.

ACKNOWLEDGEMENTS

This work was supported in part by the Agence Nationale de la Recherche through the Add4P Equipex+ project (ANR-21-ESRE-0007) and 3DGlassens project (ANR-21-CE08-0035-01). The present work was also carried out within the framework of the Contrat de Plan Etat-Region (CPER) WaveTech@HdF, which is supported by the Ministry of Higher Education and Research, the Hauts-de-France (HdF) Regional council, the Lille European Metropolis (MEL), the Institute of Physics of the French National Centre for Scientific Research (CNRS), and the European Regional Development Fund (ERDF).

This work has been also supported by IRCICA institute and FiberTech Lille platform of University of Lille (https://fibertech.univ-lille.fr/en/).

REFERENCES

[1] H. El Aadad *et al.*, Mater. Today Adv., 22, 100500, 2024.

[2] G. Seniutinas *et al.*, Microelectron. Eng., 191, 25-31, 2018.

[3] C. Xin *et al.*, Mater. Des., 227, 111736, 2023.

[4] J. Bauer *et al.*, Science, 380, 960-966, 2023.

[5] L. He *et al.*, Bioeng., 10, 672, 2023.

[6] M. Cannio *et al.*, Materials, 14, 5440, 2021.

[7] A.R. Boccaccini and J.J. Blaker, Expert Rev. Med. Devices, 2, 303-317, 2005.

[8] L. He *et al.*, Bioengineering, 10, 672, 2023.

[9] B.A.E. Ben-Arfa and R.C. Pullar, Processes, 8, 615, 2020.

Bias-Dependent TID Effects and Annealing Recovery in Power COTS GaN HEMTs

Hadrien Couillaud[1], Marc Gaillardin[1] and Laurent Artola[2]

[1]CEA, DAM, CEA Gramat,
F-46500 Gramat, France
[2]DPHY, ONERA, Université de Toulouse,
31000, Toulouse, France

ABSTRACT

This work investigates the response of the commercial normally-off GaN HEMT transistor GS66508B to total ionizing dose (TID) effects under various bias conditions. The study focuses on the physical mechanisms responsible for the observed degradations. It then examines the recovery of key static parameters, namely V_{TH} and g_m using two different annealing methods.

PACS Keywords: GaN HEMT, power devices, COTS, TID effects, annealing, interface traps.

1 INTRODUCTION

Wide bandgap (WBG) transistors, especially Gallium Nitride High Electron Mobility Transistors (GaN HEMTs), have gained interest for their high performances, high thermal tolerance, breakdown voltage, and power density. The Two-Dimensional Electron Gas (2DEG) formed at the AlGaN/GaN interface enables high mobility and GHz-range operation. With the growing availability of commercial off-the-shelf (COTS) devices, GaN HEMTs are increasingly adopted, particularly in space applications, due to their superior Total Ionizing Dose (TID) resistance compared to silicon-based devices [1].

While GaN HEMTs show good TID tolerance, the mechanisms behind thermal annealing and radiation hardening in commercial devices are not fully understood [2]. This study compares the TID response of a COTS power GaN HEMT under various biases and examines parameter recovery using two annealing methods.

2 DEVICE AND EXPERIMENTAL SETUP

The GS66508B p-GaN from GaN Systems features V_{TH} = + 1.7 V, V_{GS} from – 10 V to + 7 V, V_{DS} = + 650 V, R_{DSON}(max) = 50 mΩ, and I_{DS}(max) = 30 A. It is an enhancement-mode transistor, ideal for power applications with high switching frequency, breakdown voltage, and current handling allowed by GaN and 2DEG properties.

This transistor, suited for high-frequency power applications, is tested under various bias conditions (Table 1) during irradiation and annealing, as shown in Fig. 1. Biases during annealing matched those used during irradiation. Static parameters were characterized using the B1500A device and B2201A switching matrix.

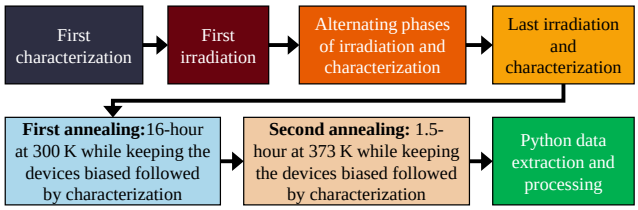

Fig. 1. Experimental procedure steps.

Bias	1	2	3	4
V_{GS} (V)	+7	-7	-7	0
V_{DS} (V)	0	0	+300	0

Table 1. Summary of irradiation bias conditions.

X-ray irradiations are conducted using the ORIATRON facility, a linear accelerator (LINAC) based at CEA Gramat, France [3]. It generates an x-ray spectrum with an average energy near 1 MeV, similar to the photon energy from ^{60}Co sources utilized to investigate TID-induced effects. The device under test (DUT) was exposed to a constant dose rate of 1.4krad(SiO_2)/min. All devices undergo irradiation at room temperature in ambient air. Annealing experiments are performed using a climatic chamber either at room temperature or at 373K.

3 STATIC PARAMETER DEGRADATION UNDER TID STRESS

In this study, the TID sensitivity of the studied GaN HEMT is assessed by tracking variations in the threshold voltage (V_{TH}) and the transconductance (g_m) which are critical electrical parameters frequently used in the evaluation of both SiC CMOS [4] and GaN HEMTs technologies [5]. ΔV_{TH} is selected as the primary indicator due to its direct influence on I_{OFF} and I_{ON} [6], making it suitable for identifying worst-case degradation scenarios. Its extraction is based on the standard linear extrapolation method [7].The g_m,max parameter is the maximum of the derived $I_D(V_G)$ curves.

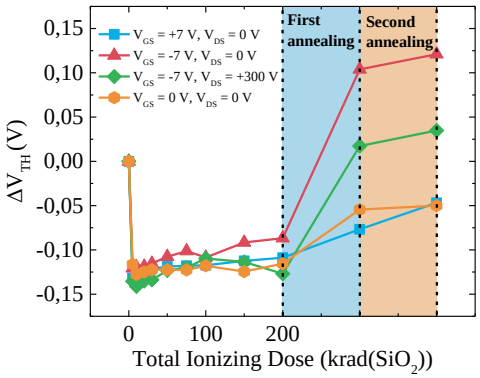

Fig. 2. ΔV_{TH} extracted as a function of TID for all bias conditions.

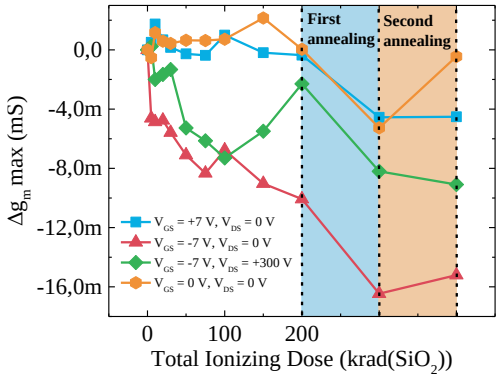

Fig. 3. Δg_m,max extracted as a function of TID for all bias conditions

Fig. 2 illustrates the ΔV_{TH} shift as a function of the TID under all bias conditions. For all bias, an significant negative shift of approximately -125 mV is reached at a low dose of 50 krad(SiO_2). For TID between 50 krad(SiO_2) and 200 krad(SiO_2), the V_{TH} shift appears to remain constant across all bias conditions. The initial negative ΔV_{TH} shift is attributed to positive charge trapping within the AlGaN barrier, which enhances the electric field toward the channel and increases carrier density in the 2DEG [8].This effect is primarily driven by ionization-induced dehydrogenation of pre-existing donor-like complexes, such as O_N-H which are associated with a high density of crystalline defects resulting from the lattice mismatch at the AlGaN/Si interface. At low doses, rapid activation of these traps dominates the threshold voltage shift, while the saturation observed at higher doses may be due to a limited density of available trap states in the material [9].

Upon examining the results after the first annealing phase, a clear V_{TH} recovery is observed for all bias conditions. However, the negative gated-bias cases 2 (V_{GS} = -7 V, V_{DS} = 0 V) and 3 (V_{GS} = -7 V, V_{DS} = +300 V) appear to recover more effectively than the others. Indeed, after the first annealing phase at 300K, the V_{TH} increases by +0.2 V for bias 2 and +0.15 V for bias 3. This recovery indicates that the radiation-induced charges are metastable in nature, likely associated with shallow or weakly trapping defect states [8].

Fig. 3 shows a slight Δg_m,max degradation under all bias conditions, consistent with limited interface trap generation from ^{60}Co exposure [5]. The initial annealing phase leads to limited g_m recovery suggesting only partial restoration of carrier mobility in the 2DEG. A more notable improvement follows the second annealing at 373 K. Similar behavior are observed for the on-state resistance ($R_{DS,ON}$) (not shown here). These recovery results through annealing are unexpected compared to what is typically observed in the literature [10]. They will be investigated thoroughly in the final paper through dedicated annealing experiments to probe the mechanisms responsible for such behaviors.

4 CONCLUSION

Irradiation results show negative shift of V_{TH} and g_m,max degradation across all bias conditions. The two annealing methods impact device recovery differently: the first better mitigates V_{TH} shifts, while the second more effectively restores 2DEG mobility.

The final paper will include a complementary study of both static and dynamic shifts induced by TID effects in two normally off enhancement mode COTS GaN HEMTs GS66508B and IGLD60R190D1. Various annealing methods will be investigated, comparing the influence of duration, temperature, and applied bias on device electrical parameter recovery, with the aim of understanding the underlying physical mechanisms.

5 AKNOWLEDGEMNT

We thank the French Ministry of the Armed Forces and the Defense Innovation Agency (AID) for funding this research.

6 REFERENCES

[1] M. Zerarka *et al*, "Cosmic ray immunity of COTS Normally-Off Power GaN FETs for space, aeronautic and automotive applications", 2020, *RADECS*.
[2] S. J. Pearton, *et al*, "Ionizing Radiation Damage Effects on GaN Devices", 2015, *Journal of Solid-State Science and Technology*.
[3] D. Lambert *et al*, "TID Effects Induced by ARACOR, ^{60}Co, and ORIATRON Photon Sources in MOS Devices: Impact of Geometry and Materials", 2021, *IEEE TNS*.
[4] K. Ben Ali *et al*, "Single event effects and total ionizing dose in 600V Si-on-SiC LDMOS transistors for rad-hard space applications", 2017, *ESSDERC*.
[5] A. C. V. Bôas *et al*, "Ionizing Radiation Hardness Characterization of GaN HEMTs Depends on the Radiation Source", 2022, *RADECS*.
[6] J. R. Schwank *et al*, "Radiation Effects in MOS Oxides", 2008, *IEEE TNS*.
[7] L. Dobrescu *et al*, "Threshold voltage extraction methods for MOS transistors", doi: 10.1109/SMICND.2000.890257.
[8] D. M. Fleetwood *et al*, "Radiation Effects in AlGaN/GaN HEMTs", 2022, *IEEE TNS*.
[9] X. Sun *et al*, "Total-Ionizing-Dose Radiation Effects in AlGaN/GaN HEMTs and MOS-HEMTs", 2013, IEEE *TNS*.
[10] H. Wu *et al*, "Total Ionizing Dose and Annealing Effects on Shift for p-GaN Gate AlGaN/GaN HEMTs", 2022, *IEEE EDL*.

Electric charges as an apparent governing parameter for electron induced stress relaxation in amorphous silica micropillars

M Rusinowicz[*], G. Kermouche[*], S. Sao-Joao[*], M. Bourguignon[**], E. Barthel[**], Y. Kato[***], G. Rosales[***], F. Volpi[****]

[*]Mines Saint-Etienne, CNRS, UMR 5307 LGF, Centre SMS, F-42023, Saint-Etienne, France
[**]Soft Matter Sciences and Engineering, ESPCI Paris, PSL University, Sorbonne Université, CNRS, Paris 75005, France
[***]Nippon Electric Glass, 7-1, Seiran 2-Chome, Otsu, 520-8639, Shiga, Japan
[****]University Grenoble Alpes, CNRS, Grenoble INP, SIMaP, 38000 Grenoble, France

ABSTRACT

We report a new approach on the phenomenon of plastic flow induced by electron irradiation in amorphous silica, revealing that the total injected electric charge is the governing parameter of the mechanical response: micropillar relaxation tests conducted under electron irradiation showed a one-to-one relationship between the injected electric charge and the measured mechanical stress level, regardless of the applied current [1]. Moreover, by performing these tests at high temperature, we have found that the effects of electronic processes and temperature are decoupled. This result suggests that under the present irradiation/temperature conditions, the density of flow defects is controlled only by irradiation, while the plastic rearrangement of the defects depends only on temperature.

PACS Keywords: Amorphous silica; Electron beam irradiation; Electric charge; Micropillar relaxation; High-temperature micromechanical tests.

1 INTRODUCTION

In the past few years a particularly intriguing phenomenon was evidenced: amorphous silica, the archetype of a brittle material at the macroscale, becomes extremely ductile when mechanically tested at the nanoscale under electron beam (e-beam) irradiation in transmission and scanning electron microscope. According to molecular dynamics and Monte Carlo calculations, the atomistic viscoplasticity mechanisms involved are described as bond-switching events related to Si–O bonds, favoring the mobility of atomic clusters and ultimately plastic flow. Such events would be strongly enhanced below the glass transition temperature under the effect of the incident electrons. This mechanism is listed as a radiolysis effect in electron microscopy-induced damage, i.e., In this study, we propose to unravel the electrical quantity governing the mechanical response of amorphous silica under e-beam irradiation and to interpret its role in terms of defect formation/motion. For that purpose, a new micropillar relaxation tests was designed and conducted both at room temperature and at high temperature (up to 600°C).

2 MATERIALS AND METHODS

Relaxation tests are carried out using a displacement-controlled Alemnis ASA nanoindenter with a 10~µm diameter flat punch. It is equipped with a high-temperature module and installed in a Zeiss Gemini Supra 55VP SEM. Amorphous silica pillars (diameter ~ 5 µm, height ~ 5 µm) are lithographed from commercial samples supplied by Nippon Electric Glass Co., Ltd. Their geometry were therefore highly reproducible. The mechanical loading consists in a compression segment followed by a relaxation segment during which the displacement of 1.5 µm is held for 300 s. Electron irradiation is performed with an acceleration voltage of 20 kV, ensuring good penetration of the electrons in the pillar. The fastest possible scan speed of 0.15 µs/pixel is used to achieve an effectively constant irradiation of the pillar. The injected current is calibrated from the SEM magnification. The dose in terms of electric charge injected is then computed from the electric current and the duration of the mechanical loading. During the relaxation segment, the mechanical stress σ is computed as the ratio “force over pillars diameter”.

3 RESULTS

The true stress vs. time curves for the relaxation tests performed at room temperature are plotted in Figure 1. The increases in stress over time up to 15~s are associated with the mechanical loading segment at 100~nm/s up to a maximum displacement of 1500~nm. Then, the decreases in stress from 15~s to 315~s correspond to the fixed-displacement relaxation segment. A reference test is performed with the beam off, showing that the stress level decreases little from approximately 6.5 to 6.0~GPa over 5~min of relaxation. the significant effect of electron irradiation is clearly evidenced by the stress drops that are more pronounced as the current increases, down to 0.5~GPa

in 5~min under 1876~pA. The electrons injected into the pillar therefore have a huge impact on the relaxation kinetics.

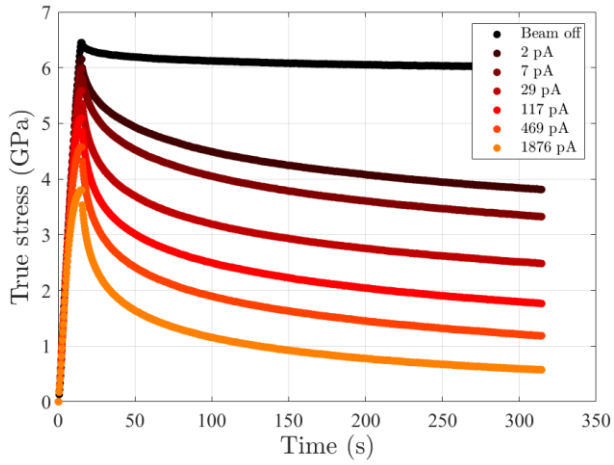

Figure 1: True stress vs. time curves at a fixed displacement of 1.5~µm with different current intensities injected into the pillars at room temperature.

The question arising from these results is whether there exists an electrical quantity that governs the entire mechanical response of amorphous silica. Since both current and time appear to play major roles in the observed phenomenon, we have tried to use the simplest physical quantity that combines both parameters: the dose Q in terms of electric charge injected into the pillar from the beginning of the relaxation segment, i.e. the integral of the current with respect to time during the relaxation. The mechanical stress is then plotted as a function of this dose Q for all the relaxation tests conducted both at RT and up to 600 °C in this study. Remarkably, all curves overlap over six decades, revealing a single master curve where the stress level σ is in one-to-one correspondence with the dose Q after normalization by the relaxation stress without irradiation (Figure 2).

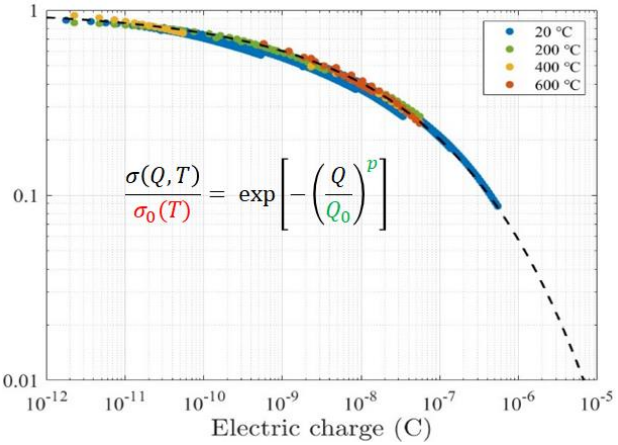

Figure 2: Normalized true stress as a function of the dose Q of electric charge injected into the pillars during the relaxation segment for different irradiation conditions at 20, 200, 400 and 600°C.

4 DISCUSSION AND CONCLUSION

We show in this work that electron irradiation-induced relaxation in silica glass is governed by the injected electric charge. Electrons injected into the material likely creates metastable transient defects, existing only in the presence of the charges, which contribute to the viscous flow if they are located in the stressed volume. Temperature has an independent role since it facilitates the local structural rearrangements from the defects formed by the electric charges. This explains why the behavior of the glass in this state is closer to that observed above the glass transition temperature, where sufficient defects are already available for viscous flow, and only their motion is thermally activated.

REFERENCES

[1] Rusinowicz, Morgan, et al. "Electric charges as an apparent governing parameter for electron induced stress relaxation in amorphous silica micropillars." Scripta Materialia 261 (2025).

Wednesday, June 25th

Session #7

RadioPhotoluminescence

Antonino Alessi, CEA/Univ. Palermo

The need of new calibrations for high level dosimetry: Radiophotoluminescence FD-7 dosimeters irradiated with 6 MeV electrons

Matteo Ferrari[*] and Aditya Raj Mandal[*], Ygor Aguiar[*‡], Ruben García Alía[‡], Matilde Avesani[*], Marc Gaillardin**, David Poujols**, Sylvain Girard[*†]

[*] Université Jean Monnet Saint-Etienne, Laboratoire Hubert Curien UMR 5516, F-42023, Saint-Etienne
[‡]European Organization for Nuclear Research (CERN), CH-1211 Geneva, Switzerland
** CEA CEA DAM, GRAMAT, F- 46500 Gramat, France

[†]Institut Universitaire de France (IUF) 75005 Paris, France.

ABSTRACT

Radiophotoluminescence (RPL) FD-7 glass dosimeters are commonly used in personal and medical dosimetry. Their application, traditionally limited to few hundreds of Gy, has been recently extended up to kGy and MGy range, and a dedicated readout system specifically targeting high doses serves the irradiation needs of CERN's accelerator complex. This study focuses on the response of both pristine and thermally treated RPL dosimeters to 6 MeV electron irradiation at CEA Gramat, covering doses ranging from 1 Gy to 1 MGy at a very high dose rate of about 780 kGy/h. Readout performed at CERN will be coupled with post-irradiation optical measurements. The results will provide new calibration curves for the use of RPL dosimeters to measure high electron doses. Annealed dosimeters are studied in view of their regeneration for high level applications.

PACS Keywords: high radiation areas, dosimetry, radiophotoluminescence, electron beam

1 INTRODUCTION

Radiophotomuminescence (RPL) dosimeters made of FD-7 glass are commonly used passively in personal and medical dosimetry thanks to their unique features such as small size, non-destructive readout, wide sensitivity range, regeneration through thermal annealing and long stability[1]. Traditional readout systems are designed to measure doses up to some hundreds of Gy. In this dose range, the RPL signal, used for readout, is proportional to the dose. At higher doses, the dosimeters darken due to the formation of color centers (see Figure 1), and the RPL signal is progressively attenuated. Various types of commercial dosimeters taking advantage of optical properties such as PMMA and radiochromic ones other than RPLs are currently studied to verify the possible extension of their dynamic range beyond the producer's indications [2]. Many of these dosimeters use transmittance at a selected wavelength to determine the absorbed dose, this being the case for RPL dosimeters used beyond 300 Gy [3]. In some cases, sensitivity is increased by using a combination of probing wavelengths. For RPL, a two light system exploits both radioluminescence signal and transmittance at a selected wavelength [4].

With growing number of facilities and radiation environments, such as CERN, where doses up to the kGy-MGy range are reached [5], there is an increasing demand of reliable passive and real-time high radiation monitors [6]. RPL dosimeters are emerging as a suitable candidates for high dose monitoring application, not only for passive use but for online readout as well [7], [8]. The readout systems currently in use to characterize the high-level response of RPL FD-7 dosimeters up to MGy of dose relies on gamma calibration curves realized in 60-Co facilities and referring to readout time performed 26 days after irradiation conclusion. These calibration curves have been proven reliable over a large range of doses and dose rates, and for a variety of radiation environments [9]. However, limitations apply, and for example for doses exceeding 0.1 MGy, deviations from these calibrations are observed. These deviations seem to be influenced by dose rate [9], radiation type and energy spectrum, temperature and previous thermal treatments [10] (such as the ones normally used to regenerate the dosimeters), time interval between irradiation and readout. Further irradiations exploring the readout dependence on these parameters, especially at high doses, are needed. This paper aims at providing a new calibration curves for both pristine and thermally treated RPLs up to the MGy level with monoenergetic 6 MeV electrons at a very high dose rate. This work will provide a deeper understanding of the defect generation and kinetic, currently debated in the scientific community, and pivotal for exploitation of dosimetry mechanisms beyond current limits [7], [11], [12].

2 MATERIAL

Commercial cylindrical (1.5 mm diameter, 8.5mm length) FD-7 RPL glass dosimeters produced by Chiyoda Technol (Japan) are studied. Samples comes from a new batch (2025), to be compared with the one used at CERN for high level

dosimetry activities since 2013. Dedicated calibration might be needed for new batches of the same commercial dosimeter. While the product could be stable over different productions for the designed readout, differences might apply for what concerns the parameters that become relevant for dosimetry beyond traditional range of use only. This can be the case of RPL dosimeters, for which the radiation-induced concentration and kinetics of color centers becomes relevant at doses exceeding about 300 Gy only.

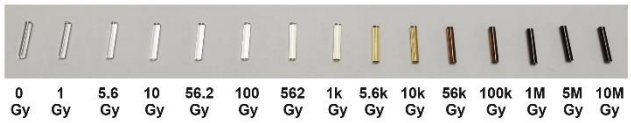

Figure 1: RPL dosimeters: color as a function of the dose [9].

3 METHODOLOGY

RPL dosimeters are thermally treated for 7h at a constant temperature of 400°C, following a cleaning procedure in ultrasonic bath. After heating, samples are cooled down naturally for at least 12 hours [10]. RPL dosimeters are known to be erasable and are reused for standard applications after annealing (normally, 1h at 400°C) [1]. The validity of annealing protocols is currently being adapted and verified for applications at high doses as well[10].

Both pristine and thermally treated RPL dosimeters are irradiated at the at CEA Gramat facility for high flux radiation testing [13]. Based on a compact linac accelerator, the facility targets high deposited doses by means of monoenergetic 6 MeV electron. The irradiation campaign aims at performing a new calibration under electron irradiation covering a wide range of selected doses from 1 Gy to the MGy level, at a constant dose rate of about 780 kGy/h. There is a general scientific interest in exploring accelerator driven irradiation facilities as an alternative to gamma sources [13] for irradiation activities.

Complementary to the experimental activities, Monte Carlo simulations realized with the code PHITS [14] will provide information on the homogeneity of the deposited dose in the RPL volume and on the conversion factors between the reference dosimetry in the facility and the dose actually absorbed by the irradiated samples.

4 MEASUREMENTS

Irradiations are ongoing. Readout will be realized using CERN's system, devoted to high doses, and the results of these new calibrations will be presented and compared with the previous gamma ones. The impact of the pre-irradiation thermal treatment on the readout will be discussed.

5 CONCLUSIONS

The results of this study will provide precious insights on the response of RPL dosimeters at high doses and useful information on the possibility of re-using dosimeters for high-dose applications. In the case of CERN, this can be evaluated in thousands of dosimeters, greatly optimizing the monitoring system.

REFERENCES

[1] T. Yamamoto, *et al.*, 'Current status and future prospect of RPL glass dosimeter', *Radiation Measurements*, vol. 136, p. 106363, Aug. 2020.

[2] P. Casolaro *et al.*, 'Real-time dosimetry with radiochromic films', *Sci Rep*, vol. 9, no. 1, p. 5307, Mar. 2019.

[3] D. Pramberger, Y. Q. Aguiar, J. Trummer, and H. Vincke, 'Characterization of Radio-Photo-Luminescence (RPL) Dosimeters as Radiation Monitors in the CERN Accelerator Complex', *IEEE TNS*, vol. 69, no. 7, pp. 1618–1624, Jul. 2022.

[4] H. Vinke and J. Trummer, 'Apparatus and Method for Determining a Dose of Ionizing Radiation', International Publication Number WO 2014/161732 A1, Oct. 2014

[5] M. Macha, *et al.*, 'Effects of Radiation Dose on Lubricants: A Review of Experimental Studies'.

[6] B. Camanzi and A. G. Holmes-Siedle, 'The race for new radiation monitors', *Nature Mater*, vol. 7, no. 5, pp. 343–345, May 2008.

[7] A. Raj Mandal *et al.*, 'Online X-ray radiation induced attenuation of RPL Dosimeters: Dose rate dependence at high doses', *IEEE TNS*, pp. 1–1, 2025.

[8] A. Hasan *et al.*, 'Online and offline Radiation-Induced Attenuation measurements on FD-7 radiophotoluminescence dosimeters irradiated at high X-ray doses', *Radiation Measurements*, vol. 177, p. 107246, Sep. 2024,

[9] Y. Aguiar *et al.*, 'Dose rate effects in Ag-doped metaphosphate glass radiophotoluminescent dosimeters up to MGy range', *IEEE TNS*, pp. 1–1, 2025.

[10] Y. Aguiar *et al.*, 'Analysis of the Thermal Annealing Regeneration Process of RPL Dosimeters for High Dose Levels', *IEEE TNS*, pp. 1–1, 2025

[11] S. W. S. McKeever, S. Sholom, and N. Shrestha, 'Observations regarding the build-up effect in radiophotoluminescence of silver-doped phosphate glasses', *Radiation Measurements*, vol. 123, pp. 13–20, Apr. 2019.

[12] T. Kurobori, *et al.*, 'Characterisation and unique behaviours of radiophotoluminescence Ag-activated phosphate glass under high-dose gamma and high-LET particle irradiation', *Radiation Measurements*, p. 107376, Jan. 2025

[13] D. Aubert *et al.*, 'A 6 MeV electron linac facility for multipurpose radiation testing', in *RADECS 2016*, Bremen, 2016, pp. 1–3.

[14] T. Sato *et al.*, 'Features of Particle and Heavy Ion Transport code System (PHITS) version 3.02', *Journal of Nuclear Science and Technology*, vol. 55, no. 6, pp. 684–690, Jun. 2018

Sensitivity degradation and regeneration behavior in silver-doped RPL glass dosimeters under multiple thermal annealing cycles

Y. Aguiar[*,‡], M. Ferrari[*], A. Raj Mandal[*], M. Avesani[*], R. G. Alía[‡], S. Girard[*,†]

[*] Université Jean Monnet Saint-Etienne, CNRS, Institut d'Optique Graduate School, Laboratoire Hubert Curien UMR 5516, F-42023, Saint-Etienne

[‡] European Organization for Nuclear Research (CERN), CH-1211 Geneva, Switzerland

[†]Institut Universitaire de France (IUF) Ministere de l'Enseignement Superieur et de la Recherche sis 1 rue Descartes 75005 Paris, France.

ABSTRACT

Silver-doped radiophotoluminescent (RPL) glass dosimeters are increasingly used in radiation dosimetry due to their high stability, broad linear dose response, minimal signal fading, and potential for multiple reuse. Thermal annealing is essential for regenerating these dosimeters by erasing the accumulated radiation signal. However, repeated high-temperature annealing may induce degradation mechanisms that compromise dosimetric accuracy and sensitivity. This study systematically investigates the impact of multiple high-temperature annealing cycles on the sensitivity and regeneration performance of Ag-doped phosphate glass RPL dosimeters. The results provide insight into their long-term reliability and inform their use in high-dose environments, such as accelerator and reactor facilities.

PACS Keywords: dosimetry, radiophotoluminescence, high-temperature annealing

1 INTRODUCTION

Radiophotoluminescent (RPL) glass dosimeters, particularly those doped with silver (Ag), have emerged as leading candidates for passive dosimetry in demanding radiation environments due to their high stability, excellent dose linearity, negligible signal fading, and the potential for reuse through thermal regeneration [1-3]. High-temperature annealing is commonly employed to erase the accumulated dose information by dissociating radiation-induced optical centers. However, depending on the temperature conditions, repeated annealing cycles may introduce risks to the dosimeter's structural and optical integrity, potentially leading to sensitivity drift [3-5]. This paper investigates the effects of multiple high-temperature annealing cycles on the dosimetric sensitivity and regeneration efficiency of silver-doped phosphate glass RPL dosimeters. The aim is to assess their long-term reusability and performance in high-dose radiation applications.

2 RPL DOSIMETERS AND HIGH-TEMPERATURE ANNEALING

The dosimeters evaluated in this study are commercial cylindrical FD7 silver-doped phosphate glass dosimeters (1.5 mm diameter, 8.5mm length) supplied by Chiyoda Technol, Japan. Upon irradiation, ionizing radiation induces the formation of electron-hole pairs, which are trapped at both intrinsic point defects, such as Phosphorous Oxygen Hole Center (POHC), and silver-induced extrinsic defect sites. This results in the formation of luminescent RPL centers (Ag^0 and Ag_2^+) and color centers responsible for optical attenuation and glass darkening. After stimulation with UV light, these centers relax emitting visible radiation characterized by two primary emission bands: ~450 nm (Ag^0, blue) and ~630 nm (Ag_2^+, orange) [6]. The concentration of RPL centers and the color centers defines the operational range and sensitivity of RPL-based dosimetry systems. Although there is still no consensus on the specific RPL centers responsible for luminescence in silver-doped phosphate glass dosimeters [6,7], it is well established that radiation-induced free electrons are captured by silver ions (Ag^+), forming Ag^0 optical centers, while the capture of free holes leads to the creation of Ag^{++} centers.

A distinct advantage of RPLDs is their potential for reuse via thermal annealing, which dissociates both RPL and color centers [3]. However, the effectiveness and safety of this process depend critically on the annealing temperature, heating/cooling rates, and the defect density in the glass, which itself is dose-dependent. The annealing efficiency is therefore influenced by both the thermal stress applied and the concentration of optical centers. A central mechanism contributing to sensitivity loss is luminescent center depletion, thermal treatments leading to a reduction of active RPL centers. Additionally, annealing promotes Ag^+ ion migration and aggregation, which under certain conditions leads to the formation of silver nanoparticle clusters. This clustering causes luminescence quenching both by reducing the number of luminescent centers (as silver ions convert into

non-luminescent nanoparticles) and by increasing absorption or scattering of the emitted RPL light [4]. The impact of annealing on luminescence depends strongly on the thermal regime. As demonstrated in [4], annealing at temperatures below the glass transition in silicate glasses can enhance photoluminescence, attributed to increased formation of RPL centers without significant nanoparticle growth. A similar enhancement was observed in phosphate glasses [5], where higher annealing temperatures increased emission intensity, although also promoted nanoparticle formation.

3 METHODOLOGY AND RESULTS

Pristine RPL dosimeters will be subjected to multiple thermal treatments at high-temperature annealing conditions (400 °C) and irradiated under X-ray and 60-Co sources. Fig. 1 shows preliminary results of the irradiated dosimeters following the first annealing cycle. Up to approximately 10 kGy, the annealed dosimeters displayed excellent agreement with reference values, with deviations below 10%. At higher doses, however, deviations increased to the 20–30% range, corresponding to a noticeably higher RPL light output from the annealed dosimeters. This increase may result from annealing-induced changes in the glass matrix. The heat treatment can eliminate non-radiative traps, improving the efficiency of RPL center formation, while also promoting Ag^+ ion migration and redistribution. Depending on the annealing conditions, silver ion aggregation may lead to either an increase in luminescent center density or luminescence quenching through the formation of non-luminescent silver nanoparticles and absorption of emitted RPL light [4].

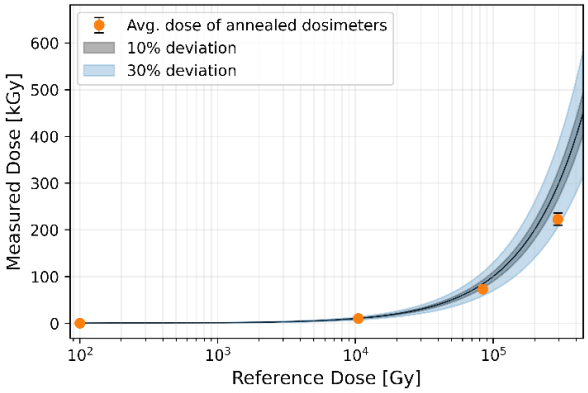

Fig. 1 – Average absorbed dose of annealed dosimeters.

Studies have shown that luminescence can increase at moderate annealing temperatures, particularly below the glass transition, as reported in silicate [4] and phosphate glasses [5], though higher temperatures also promote nanoparticle growth. Thus, while degradation mechanisms such as luminescent center depletion, silver clustering, and matrix restructuring are active, their combined effect may transiently enhance RPL output at high doses. This enhancement does not necessarily indicate improved dosimetry performance, as it also reflects a non-linear interplay between RPL and color centers, both of which influence signal readout. Further investigation is necessary to determine whether the enhanced signal is due to increased RPL center formation or reduced reabsorption by attenuating centers. Ongoing spectroscopic analysis will help clarify the contribution of each factor.

4 CONCLUSION

This study provides a comprehensive evaluation of sensitivity drift and regeneration behavior in Ag-doped RPL dosimeters subjected to high doses and repeated high-temperature annealing. Our findings highlight the complex thermal response of these materials, where annealing-induced structural and chemical changes can both enhance and diminish luminescence, depending on the annealing conditions and accumulated radiation dose. Our results provide practical insight into optimizing annealing strategies and guide future development of more resilient dosimetry materials for use in demanding radiation environments.

REFERENCES

[1] P. E. Wesolowska *et al.*, “Characterization of three solid state dosimetry systems for use in high energy photon dosimetry audits in radiotherapy,” *Radiation measurements*, vol. 106, pp.556-562, Nov. 2017.

[2] D. Pramberger *et al.*, “Characterization of Radio-Photo-Luminescence (RPL) Dosimeters as Radiation Monitors in the CERN Accelerator Complex,” *IEEE Trans. Nucl. Sci.*, vol. 69, no. 7, pp. 1618–1624, Jul 2022.

[3] Y. Aguiar *et al.,* “Analysis of the Thermal Annealing Regeneration Process of RPL Dosimeters for High Dose Levels,” *IEEE Trans. Nucl. Sci.,* March 2025.

[4] Y. Sgibnev *et al.*, Governing Functionality of Silver Ion-Exchanged Photo-Thermo-Refractive Glass Matrix by Small Additives. *Appl. Sci.* **2021**, *11*, 3891. https://doi.org/10.3390/app11093891

[5] M. A. Marzouk *et al*., The effects of delayed annealing on the luminescent activity of heavy metal cadmium zinc phosphate glasses activated by: Er3+ and Tb3+ ions, *Sci Rep* **14**, 5101 (2024). https://doi.org/10.1038/s41598-024-55409-7

[6] S. W. S. McKeever *et al.*, ‘Observations regarding the build-up effect in radiophotoluminescence of silver-doped phosphate glasses’, *Radiation Measurements*, vol. 123, pp. 13–20, Apr. 2019, doi: 10.1016/j.radmeas.2019.02.009.

[7] T. Kurobori *et al.*, ‘Characterisation and unique behaviours of radiophotoluminescence Ag-activated phosphate glass under high-dose gamma and high-LET particle irradiation’, *Radiation Measurements*, p. 107376, Jan. 2025, doi: 10.1016/j.radmeas.2025.107376.

Impact of thermal annealing on radiation induced attenuation for radiophotoluminescence glass dosimeters at high X-ray doses

Aditya Raj Mandal[*], Matteo Ferrari[*], Ygor Aguiar[‡,*], Ruben García Alía[‡], Adriana Morana[*], Matilde Avesani[*], Sylvain Girard[*,†]

[*]Université Jean Monnet Saint-Etienne, CNRS, Institut d'Optique Graduate School, Laboratoire Hubert Curien UMR 5516, F-42023, Saint-Etienne
[‡]European Organization for Nuclear Research (CERN): CH-1211 Geneva, Switzerland
[†]Institut Universitaire de France (IUF) Ministère de l'Enseignement Supérieur et de la Recherche, 1 rue Descartes, 75005 Paris, France.

ABSTRACT

Commercial radiophotoluminescence (RPL) FD7 glasses used as passive dosimeters for personal and medical applications are stable at room temperature, and can be regenerated with thermal treatments at about 400 ºC. However, the validity of those regeneration techniques when RPLs are used for high doses up the kGy and MGy range has to be proven. At such doses the dosimeters darken with dose and so Radiation Induced Attenuation (RIA) becomes relevant for the readout process. This work focuses on the online RIA dependence on both pristine and pre-treated RPL (400°C for 7 hours). Preliminary results collected using X-ray tubes operated at 100 kV up to a maximum dose of 7 kGy allow the possible impact of temperature and of annealing procedures on the RPL readout to be evaluated at high doses.
PACS Keywords: radiophotoluminescence, x-rays, temperature, high level dosimetry, annealing

1 INTRODUCTION

Radiation monitoring in high radiation areas such as particle accelerator, fission reactors or nuclear waste repositories poses various technical challenges and is not sufficiently explored. RPL glasses are among the few reliable dosimetry systems reliable above the kGy. Their main features include small size, low fading and reusability [1, 2].

Following the producer's indication and generally agreed protocols, pre-heating RPL dosimeters at 70°C for 30 minutes ensure stabilization of RPL signal and annealing it at 400°C for 1 hour allows the RPL to be reliably re-used to measure doses up to 1 Gy [2]. Despite their well-known and characterized response for doses up to few hundreds of Gy, the possibility of regenerating RPL dosimeters via thermal treatments for high dose level applications remains to be experimentally verified. Among other applications, this is particularly relevant for CERN, where thousands of dosimeters are exposed to doses up to the MGy level each year along the accelerator complex. In a recent work, the response of annealed RPL dosimeters passively irradiated using γ-rays at doses ranging between 100 Gy and 500 kGy has been compared to pristine ones, evidencing the systematic impact of thermal treatments on the readout. Further experiments investigating the dependency of the high-dose readout system to the modified kinetics of the defects induced by temperature are needed [3].

The present work reports online RIA experiments performed at room temperature under X-ray radiation comparing pristine and thermally treated RPLs. Based on these first findings, future studies will target online RIA experiments performed at different temperatures as well.

2 MATERIAL

Commercial FD7 RPL cylindrical (1.5 mm diameter, 8.5 mm length) glass dosimeters manufactured by Chiyoda Technol, are studied in this work. These are silver-doped (0.17 wt%) polyphosphate glass dosimeters with chemical compositions as P: 31.55 wt%, O: 51.16 wt%, Na: 11 wt% and Al: 6.12 wt% and density of 2.6041 g/cm^3 [4, 5]

3 METHODOLOGY

In this study, both pristine (P) and High-Temperature Annealing (HTA) pre-treated (G0) samples are studied. Figure 1 shows a schematic of the experimental setup used for recording transmitted signal in real time (online) under X-rays. White light is produced by a halogen source and guided through high-OH pure silica optical fibers to a parabolic mirror, collimating the light towards the RPL, that is placed on an aluminum holder allowing the light to pass through the glass sample and with holes blocking excess light. Transmitted light is then collected by a second parabolic mirror after propagation in free space from the irradiated sample. This signal is recorded by a spectrometer.

A 1.5 mm Al filter is used to harden the X-ray spectrum and ensure dose homogeneity [6]. The samples are irradiated at room temperature with an X-ray tube with W target operated at 100 kV at a dose rate of 1.77 Gy[FD7]/s and up to 7 kGy[FD7]. Transmitted signal is recorded before (reference point), during and after irradiation (recovery period). RIA is calculated using equation 1.

$$RIA(t,\lambda) = -\frac{10}{L} log_{10}\left(\frac{I(t,\lambda) - I_N(\lambda)}{I_{ref} - I_N(\lambda)}\right) \quad (1)$$

where L is length of the irradiated sample. I_{ref} (0, λ) and I(t, λ) are the transmitted intensities before irradiation and at time t, respectively at wavelength λ, measured in terms of photon counts. I_N (λ) is the background noise at λ [7].

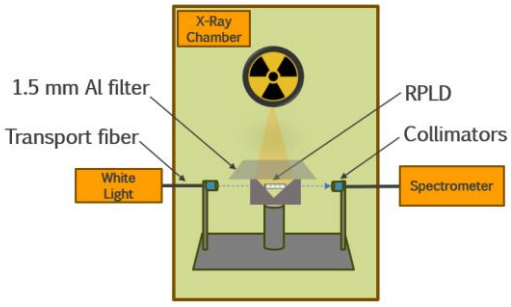

Figure 1: Schematic of the setup to measure the online RIA under X-rays [8].

4 RESULTS

Figure 2 reports RIA growth and recovery (3h) kinetics for P and G0 samples for a selection of wavelengths at room temperature. The RIA evolution of

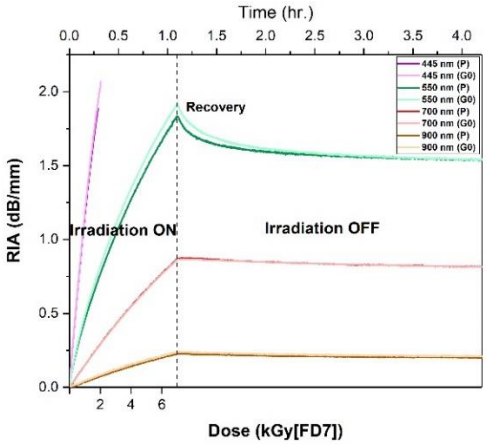

Figure 2: Response of radiation induced attenuation with dose for pristine (P) and annealed (G0) samples.

P and G0 samples seem comparable at most wavelength, except at 550 nm, where RIA is about 0.1 dB/mm higher for the G0 sample at 7 kGy. This difference could be due to presence of metastable defects that stabilizes later in time as suggested by the post-irradiation recovery time. G0 dosimeter hasn't shown degradation at 445 nm wavelength in comparison to the P one, in agreement with what reported by Aguiar et al. [4] at similar doses. RPL readout is being performed at CERN using a system adapted to high doses, exploiting transmission at 445 nm to assess dosimetry.

5 CONCLUSION

RIA experiments seem encouraging in supporting the use thermally annealed dosimeters for dosimetry up to 7 kGy, as minor differences are reported between pristine and annealed dosimeters, and as the impacted wavelengths are not directly concerned by the readout system used at CERN. These studies are pivotal for applications needing large volumes of dosimeters to be regenerated and reused at high doses. Future experiment will include the development of an improved setup with a thermal heating plate to allow online RIA at different temperatures, and so the combined effect of temperature and radiation, to be measured.

REFERENCES

[1] Y. Aguiar et al., "Dose rate effects in Ag-doped metaphosphate glass radiophotoluminescent dosimeters up to MGy range," in IEEE Transactions on Nuclear Science, doi: 10.1109/TNS.2025.3549949.

[2] *Clinical Dosimetry System - Dose Ace*. Available at: https://www.c-technol.co.jp/en/dosimetryequipment/clinicaldosimetry/

[3] Aguiar *et al.*, Analysis of the Thermal Annealing Regeneration Process of RPL Dosimeters for High Dose Levels. IEEE Transactions on Nuclear Science, pp.1–1. doi: 10.1109/tns.2025.3549987

[4] D. Pramberger et al., "Characterization of Radio-PhotoLuminescence (RPL) Dosimeters as Radiation Monitors in the CERN Accelerator Complex," IEEE Trans. Nucl. Sci., vol. 69, no. 7, pp. 1618–1624, Jul 2022.

[5] S. McKeever, A course in luminescence measurements and analyses for radiation dosimetry. John Wiley Sons, Ltd, 2022.

[6] M. Ferrari et al., "Characterization of Radiophotoluminescence Dosimeters Under X-Ray Irradiation at High Doses," in IEEE Transactions on Nuclear Science, vol. 71, no. 8, pp. 1821-1828, Aug. 2024, doi: 10.1109/TNS.2024.3365272.

[7] S. Girard *et al.*, "Growth and decay kinetics of radiation-induced attenuation in bulk optical materials," IEEE Transactions on Nuclear Science, vol. 65, no. 8, pp. 1612–1618, 2018.

[8] A. Raj Mandal et al., "Online X-ray radiation induced attenuation of RPL Dosimeters: Dose rate dependence at high doses," in IEEE Transactions on Nuclear Science, doi: 10.1109/TNS.2025.3546459.

Monte Carlo Simulation dosimetry study of cylindrical FD-7 radiophotoluminescent dosimeters in different radiation environments

M. Avesani[*], M. Ferrari[*], A. Raj Mandal[*], Y. Aguiar[*,‡], S. Girard[*,†]

[*]Université Jean Monnet Saint-Etienne, CNRS, Institut d'Optique Graduate School, Laboratoire Hubert Curien UMR 5516, F-42023, Saint-Etienne
[‡] European Organization for Nuclear Research (CERN):
CH-1211 Geneva, Switzerland
[†]Institut Universitaire de France (IUF) Ministère de l'Enseignement Supérieur et de la Recherche, 1 rue Descartes 75005 Paris, France.

ABSTRACT

We present the results of a simulation study to estimate the dose deposited in radiophotoluminescence (RPL) dosimeters exposed to various fields of ionizing radiations (photons, neutrons and electrons) and for different energy spectra. Commercial cylindrical (1.5 mm diameter, 8.5 mm length) FD-7 silver doped phosphate glasses manufactured by Chiyoda Technology (Japan) and used for dosimetry are considered. Monte-Carlo simulations performed with PHITS allowed us to determine: i) the dose attenuation within the RPL volume, ii) the dose-fluence ratio and iii) the conversion factor from dose to water or silica, often the standard in irradiation facilities, to RPL material, in different irradiation conditions. This set of information supplies reference information that RPL users can exploit to determine the dose absorbed in real irradiation conditions once the fluence is known. The relationship between the dose absorbed in calibration conditions, typically gamma radiation, and more complex operation radiation environment is given.

PACS Keywords: dosimetry, radiophotoluminescence, phits, monte-carlo simulations

1 INTRODUCTION

Radiophotoluminescence dosimeters are widely used for personal and environment dosimetry [1] due to their unique features such as their small size, low dependency on energy, linear response with accumulated dose up to hundreds of Gy, reproducible response, non-destructive multiple readout capability and long stability against fading effects [2]. Their use is currently being extended to much higher doses, up to the MGy level [3]. In light of these considerations, considerations on the dose deposited in RPL dosimeters following exposure to different radiation fields are crucial to assess their response and sensitivity, and extend and consolidate their use beyond traditional photons applications, enabling their deployment in more complex and mixed-field radiation environments.

Computational studies are necessary tools to refine dosimetry, further understand the experimental RPL readout following various irradiations, and to help designing further campaigns [3]. The aim of the work is to provide simulation data for estimating: i) the average deposited dose; ii) the primary radiation field attenuation within the RPL volume, providing information on the dose homogeneity; iii) the conversion factor between dose to water or silica and dose to RPL. This is evaluated for various scenarios of particle types and energy spectra. Specific considerations on the charged particle equilibrium (CPE) information and its impact on deposited dose will be provided. In this work, we produce this information using Monte-Carlo (MC) simulations realized with PHITS [4].

2 METHODS AND TOOLS

2.1 Radiophotoluminescence dosimeters

The studied RPL dosimeters are phosphate glasses doped with silver ions. The commercial FD-7 formulation, reported in Table 1, is used to simulate the dosimeters in the MC model [5]. The RPLs are 8.5-mm long cylinders with a 1.5-mm diameter.

	O [wt-%]	P [wt-%]	Na [wt-%]	Al [wt-%]	Ag [wt-%]	Density [g/cm^3]
FD7	51.16	31.55	11.0	6.12	0.17	2.6041

Table 1: Composition and density of the FD7 glass.

2.2 Monte Carlo model

Simulations are performed with the MC code PHITS (version 3.34) [4]. The RPL is approximated as a rectangular box and the volume is divided into 0.1 mm thick layers to evaluate the homogeneity of the dose deposited throughout the sample with sufficient resolution.

To assess radiation transport, point isotropic sources are compared with monodirectional pencil beam ones to estimate the impact of particle direction on RPL dosimetry. Simulations were performed for of the following source

particles : 60-Co gamma sources (emitting with the same probability two photons of energy 1.17 MeV and 1.33 MeV, respectively), X-ray photons produced by W targets with a tube operating at 100 keV, 160 keV and 225 keV and Al filters to harden the spectrum, a monoenergetic 14-MeV neutron beam and monoenergetic 2.5-MeV and 6 MeV electron beams. These represents standard sources generally available for RPL irradiation and calibration [3]. In addition, selected mixed neutron and gamma fields such as the ones present in nuclear reactor irradiation facilities and near spallation sources are studied.

For each investigated source, the particle fluence and the deposited dose in the RPL sample represented the main calculated quantities. The dose as a function of the sample depth is computed to study its homogeneity within the sample volume. The described methodology mainly targets cylindrical FD7 glass dosimeters, but it can be adapted to other case studies and specific experimental setups. The impact of the specific RPL geometry on the results will be discussed in the extended contribution.

3 RESULTS AND DISCUSSION

In this short abstract, a 14.1-MeV neutron pencil beam source is chosen as example of irradiation condition. The source distribution is designed to allow uniform RPL irradiation.

3.1 Fluence and dose attenuation

Figure 1 displays the simulation results of the attenuation of the fluence and the deposited dose as a function of the RPL thickness. The particle fluence is homogeneous within ±1%, and correspondingly, the deposited dose is attenuated by only 1% throughout the volume, which is generally considered as a very satisfactory homogeneity for these dosimeters.

3.2 Dose-fluence ratio

Average fluence and dose over the whole RPL volume were calculated, leading to a ratio of: 1.92×10^{-11} Gy·cm^2. From this value, it is possible to determine the necessary particle fluence (typically, the information requested by the facility operators) to deposit a desired dose in the dosimeter, a method presented in [6].

This process has been repeated for the selected particle types and energies, and will be reported in the final contribution.

The calculated ratio refers to the specific sample geometry, material, and chosen irradiation conditions. Its dependency on irradiation parameters such as field isotropy and sample geometry or energy spectrum (as in the case of X-ray irradiation) will be further discussed.

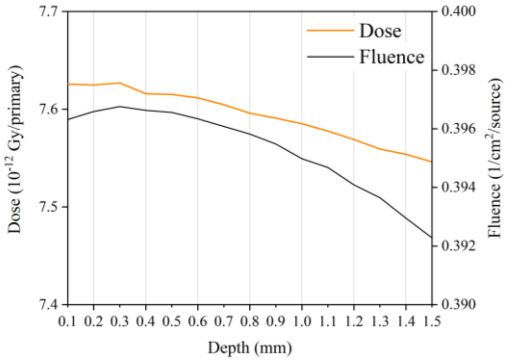

Figure 1: Dose (orange line) and fluence (black line) attenuation within the RPL for 14.1 MeV irradiation.

4 CONCLUSION

The calculated dose-fluence ratios in specific irradiation conditions, and the information on the dose homogeneity can be used to support experimental campaign from the design phase and integrate dosimetry information post-irradiation. Systematic comparisons between these simulation results and the corresponding experiment will allow the response effectiveness of the RPL glasses to various radiations, so far scarcely investigated, to be further assessed.

Parametric simulations studies will allow us to understand to which extent the presented results depend on sample geometry and size, composition of RPL dosimeters, source distribution and directionality.

REFERENCES

[1] A. Raj Mandal *et al.*, "Online X-ray radiation induced attenuation of RPL Dosimeters: Dose rate dependence at high doses," *IEEE Trans. Nucl. Sci.*, pp. 1–1, 2025, doi: 10.1109/TNS.2025.3546459.

[2] M. Ferrari *et al.*, "Characterization of Radiophotoluminescence Dosimeters Under X-Ray Irradiation at High Doses," *IEEE Trans. Nucl. Sci.*, vol. 71, no. 8, pp. 1821–1828, Aug. 2024, doi: 10.1109/TNS.2024.3365272.

[3] Y. Aguiar *et al.*, "Dose rate effects in Ag-doped metaphosphate glass radiophotoluminescent dosimeters up to MGy range," *IEEE Trans. Nucl. Sci.*, pp. 1–1, 2025, doi: 10.1109/TNS.2025.3549949.

[4] D. Pramberger, Y. Q. Aguiar, J. Trummer, and H. Vincke, "Characterization of Radio-Photo-Luminescence (RPL) Dosimeters as Radiation Monitors in the CERN Accelerator Complex," *IEEE Trans. Nucl. Sci.*, vol. 69, no. 7, pp. 1618–1624, Jul. 2022, doi: 10.1109/TNS.2022.3174784.

[5] T. Sato *et al.*, "Recent improvements of the particle and heavy ion transport code system – PHITS version 3.33," *J. Nucl. Sci. Technol.*, vol. 61, no. 1, pp. 127–135, Jan. 2024, doi: 10.1080/00223131.2023.2275736.

[6] D. Lambert *et al.*, "Simulation-Assisted Methodology for the Design of Fiber-Based Dosimeters for a Variety of Radiation Environments," *IEEE Trans. Nucl. Sci.*, vol. 71, no. 8, pp. 1846–1853, Aug. 2024, doi: 10.1109/TNS.2024.3380318.

Wednesday, June 25th

Poster Session

Enhanced Spatially-Resolved Optical Fiber-Based Dosimetry Through Optical Frequency Domain Reflectometry

Jeremy Perrot[*], Adriana Morana[*], Emmanuel Marin[*], Aziz Boukenter[*], Youcef Ouerdane[*], Johan Bertrand[*] and Sylvain Girard[*(**)]

[*]University Jean Monnet Saint-Etienne, CNRS, Institut d'Optique Graduate School, Laboratoire Hubert Curien, UMR 5516, F-42023 Saint-Etienne, France.

[**]Institut Universitaire de France (IUF), Ministère de l'Enseignement Supérieur et de la Recherche, F-75005 Paris, France.

ABSTRACT

We propose a high-resolution (sub-centimeter) distributed dosimetry technique based on phosphosilicate optical fibers and Rayleigh frequency shift signatures. We evaluate the performance of this method, explore its underlying physical mechanisms, and demonstrate its application in a detailed X-ray 2-D dose deposition distribution.

PACS Keywords: dosimetry, ionizing radiations, optical fibers, optical fiber sensors.

1 INTRODUCTION

Silica-based optical fibers offer a plethora of monitoring applications in harsh environments. Its deported, distributed [1] and real-time sensing capabilities allow the monitoring of temperature [2], strain [3], gas concentration [4], water levels [2]. Fiber sensors are also of major interest for dosimetry applications in radiation environments, such as those associated with high energy physics [5] or nuclear reactors [6]. Radiation sensitive optical fibers are commonly doped with either Phosphorus [7] or Aluminum [8] in their cores. It was shown that the infrared Radiation Induced Attenuation (RIA) of P-doped optical fiber linearly grows with the Total Ionizing Dose (TID) up to 500 Gy(SiO_2) without dose-rate dependence. This is exploited by point or distributed dosimeters [9] to monitor the TID level. These properties are explained by the energy and optical properties of P-related color centers [9]. Around 1550 nm, the RIA is governed by the P1 defect having an optical absorption band peaking at ~1569 nm (~ 0.79 eV) and a FWHM of ~ 0.29 eV being very stable at room temperature [10]. Prior studies showed that the radiation sensitivity coefficient of the P-doped fiber around 1550 nm [11] reaches 3 to 4 $dB \cdot km^{-1} \cdot Gy^{-1}(SiO_2)$ [10]. Moreover, no thermal dependence (between -80 °C and +120 °C) of the 1550 nm RIA has been reported [12]. Another important specificity of this material is that its linear sensitivity coefficient of 4 $dB\ km^{-1} \cdot Gy^{-1}$ (at 1550 nm up to 500 Gy) is similar whatever the type and energy of the particle depositing the dose. We have recently demonstrated an improved spatial resolution X-ray dose deposition mapping achieving a 3 cm distributed spatial resolution allowing a precise 2-D dose deposition distribution with a P-doped fiber interrogated by a Rayleigh Optical Frequency Domain Reflectometer (R-OFDR) over several tens of meters of fiber drastically improving the performances (3 cm) [13] of the previously proposed OTDR method (40 cm) [11]. The proposition of using the Rayleigh Frequency Shift (RFS) as the sensing measurand has been investigated for medical applications [14], providing enhanced spatial resolutions (sub centimeters) and proved the feasibility of using such technique for dosimetry applications using fibers doped with Al and Mg nanoparticles. However, the outcome and technique characterization remained unclear and needs deeper investigations, also using a P-doped fiber. In this study we investigate the performances of this R-OFDR for dosimetry proposing the Rayleigh Frequency Shift (RFS) exploitation using a P-doped fiber, understanding its limitations and propose a high spatial resolution mapping. In this work, all the doses are expressed in SiO_2.

2 EXPERIMENTAL SETUP

X-ray irradiations were conducted at LabHX (Hubert Curien Laboratory, France) using a 100 kV tungsten-target X-ray tube, producing photons with a mean energy of ~40 keV. By varying the tube current or height, the dose-rate level can be adjusted. Optical fiber samples (1 m) were coiled as a monolayer spiral of 5 cm outer diameter (homogenize the deposited dose). Whereas one end was spliced to a transport radiation hardened single-mode fiber to deport the sample's R-OFDR responses outside the irradiation zone. The irradiations were performed at 30 °C, stabilized by a thermal plate (±0.1 °C). Each irradiation run reached an accumulated dose of 2 kGy(SiO_2) varying the dose-rate from 10 mGy/s to 4 Gy/s. One hour of recovery phase was recorded after the irradiation end.

3 RESULTS & DISCUSSION

We have measured the temperature stabilized Radiation Induced RFS (RI-RFS) signature evolution with dose up to 2 kGy at 10 mGy/s, 400 mGy/s and 4 Gy/s. Results presented in Figure 1 demonstrate an independence with the dose-rate

of the RFS signatures, within the frequency uncertainty margins (±0.1 GHz) with an averaged sensitivity coefficient of ~5×10^{-4} GHz/Gy. This preliminary measurement highlights the potential of the technique for monitoring the deposited dose. This RFS ($\Delta\nu_R$) is known to originate from a Radiation Induced Refractive Index Change (RI-RIC) (Δn_{eff}) as described in (1), where $\nu_c = \lambda/c$.

$$\Delta\nu_R/\nu_c = -\Delta n_{eff}/n_{eff} \quad (1)$$

The linearity behavior of the RI-RIC over 500 Gy is of interest where the usual OTDR/OFDR traces-based dosimetry applications in the near infrared domain face a sub-linear behavior over this dose threshold. In addition, we observe no variation of the RFS during one hour after irradiation which, at the same temperature and conditions guarantee a deposited dose memory over-time. This is not directly comparable to the RIA as the POHC defect recombining into P1 defects induce a slight increase of the 1550 nm RIA level after irradiation [10].

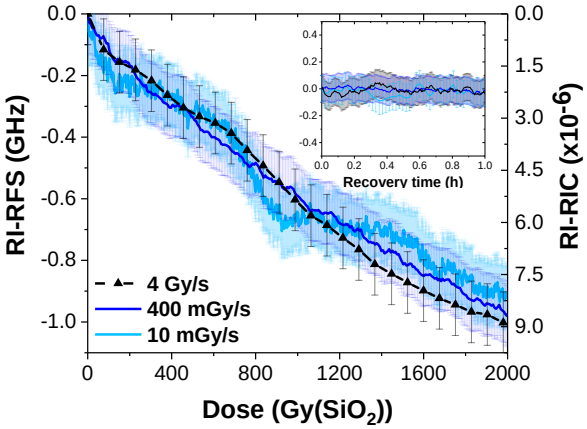

Figure 1: X-ray induced P-doped fiber RI-RFS signatures up to 2 kGy at 10 mGy/s, 400 mGy/s and 4 Gy/s, at 1550 nm.

This linearity at higher doses and absence of signal increase in the recovery phase will be investigated can be explained by a wider RIA contribution than the sole ~1550 nm scanned wavelength from Kramers-Kronig relation [15], with a contribution from the whole spectrum.

In addition, we have assessed the achievable spatial resolution of this technique (Figure 2). Varying the gauge length of the R-OFDR trace, we determine the uncertainty on the RFS signal giving the lowest frequency/dose uncertainty (0.06 GHz/126 Gy) with a spatial resolution of ~ 8 mm. Reducing the spatial resolution, drastically degrades the frequency/dose uncertainties. This method RI-RFS/dose linearity will be investigated for higher doses with ON/OFF sequential irradiations to assess the dose memory capability of this method, also for higher doses. We also aim at improving the fiber RFS sensitivity coefficient with dose, testing this method with Al-doped fibers to resolve lower doses. The final work will present a mapping demonstration providing an X-ray beam surface distribution with an 8 mm resolution.

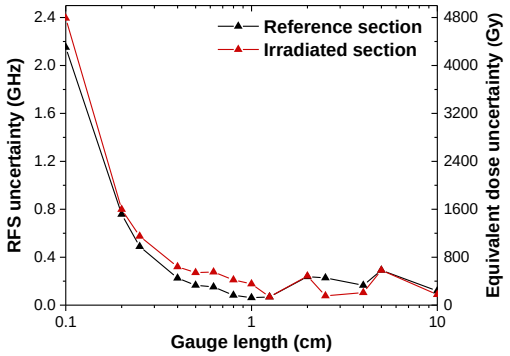

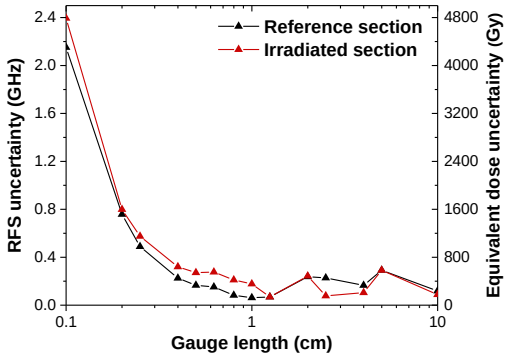

Figure 2: RFS uncertainty in function of the gauge length and its equivalent dose measurement uncertainty.

4 CONCLUSION

We propose a dosimetry technique using a phosphosilicate radiation-sensitive fiber interrogated by a R-OFDR exploiting the distributed fiber RFS signature evolution with dose. We observe a linearity (~4.9 GHz/Gy) between the RI-RFS/RI-RIC with the deposited dose up to 2 kGy with an independence on the dose-rate and with an optimal spatial resolution of 8 mm and a capability to dose memory inducing permanent refractive index increase in the fiber. These promising features are of interest for reliable dosimetry for high doses.

The final work will be complemented with higher dose testing, dose memory testing for multiple consecutive irradiation runs and we will propose improvements of the technique from the fiber sensitivity to conclude with a high spatial resolution X-ray beam shape surface mapping demonstration.

REFERENCES

[1] X. Bao *et al.*, Sensors, vol. 12, nº 7, pp. 8601-8639, June 2012.
[2] S. Rizzolo *et al.*, Sci Rep, vol. 7, nº 1, p. 8766, Aug. 2017.
[3] J. Wu *et al.*, Optical Fiber Technology, vol. 60, Dec. 2020.
[4] S. Rizzolo *et al.*, J. Phys. Photonics, vol. 2, nº 1, Jan. 2020.
[5] S. Girard *et al.*, J. Opt., vol. 20, nº 9, Sept. 2018.
[6] T. Kakuta *et al.*, Journal of Nuclear Materials, vol. 307-311, pp. 1277-1281, Dec. 2002.
[7] M. C. Paul *et al.*, Journal of Non-Crystalline Solids, vol. 355, nº 28-30, pp. 1496-1507, Aug. 2009.
[8] A. Alessi *et al.*, Physica Status Solidi (a), vol. 216, nº 3, Feb. 2019.

[9] D. L. Griscom *et al.*, Journal of Applied Physics, vol. 54, nº 7, pp. 3743-3762, July 1983.
[10] D. D. Francesca *et al.*, *J. Lightwave Technol.*, vol. 37, nº 18, pp. 4643-4649, Sept. 2019.
[11] D. Di Francesca *et al*., IEEE Transactions on Nuclear Science, vol. 66, no. 1, pp. 299-305, Jan. 2019.
[12] G. L. Vecchi *et al.*, Optical Fiber Technology, vol. 55, March 2020.
[13] J. Perrot *et al.*, IEEE Sensors J., vol. 24, nº 13, pp. 20688-20695, July 2024.
[14] M. Olivero *et al.*, IEEE Transactions on Instrumentation and Measurement, vol. 70, pp. 1-9, April. 2021.
[15] N. G. Van Kampen *et al*., J. Phys. Radium, vol. 22, nº 3, pp. 179-191, 1961.

Exploiting the Yb^{2+} Ion Lifetime for Optical Fiber-Based Cryogenic Thermometry

A.K. Alem[*], M. Cieslikiewicz-Bouet[**], M. Bouazaoui[**], E. Marin[*], A. Morana[*], S. Girard[*, ***], H. El Hamzaoui[**], I. Razdobreev[**], A. Cassez[**], V. Andrieux[**], A. Boukenter [*], Y. Ouerdane[*]

[*]Université Jean Monnet Saint-Etienne, CNRS, Institut d'Optique Graduate School, Laboratoire Hubert Curien UMR 5516, Saint-Étienne, France
[**]Univ. Lille, CERLA, CNRS, UMR 8523-PhLAM-Physique des Lasers Atomes et Molécules, F-59000 Lille, France
[***]Institut Universitaire de France (IUF), Ministère de l'Enseignement Supérieur et de la Recherche, 75005 Paris, France

ABSTRACT

The study of the luminescence lifetimes of divalent ytterbium (Yb^{2+}) and trivalent ytterbium (Yb^{3+}) ions in silica glasses are promising for cryogenic temperature sensing down to 10 K. The main goal of this work is to investigate the sensing performance of Yb^{3+}/Yb^{2+} ion doped preform and fiber for lifetime based cryogenic thermometry. The luminescence lifetimes of the fiber sample, originating from a bulk glass preform and having experienced the combined effects of process temperatures and mechanical stresses during its drawing, will be discussed at the symposium. In this abstract, preliminary results regarding the temperature dependence of the Yb^{2+} ion lifetime are reported for the preform sample. The absolute sensitivity of this sample measured at 77 K and at room temperature is 2.3 µs/K and 0.42 µs/K, respectively. This sensor can be utilized for non-contact cryogenic thermometry applications in harsh environment and vibration rich areas such as turbine blades and turbo pumps in extremely low temperature environments. A further systematic investigation of such sensors could reveal possible ways of enhancing their performance and implementation in terms of architecture and optimization of the acquisition chain.

Keywords: Rare earth doped ions, lifetime cryogenic thermometry, optical fibers, preform, fiber drawing

1 INTRODUCTION

Luminescent thermometry is a non-contact technique that utilizes a temperature dependent emission characteristic of rare earth doped ions, transition metal oxide compounds [1], [2], [3] and transition metal oxides with intrinsic emission [4]. This kind of thermometer can use either directly the intensity of the emission signal or its lifetime through intensity decay time measurements. But, compared to the intensity signal, lifetime-based thermometers are intrinsically more stable and less affected by the sensor packaging and implementation. As an example, these sensors can be used for temperature sensing in many industrial use cases such as turbo pumps and turbine blades [4]. Their performance metrics, chemical composition optimization and effect of different stages of manufacturing processes on the sensing parameters still remain complex to fully understand and optimize them for extreme temperature sensing applications. In a recent work [5], divalent ytterbium (Yb^{2+}) ion lifetimes of a custom-made Yb^{3+}/Yb^{2+} co-doped preform silica-based glasses were studied for cryogenic temperature sensing and showed a promising characteristic. All the stages of fiber drawing processes can affect the sensitivity of such glass based cryogenic sensors due to stresses and heat treatments involved at different stages of fiber manufacturing processes. We could then expect different responses between the preform and its fiber counterpart. This will be discussed at the conference.

Heat treatment processes during preform elongation and fiber drawing can alter the lifetime of rare earth ions. For example, in a work by Petr Varak et al. [6], [7], the temporal evolution of erbium, ytterbium and other rare earth ion fluorescence was characterized at distinct steps in optical fiber manufacturing process stages, namely the initial preforms, the elongated preform (cane), the standard fiber, and the over cladded fiber. It was found that process temperature applied to the preforms typically led a faster fluorescence decay, this is due to the diffusion of dopants and the formation of clustering of rare earth ions. To the best of our knowledge, this effect of fiber drawing process in cryogenic temperature region has not been yet systematically studied. So, the main objectives of our study are simplifying the implementation complexity of the preform sample as a cryogenic temperature sensor by using optical fiber sample instead of preform sample and investigating the combined effect of heat treatment and stress introduced during fiber drawing process on the lifetime of Yb^{2+} doped silica based optical glasses in the cryogenic temperature region from liquid nitrogen to room temperature.

2 MATERIALS AND METHODS

A 2 mm thick cylindrical shape Yb^{3+}/Yb^{2+} codoped preform sample has been fabricated using modified chemical

vapor deposition (MCVD) at PhLAM laboratory, University of Lille, France. For the study, the glass sample was placed on a sample holder inside ST-100 optical cryostat from Janis, USA, excited by a UV pulsed laser at 320 nm wavelength and 8 ns pulse width in a transverse direction through the cryostat's optical window. This excitation wavelength was chosen as Yb^{2+} ions are associated with two absorption bands around 300 nm and 400 nm, probably resulting from the $4f^{14} \rightarrow 4f^{13}5d$ transitions [5]. Under this excitation, a broad emission spectrum covering the whole visible range is observed, and currently attributed to the 4f5d→ 4f transition [5]. The fluorescence spectra and decay rates were detected by a gated intensified CCD (Pi-MAX 3 Princeton Instruments) with a 4 µs time window after waiting a minimum of 30 minutes to achieve thermal stabilization at each investigated temperature. The sample temperature from 77 K to room temperature was varied using liquid nitrogen-based optical cryostat and 335-temperature controller from Lakeshore Cryotronics, USA. These reference temperatures were measured using a Si diode-based temperature sensor that comes along with the temperature controller. After recording the fluorescence spectra and decay rates at each temperature, the lifetime was extracted from the fluorescence decay rates using a stretched exponential curve fitting on the fluorescence intensity integrated from 500 nm to 525 nm spectral range. Finally, the lifetimes extracted at different temperatures are calibrated with the reference temperature sensor readings.

3 RESULTS AND DISCUSSIONS

Lifetimes of the Yb^{2+} ions are measured at different temperatures ranging from at 77 K to room temperature. Furthermore, it is also measured at 350 K aiming to see the temperature sensing range of this preform sample. As depicted in Figure (1), the lifetime decreases as the temperature rises to room temperature, which agrees with [5]. This could be due to the fact that thermal energy allows particles to redistribute more rapidly between states, resulting in a faster decay at higher temperatures [4]. Furthermore, red circle dot shows that this sensor lifetime at 350 K does not change significantly as compared to the value at room temperature. Hence, this sensor cannot be used for sensing temperatures higher than 300K. The lifetime versus temperature in Figure (1) for this particular temperature range can be also well fitted with a second-order polynomial function (R^2 =0.9997). This experimentally measured lifetime (τ) temperature dependence can be mathematically modeled using the fitted equation as follows:

$$\tau\ (\mu s) = 0.0042 \times T^2 - 2.9388 \times T + 546.98 \qquad (1)$$

Where T is the temperature in units of kelvin. The measured absolute sensitivity at liquid nitrogen temperature and room temperature is found to be 2.3 µs/K and 0.42 µs/K respectively.

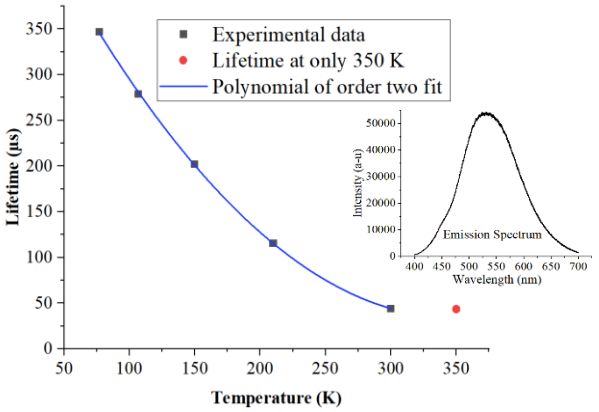

Figure 1: Lifetime versus temperature.

Error bars for the temperature and lifetime are not included in the plots as they are smaller than the symbol size used in the plot. The errors associated with the lifetime measurement is less than 3.2 µs. Additionally, a typical emission spectrum at an excitation wavelength of 325 nm is included in Figure 1 as an inset. Fiber sample preparation from University of Lille, France, from a similar preform is in progress and the fiber will be tested and results will be analyzed for the symposium.

4 CONCLUSSIONS

These preliminary results showed the feasibility of using Yb^{2+} doped preform silicate glass sample as the sensitive element of a cryogenic sensor by exploiting the ion lifetime temperature dependence from liquid nitrogen to room temperature. This dependency can be well fitted by a polynomial function of order two. Its absolute sensitivity measured at 77 K and room temperature is 2.3 µs/K and 0.42 µs/K respectively. The effect of different fiber manufacturing process stages such as preform elongation and fiber drawing on the lifetime of such glasses will be investigated for the conference.

REFERENCES

[1] S W Allison et al., Nanotechnology, 14, 859, 2003.
[2] M.D. Chambers, and D.R. Clarke, Annual Review of Materials Research 39, pp. 325 - 359, 2009
[3] V. B. Mykhaylyk et al., MDPI Sensors, 20, 5259,2020
[4] N. Ahmed et al., Materialia, 4, 287-296, 2018
[5] Hicham El Hamzaoui et al., MDPI Sensors, 24, 248, 2024
[6] Petr Varak et al., Optical Materials: X, 15, 100177, 2022
[7] Petr Varak et al., Optics Express, 30, 10050-10062, 2022

Feasibility of In Vivo Dosimetry in Contact Radiotherapy Using a Germanium-Doped Silica Optical Fiber

Gevorg SHUMILOV[a], Clémence GENTNER[a], Régis AMBLARD[a], Rémy VILLENEUVE[a], Nicolas GARNIER[a], Karine BENEZERY[b], Hicham EL HAMZAOUI[c], Monika BOUET[c], Mohamed BOUAZAOUI[c], Franck MADY[d], Mourad BENABDESSELAM[d] et Benjamin SERRANO[a]

[a] Centre Hospitalier Princesse Grace, Division de Radiophysique et Radioprotection, avenue Pasteur, 98000 Monaco
[b] Centre Hospitalier Princesse Grace, Service de Radiothérapie, avenue Pasteur, 98000 Monaco
[c] Université Lille, CNRS UMR 8523 – PhLAM – Physique des Lasers Atomes et Molécules, 59000 Lille, France
[d] Université Côte d'Azur, Institut de Physique de Nice, UMR 7010, 06200 Nice, France

INTRODUCTION

In the context of skin tumor treatments, contact radiotherapy is rapidly gaining ground. However, certain anatomical locations, such as the nasal fold, eye corner, or ear fold, introduce uncertainties in the absorbed dose, and in vivo dosimetry could help improve treatment accuracy and safety in such cases. An optical fiber (OF) appears to be a promising candidate for this purpose, due to its high sensitivity to X-rays, an effective atomic number ($Z_{eff} \approx 10$) close to soft tissue ($Z_{eff} \approx 7.4$), and its small size (core diameter ≈ 50 µm; outer diameter < 150 µm). We propose to investigate the response of an optical fiber to X-rays and to evaluate its performance in a clinical scenario using an anthropomorphic phantom.

PACS Keywords: optical fiber, dosimetry, in vivo, skin contact radiotherapy, germanium dopped silica.

1 MATERIALS AND METHODS

Previous studies have shown that appropriate germanium (Ge) doping provides the OF with a particularly strong radioluminescence (RL) response[2]. The emitted RL is guided to the optical detection system via a silica transport fiber, welded to a 1 cm segment of Ge-doped fiber that serves as the sensitive element. The dosimetric properties of the OF were characterized using an Xstrahl 100 contact radiotherapy unit delivering X-rays at tube voltages of 50, 80, and 95 kV. A flat 0.02 cc ionization chamber (ref. 23342 PTW) was used simultaneously as a reference dosimeter. To assess the influence of field size, circular collimators with diameters of 2, 3, 4, 6, and 8 cm were employed.

2 RESULTS

The results obtained for all three tube voltages show that the response of the OF is proportional to that of the ionization chamber (IC), with excellent linearity. The correlation coefficients (R^2) are 0.9992, 0.9990, 0.9986, 0.9991, and 0.9992 for collimator diameters of 2, 3, 4, 6, and 8 cm, respectively. An example of this linear relationship for a collimator diameter of 2 cm is shown in Figure 1. The measurements exhibit very good repeatability: 0.4% for the OF compared to 0.2% for the IC. Reproducibility, which is influenced by OF positioning, is 2.6% versus 0.3% for the IC.

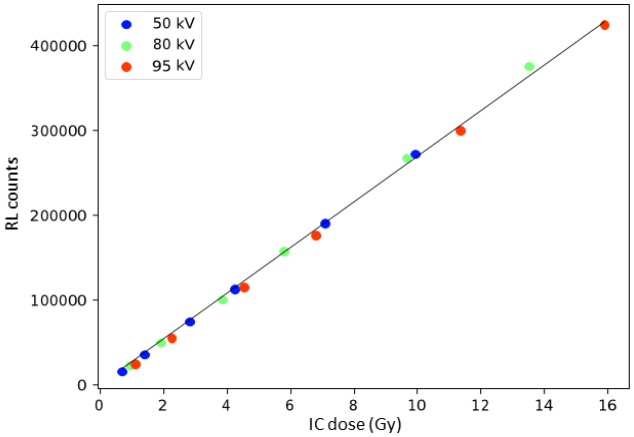

Figure 1: Linearity of the OF response as a function of the dose measured by the IC for a collimator with a 2 cm diameter.

The response of the OF to variations in the radiation field at all three tube voltages follows the same trend as that of the IC. However, a slight increase in the discrepancy between the responses of the two detectors is observed as the field size increases (Figure 2).

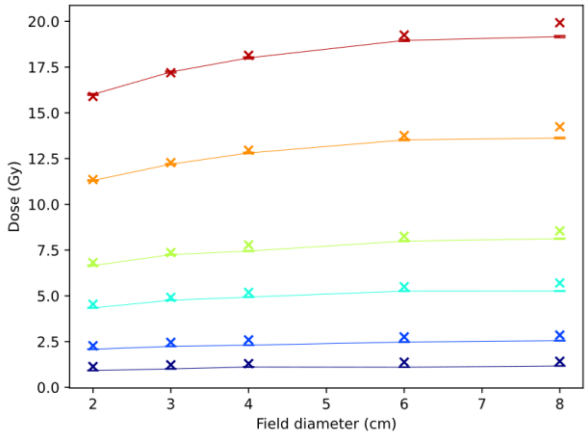

Figure 2. Dose dependence as a function of field size for 9.5% Ge-doped OF (-) and IC (x) at 95 kV.

Figure 3. In vivo dosimetry measurement on an anthropomorphic phantom in the nasal fold.

Measurements performed on an anthropomorphic phantom under clinical conditions (Figure 3) show deviations from the prescribed dose of $2.2 \pm 0.8\%$ on a flat surface and $8.1 \pm 2.3\%$ on an irregular facial area, without applying any distance correction.

3 CONCLUSIONS

This study demonstrates the feasibility of using a Ge-doped silica optical fiber as a potential in vivo dosimeter for contact radiotherapy. A future clinical implementation will require several improvements, such as complete protection of the detection chain from ambient light shielding of the detection system and robustness of the sensitive element.

REFERENCES

[1]. Nestor et al., Consensus Guidelines on the Use of Superficial Radiation Therapy for Treating Nonmelanoma Skin Cancers and Keloidspie, J Clin Aesthet Dermatol, Feb 1;12(2), 2019

[2]. Benabdesselam et al., Ge-Doped Optical Fibers for Passive and Active Radiation Detection Modes. IEEE Sensors Journal, 23, 7, 2023.

Hybrid sol-gel waveguide sensor for damage detection in aerospace domain

Maxime Royon*, Damien Jamon*, Thomas Blanchet*, François Royer*, Francis Vocanson*, Emmanuel Marin*, Adriana Morana*, Aziz Boukenter*, Youcef Ouerdane*, Yves Jourlin*, Sylvain Girard*

*Laboratoire H. Curien, UJM-CNRS-IOGS, Université de Saint-Etienne, 18 rue du Pr. Benoît Lauras, 42000 Saint-Etienne, France

ABSTRACT

The potential of sol–gel-based optical sensors is investigated for applications in the aerospace domain. To this aim, a low-cost and non-intrusive sol–gel sensor based on waveguides, arranged as a 2D matrix structure, is fabricated by UV photolithography for delamination and damage detection. Two different organic–inorganic sol–gels were selected to fabricate the photonic device: TiO_2–SiO_2 and ZrO_2–SiO_2, acting as the waveguide core and the cladding, respectively. A systematic study was performed to determine the manufacturing parameters controlling their properties. The results show that large surfaces can be functionalized via sol–gel methods using the direct laser-writing approach. The structures are characterized in terms of refractive index, and the guiding properties were investigated, indicating an excellent behavior regarding the light guidance in a straight waveguide or in the 2D matrix structure grid. Additionally, tests show that the presence of impact can be easily detected after damage through the induced optical losses on large surfaces.

PACS Keywords: sol-gel, photolithography, damage sensing, direct writing technique.

1 INTRODUCTION

The sol–gel chemistry process, based on hydrolysis and condensation reactions [1], is an elegant technique used for the low-temperature synthesis of optical materials. This soft chemistry route allows the fabrication of various optical elements in large applicative fields including the fabrication of waveguides with a very high transparency in the telecommunication ranges. Metal alkoxides precursors (from Ti, Zr, Si…) are used to create an inorganic metal oxides matrix (TiO_2, ZrO_2, SiO_2…), and the resulting materials can be tailored in terms of mechanical and optical properties by adjusting the chemical conditions and the molar ratio. The use of precursors containing an organic chain can confer a UV photosensitivity to the final mixture, a crucial step regarding the manufacturing of sol–gel devices. Sol-gel materials are negative photoresists where the zone exposed to UV photons is polymerized, inducing a densified pattern. During the development process in an alcoholic solution, the area exposed to UV photons is not removed while the unexposed one is dissolved, revealing the photonic device.

In the framework of the Cleansky2 (Horizon 2020) project advanced damage detection through optical sensor network (ADD-ON), we demonstrate the feasibility of using a non-intrusive sol–gel approach for damage sensing over large surfaces [2, 3]. More specifically, a low-cost sensor for delamination and damage detection based on the light transport of sol–gel waveguides is presented. This photonic device should be integrated on aircraft parts, such as wings, considering the specific environmental constraints of the aerospace domain for SHM usage. Figure 1 illustrates the targeted final architecture of the sensor to be manufactured. This latter is based on waveguides arranged as a 2D sol–gel grid able to be deployed on a large surface (40 cm x 40 cm). After light injection into all the waveguides, the detection and impact localization can be clearly observed through the 2D mapping grid, where the optical mode extinction or intensity decrease indicates the presence of damages.

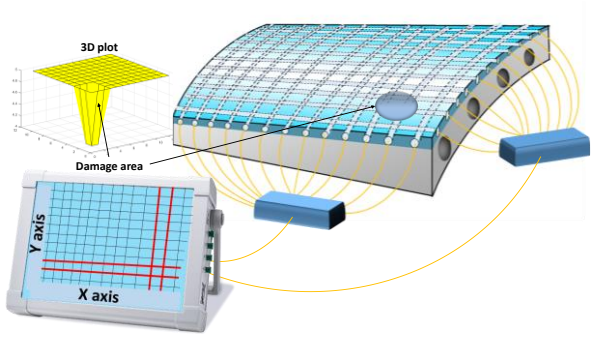

Figure 1: Final architecture of the 2D sol-gel matrix sensor for damage detection.

2 RESULTS AND DISCUSSION

To create the waveguide sensors, two homemade organic–inorganic solutions are synthesized and used as the core (TiO_2-SiO_2) and the cladding (ZrO_2-SiO_2) acting as a protective layer. One of the primary goals of the UV photolithography is the optimization of the refractive index

contrast (Δn) between the core and the surrounding environment (air, substrate, protective layer…) fostering the best performances possible of sol–gel photonic devices in terms of low losses and mode confinement. This optical property is obtained via ellipsometry technique revealing an excellent contrast where Δn ranging from 6.3 x 10^{-2} (@630nm) and 5.3 x 10^{-2} (@1550 nm).

In order to create TiO_2-SiO_2 sol-gel waveguides, the direct writing technique was investigated using the Dilase 750 facility : the sample is placed on a computed translation stage allowing motion in the X and Y direction on long distance (40 cm x 40 cm). The insolation is performed by an UV source emitting at 375 nm and focused on the sol-gel layer. Figure 2 reveals the impact of the laser and the scanning speed of the stages on the lateral dimension (width) of the sol-gel waveguides: the extremal widths of waveguides that we can obtain are between roughly 4 µm to 20 µm.

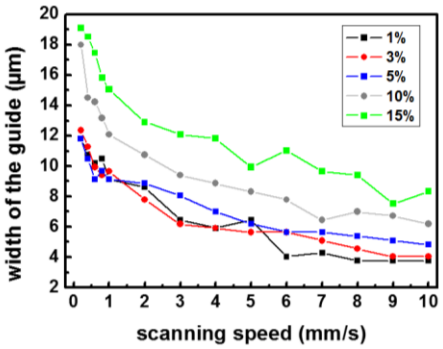

Figure 2: Width of the TiO_2-SiO_2 guides as a function of the scanning speed for different laser energies.

The proof of concept sensor was achieved on a 40 cm x 40 cm soda-lime glass substrate. The photo-induced device comprises a grid of 62 lines separated by a 1 cm distance as shown in Figure 3(a). A microscope image is also given focusing on the crossed area(b).

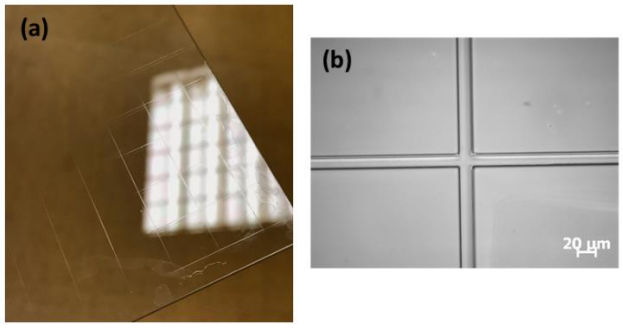

Figure 3: (a) Overview of the grid. (b) microscope image of the doubled exposed zone.

The light transport on this architecture was evaluated using a butt coupling configuration at 638 nm: the light is coupled in the different waveguide using a SMF28 while a camera is dedicated to the output light observation once imaged through a long working distance 20 x microscope objective. It is to note that the light transport is still efficient for long waveguides (> 30 cm).

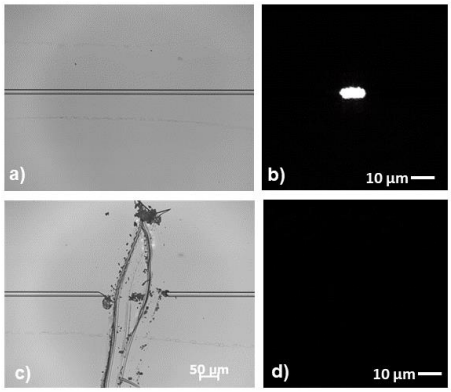

Figure 3: Light guidance in a TiO_2-SiO_2 waveguide. (a) unaffected waveguide before impact. (b) Corresponding output optical guided mode at 638 nm. (c) waveguide after impact. (d) Absence mode observation.

The feasibility of using such device as a damage sensor is investigated in figure 3. The results presented are related to the case where the TiO_2–SiO_2 waveguide is deposited on soda-lime glass and surrounded by the air. To this aim, Figure 3(a) illustrates a waveguide before any impact through the microscope image. The corresponding mode at 638 nm (b) is given showing the satisfying guiding properties. A series of damages were made on the substrate until affecting one of the guides. After being impacted (c), we can clearly observe the specific zone of the damage. For this latter, the characterization of the optical mode was also performed. The result presented in (d) shows the alteration of the mode and the absence of light after the damage. These results highlight that this device based on the light transport can operate as an on/off sensor.

ACKNOWLEDGEMENTS

This project has received funding from the Clean Sky 2 Joint Undertaking under the European Union's Horizon 2020 research and innovation program under grant agreement n°785341.

REFERENCES

[1] Hench, L.L. et al. The sol-gel process. Chem. Rev., 90, 33–72. 1990
[2] Royon, M. et al, aerospace, 8, 109, 2021.
[3] Royon, M. et al, aerospace, 8, 401, 2021.

Influence of OH content and pre-irradiation on the radiation-induced luminescence of pure-silica-core optical fibers

Mario Coto[1], Adriana Morana[1], Luca Weninger[1], Fiammetta Fricano[1], Sylvain Girard[1,2]

[1] Laboratoire Hubert Curien, Université Jean Monnet Saint-Etienne, Saint-Etienne, France
[2]Institut Universitaire de France, Paris, France

ABSTRACT

This study compares the nature of the X-ray radiation-induced luminescence (RIL) of multimode pure-silica-core (MM-PSC) optical fibers containing different levels of hydroxyl groups (OH). The effects of pre-irradiation up to 14 kGy on the RIL is also investigated.

PACS Keywords: pure silica core, radiation-induced effects, luminescence, hydroxyl.

1 INTRODUCTION

Pure Silica Core (PSC) optical fibers are well-suited for radiation environments due to their high resistance to ionizing damage, particularly at total doses exceeding 10 kGy [1]. For these PSC fibers, the precise control of the OH and chlorine (Cl) amounts is crucial as these two impurities significantly influence defect generation under irradiation [2]. Based on OH levels, PSC fibers are typically classified as wet (high-OH), dry (low-OH), or medium OH, each exhibiting distinct optical responses. Radiations induce, in PSC fibers, point defects such as non-bridging oxygen hole centers (NBOHCs) and SiE′ centers, which contribute to both radiation-induced attenuation (RIA) and luminescence (RIL) [2]. OH groups act as precursor sites for generating NBOHCs under ionizing radiation exposure, leading to a characteristic red emission around 650 nm [3]. Dry fibers exhibit a lower concentration of such precursors, while medium OH fibers demonstrate intermediate behavior. These insights are valuable for optimizing the use of these PSC fibers in radiation-sensitive applications, particularly as radiation hardened transport fibers in combination with scintillating optical fibers, e.g., for dosimeter architectures. For this reason, it is very interesting to investigate their radioluminescence properties.

2 MATERIAL AND METHODS

The irradiations were performed with the X-ray machine LabHX of Lab. Hubert Curien (Saint-Etienne, France) that has a tungsten target, operating at 100 kV, to produce X-ray photons with a mean energy fluence of 40 keV.

Figure 1 illustrates the experimental setup. Three types of PSC multimode (100 µm core diameter) optical fibers with low, medium, and high OH contents were irradiated. Fibers ($L = 7\ m$) were routed through the irradiation chamber, leaving external segments connected to PMTs (counting units C8855-01), and spectrometers (type H7421-40), both from Hamamatsu, via fast optical connectors, then from the same fiber, segments ($L_s = 5\ cm$) were centrally located and secured between tungsten shields (labeled S1 and S2) to ensure localized irradiation exposure. For each type of fiber, the fiber itself was used as transport fiber, i.e., sample and transport fiber are the same, no splice needed. PMTs and spectrometers were shielded from ambient light. To investigate the pre-irradiation effects, the experiment consisted of a calibration study of the RIL as a function of dose before and after a long run-up to 14 kGy.

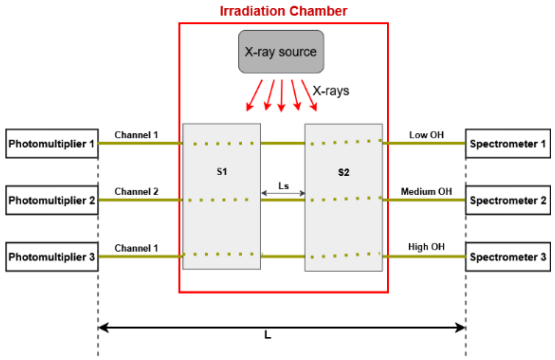

Fig.1. Schematic of the experimental setup.

Figure 2 illustrates the irradiation pattern applied during the pre- and post-irradiation experiments. The setup consists of sequential irradiation intervals using increasing current levels from 0.08 up to 30 mA in discrete steps, corresponding to a dose-rate in SiO_2 from 20.33 $mGy\ s^{-1}$ to 7.5 $Gy\ s^{-1}$. Each current level is maintained for 20 s, followed by a 40 s pause. After reaching the peak current (30 mA), the sequence continues with decreasing current levels, referred to as returning points, which are essential for analyzing potential saturation effects and the reversibility of the intensity response. This structured pattern allows assessment of the linearity between induced intensity and dose, as well as the stability of the optical response following exposure to high radiation levels. During the long irradiation, all fibers were exposed for 10^5 s at a dose rate of 0.139 $Gy[SiO_2]s^{-1}$, resulting in a total delivered dose of about 14 kGy.

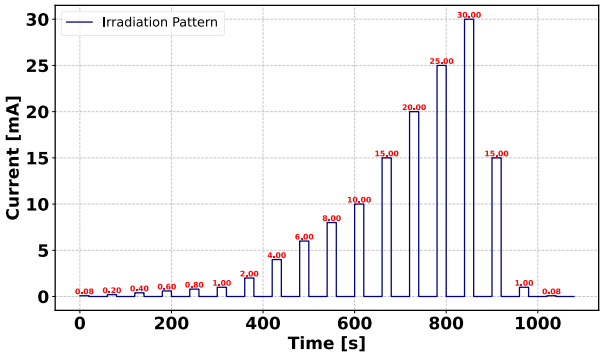

Fig.2. Irradiation pattern for pristine and post-irradiation.

3 RESULTS AND DISCUSSION

Figures 3 to 5 show the dose-response behavior for PSC fibers with varying OH content, comparing pristine and post-irradiation conditions under increasing and returning dose segments. Insets highlight the kinetic response at the highest current level. As detailed in Table 1, the slope of the linear fit reflects RIL sensitivity, the R^2 indicates the linearity of the intensity-dose relationship, and ΔI values describe the radiation-induced effect based on relative intensity changes, between post and pristine curves, at the 15th step (the one with the highest dose-rate (at ~950 s) and at the 16th step (at ~975 s) kinetic peaks.

Table 1. Summary of slopes, linearity (R^2), and intensity change (ΔI).

	Fiber type	Slope (pristine)	Slope (post)	R^2 (pristine)	R^2 (post)	ΔI_{max}(%) @ ~950 s	ΔI_{min}(%) @ ~975 s
1	Low OH	17943.11	19019.75	1.000	0.9999	8.76	4.52
2	Medium OH	12065.86	16967.51	0.9999	0.9991	31.76	26.82
3	High OH	15029.84	23920.53	0.9977	0.9912	34.09	34.30

The low-OH fiber exhibits the highest RIL sensitivity after 14 kGy dose (slope ~19k), nearly perfect linearity (R^2 = 1.0000 pristine, 0.9999 post), and the smallest ΔI values (8.76%, 4.52%). These characteristics point to a very stable RIL response with minimal saturation or attenuation effects, making it a strong candidate for high-dose rate dosimetry applications. For the medium-OH fiber, the pristine slope is the lowest (~12k), confirming reduced RIL yield. Instead, post-irradiation intensity increases significantly (slope ~17k), it retains excellent linearity (R^2 = 0.9999 pristine, 0.9991 post) and moderate ΔI values (31.76%, 26.82%). The relatively lower sensitivity and high stability make it particularly suitable as a transport fiber, where minimal signal interference is desirable under prolonged exposure. In contrast, the high OH fiber shows the strongest RIL increase post-irradiation (slope ~24k) and the highest ΔI (34.09%, 34.30%), but a noticeable decline in fit quality (R^2 = 0.9977 pristine, 0.9912 post). Additionally, the returning segments consistently lie below the increasing ones, suggesting cumulative RIA and partial saturation due to an enhanced NBOHC generation favored by higher OH content through to the cleavage of ≡Si–O–H bonds [1,2]. Overall, these results confirm the crucial role of OH level in modulating the RIL response of PSC fibers. Higher OH content increases sensitivity but compromises linearity and reversibility, while lower OH levels ensure more stable and predictable RIL behavior under extended irradiation.

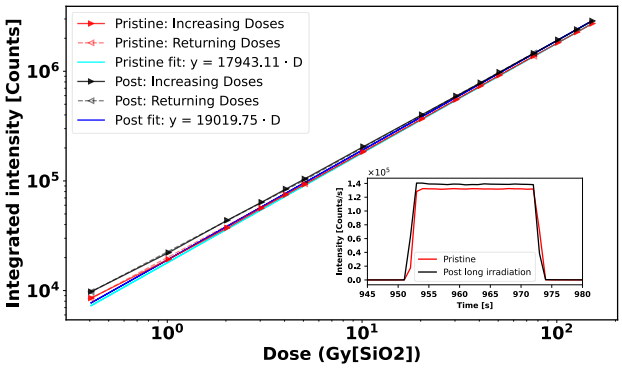

Fig.3. PSC low OH fiber intensity responses.

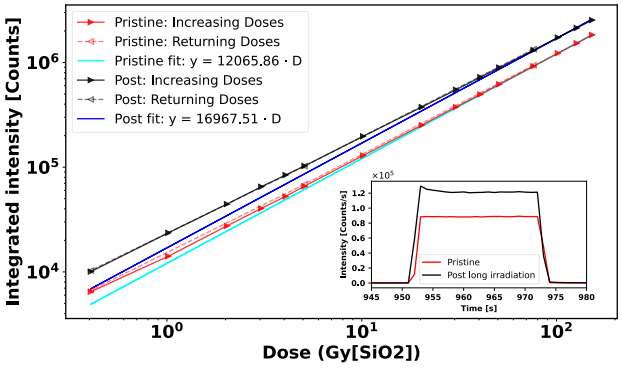

Fig.4. PSC medium OH fiber intensity responses.

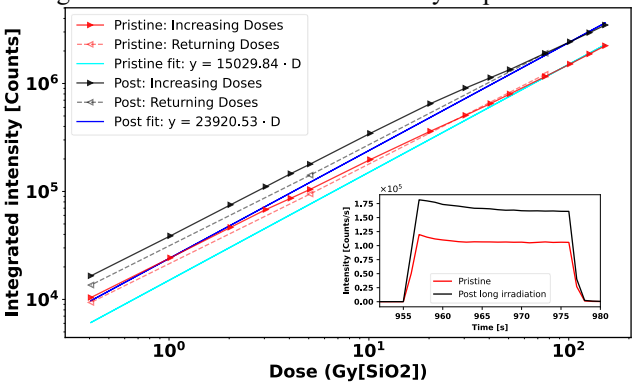

Fig.5. PSC high OH fiber intensity responses.

REFERENCES

[1] Girard, S. et al. *Overview of radiation induced point defects in silica-based optical fibers.* IEEE Transactions on Nuclear Science, 60(3), 2013.
[2] Campanella, C.; Radiation Effects on Pure-Silica Multimode Optical Fibers in the Visible and Near-Infrared Domains: Influence of OH Groups. Appl. Sci. 2021, 11, 2991.
[3] Fricano, F., et al. *Preirradiation Treatment Influence on the Radioluminescence of a Nitrogen-Doped Optical Fiber Dosimeter.* Physica Status Solidi A, 221(3), 2024. DOI: 10.1002/pssa.202300665.

Optical fibers irradiation at the n_TOF NEAR station at CERN: a Monte Carlo simulation dosimetry study

M. Avesani[*], J. Perrot[*], Y. Aguiar[*,‡], A.P. Bernardes[‡], M. Cecchetto[‡], R. Garcia Alia[‡], D. Ricci[‡], M. Calviani[‡], S. Girard[*,†], M. Ferrari[*]

[*]Université Jean Monnet Saint-Etienne, CNRS, Institut d'Optique Graduate School, Laboratoire Hubert Curien UMR 5516, F-42023, Saint-Etienne

[‡] European Organization for Nuclear Research (CERN): CH-1211 Geneva, Switzerland

[†]Institut Universitaire de France (IUF) Ministère de l'Enseignement Supérieur et de la Recherche, 1 rue Descartes 75005 Paris, France.

ABSTRACT

The NEAR neutron and gamma mixed-field irradiation station at CERN is used for the passive irradiation of commercial components and materials, including optical fibers, for high radiation applications. This study presents simulation results aimed at estimating the dose deposited in the various components of an optical fiber (coating, cladding and core) and in an optical fiber coil at different irradiation positions where neutron with energies ranging from thermal to hundreds of MeV, high energy photon and electrons are present. Monte Carlo simulation results calculated with PHITS, combined with the experimental results, provide deeper insight into dose deposition within the optical fiber. This work offers valuable indications for irradiations of optical fibers in mixed radiation fields, particularly for the optimization of the experimental setup to enable accurate dosimetry.

PACS Keywords: optical fiber, dosimetry, PHITS, Monte-Carlo simulations, mixed radiation fields

1 INTRODUCTION

Optical fibers (OF) are widely used in radiation environments as their sensitivity to radiation can be controlled by manufacturing the core and the cladding with appropriate compositions [1], [2] , [3]. OF-based sensors can be used for radiation monitoring in a variety of applications including nuclear, space, high energy physics and radioactive waste storage. As the development of devices operating in extreme condition continue to progress and radiation environments are becoming more challenging, further experimental and computational studies are necessary to characterize the vulnerability and evaluate the possible use of OF in these new conditions. A selection of OF samples was passively irradiated at NEAR [5] during operational year 2023, aiming at assessing neutron and gamma radiation effects on both optical properties and mechanical coating degradations. Computational investigations performed with Monte Carlo (MC) tools are essential to calculate the deposited doses in complex radiation environments and deepen the comprehension of experimental radiation effects. The aim of this simulation work is threefold: i) to estimate the dose deposited in the different OF components (coating, cladding and core); ii) to evaluate the dose distribution in a realistic sample configuration, such as an OF coil; and, iii) to assess the Charge Particle Equilibrium (CPE) conditions within the sample geometry. This information is vital to use NEAR for OF irradiation.

2 IRRADIATION FACILITY AND TOOLS

2.1 NEAR irradiation test station

The NEAR irradiation test station of the neutron time-of-flight (n_TOF) facility at CERN is a parasitic, mixed-field, neutron-dominated irradiation station [4], allowing materials and components to be exposed to a unique combination of spallation neutron spanning over 11 decades of energy and high-energy gamma fields. Three irradiation positions are available at NEAR [4][5]: top shelf (TS), closer to the source; bottom shelf (BS); and, a bottom box (BB), situated below both shelves. In these positions, samples are irradiated for about one year of operation time, absorbing mixed neutron and gamma doses within the MGy range. In an irradiation campaign realized in 2023, nine OF samples have been irradiated in these three positions. An extensive characterization combining both optical and mechanical measurements has been realized [5].

2.2 Monte Carlo model

To assess radiation transport in the OF, a two-step simulation approach is used. First, particle energy spectra and fluence distributions are calculated with FLUKA [7] at the irradiation positions. An example of the resulting spectra is reported in Figure 1. In the second step, these spectra were used to generate isotropic sources to compute more effectively and in a simpler geometry, the radiation transport in the OF using PHITS (version 3.34) [6]. This approach improves computational efficiency and accuracy. Three different geometries are studied: 1) a bulk cylindrical volume (radius 1.5 cm and 1 cm) made of silica, acrylate and polyimide to assess the dosimetry in the different materials; 2) a 2-cm long optical fiber segment made of three concentric cylinders simulating the core (diameter of 10 µm) , cladding

(silica and diameter of 125 µm) and coating (acrylate or polyimide); 3) a more realistic optical fiber coil configuration, to investigate the CPE conditions and potential self-absorption phenomena. Particle fluence and the deposited dose are the main calculated quantities.

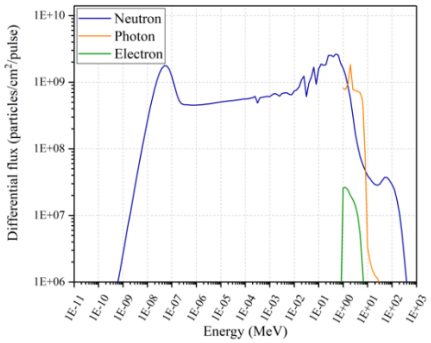

Figure 1: Radiation spectra in the TS.

3 RESULTS AND DISCUSSION

The results reported in Figure 2 refer to NEAR irradiation conditions with 3.371428×10^6 proton pulses [5]. The dose components are shown for each material in the three irradiation positions, with contribution separated by particle type (neutrons, photons and electrons) in the bulk material. Across all the materials, the total dose in the BS position is up to 9% higher than in the TS. The dose contributions from electrons and photons are relatively constant in all positions and materials. However, the total dose in the BB is significantly lower than in BS: reduced by 85% in acrylate, 12% in polyimide, and 28% silica. Neutron contributions dominate the dose in hydrogen-containing materials, accounting for ~60-80% of the total dose in acrylate and polyimide in the three positions. On the other hand, in silica, a hydrogen-free material, the neutron contribution is only about ~30% of the total dose. The difference in the neutron dose strongly depends on the material composition: materials containing hydrogen like acrylate and polyimide (H mass fraction of 7% and 3%, respectively) absorb more dose due to higher fast neutron scattering probability in comparison to hydrogen-free silica. Similar to what observed for the bulk materials, the electron and photon dose contributions are relatively constant across the three positions and different OF segment (acrylate coating, silica cladding and silica core). However, the gamma dose contributions are ~95% lower in the fiber geometry configuration than in the bulk material, leading to a general decrease of the total doses. This might indicate that CPE conditions are not met in a single OF layer in the NEAR environment. In the silica cladding and core, the electron contribution reaches ~50-60% of the total, while in the acrylate coating, neutron interactions dominate, contributing about 88% of the total dose. Moreover, the total absorbed dose in the silica core and cladding is ~82% lower than that in the coating across all irradiation positions. This results suggests that, under mixed-field exposure, the acrylate coating may be the most radiation-sensitive element of the OF, potentially compromising its correct operation. CPE conditions and OF spool modelling will be further discussed in the extended manuscript.

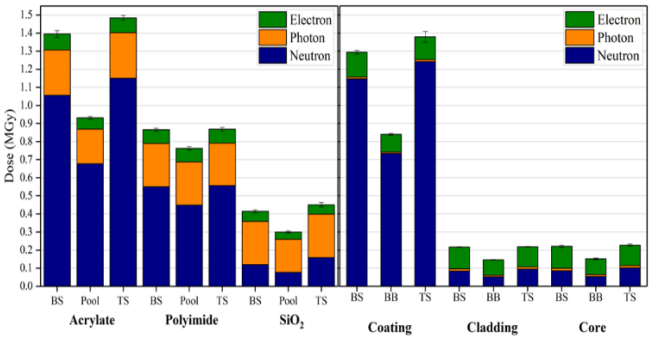

Figure 2: Dose components in the NEAR irradiation position in bulk materials (left) and in the components of a single layer of OF (right).

4 CONCLUSION

The performed MC simulations show that the material composition and sample geometry significantly influence dose deposition in optical fibers used in mixed-field environments. These findings highlight the need for realistic modelling including full optical fiber geometry, spool configuration and the radiation environment to accurately estimate absorbed doses . Such considerations are crucial for supporting future experiments and better interpreting radiation-induced degradation mechanisms. The strong dependence of neutron dose on fiber geometry and coating material could offer a concrete path for radiation-hard fibre design.

REFERENCES

[1] S. Girard *et al.*, "Overview of Radiation Effects on Silica-Based Optical Fibers and Fiber Sensors," *IEEE Trans. Nucl. Sci.*, vol. 72, no. 4, pp. 982–1020, Apr. 2025, doi: 10.1109/TNS.2024.3511455.

[2] Y. Bao and G. Chen, "High-temperature measurement with Brillouin optical time domain analysis of an annealed fused-silica single-mode fiber," *Opt. Lett.*, vol. 41, no. 14, p. 3177, Jul. 2016, doi: 10.1364/OL.41.003177.

[3] R. Janani *et al.*, "From acrylates to silicones: A review of common optical fibre coatings used for normal to harsh environments," *Progress in Organic Coatings*, vol. 180, p. 107557, Jul. 2023, doi: 10.1016/j.porgcoat.2023.107557.

[4] M. Ferrari *et al.*, "Design development and implementation of an irradiation station at the neutron time-of-flight facility at CERN," *Phys. Rev. Accel. Beams*, vol. 25, no. 10, p. 103001, Oct. 2022, doi: 10.1103/PhysRevAccelBeams.25.103001.

[5] J. Perrot *et al.*, "Mixed Neutron and Gamma Effects on Optical Fibre Glass and Coating Materials".

[6] T. Sato *et al.*, "Recent improvements of the particle and heavy ion transport code system – PHITS version 3.33," *Journal of Nuclear Science and Technology*, vol. 61, no. 1, pp. 127–135, Jan. 2024, doi: 10.1080/00223131.2023.2275736.

[7] G. Battistoni *et al.*, "Overview of the FLUKA code," *Annals of Nuclear Energy*, vol 82, pp. 10-18, Aug. 2015, doi: 10.1016/janucene.2024.11.007.

Pulsed X-ray Radiation Responses of Single-Mode and Multimode Fluorine-doped Optical Fibers

V. De Michele[*], C. Marcandella[**], P. Paillet[**], S. Girard[*,***]

[*]Université Jean Monnet Saint-Etienne, Laboratoire Hubert Curien, F-42023, Saint-Etienne, France
[**]CEA, DAM, DIF, F-91297 Arpajon, France
[***] Institut Universitaire de France (IUF) Paris, 75005, France

ABSTRACT

This study compares the pulsed X-ray radiation responses of different two super-radiation-hardened (SRH) single-mode (SM) and multimode (MM) optical fibers to more conventional optical fibers. Real-time (ms) measurements of radiation-induced attenuation (RIA) spectra were conducted right after the pulse within the spectral range of 0.8 eV to 3.0 eV (400 – 1600 nm) both at room temperature (RT) and at liquid nitrogen temperature (LNT) allowing to characterize the contribution from metastable defects that are rapidly bleached after the short irradiation pulse. Additionally, we monitored the RIA kinetics at 1550 nm from the nanosecond timescale to several hundreds of seconds. Results show that the MM-SRH presents limited transient RIA for shortest times after pulse(<100 µs), lower than other optical fibers and clearly better than the SM-SRH that present the worst transient response. Possible explanation of this radiation hardness could be the very specific F-doping gradient in this fiber that should reduce the precursor sites for self-trapped holes.

PACS Keywords: Optical fibers; Transient defects, radiation effects; Harsh environment; Silica.

1 INTRODUCTION

Operating under particular extremely harsh environments, such as the ones encountered in megajoule class laser facilities [1], requires for the optical fiber a high radiation tolerance level. Indeed, the main radiation induced degradation mechanism corresponds to the degradation of the fiber transmission caused by the RIA explained by the generation of absorbing points defects in the fiber core and cladding [2]. In particular, if the pure-silica-core (PSC) or F-doped optical fibers are the best compositions for operation under steady-state X-ray or γ-ray irradiation, their transient RIA response (during the first µs after a X-ray pulse) is however known to exceed the one of Ge-doped fiber and even the one of the radiation sensitive P-doped OFs [3]. In order to reduce the darkening of the optical fibers under pulsed X-rays, we investigate here a new type of super-radiation hardened SM and MM optical fibers that contain fluorine in both the fiber core and cladding. To highlight the performance of these two optical fibers, we have studied their online RIA, both at RT and LNT, induced by pulsed X-ray at the Asterix facility from the CEA Gramat [4], representing a model for ignition shots at megajoule class laser facilities. Through this comparison, the attenuation analysis shows that the transient RIA in the MM-SRH fiber is significantly lower than in other optical fibers, particularly at early times after the pulse. This improved performance at short timescales after the pulse contributes to redefining the classification of the most radiation-tolerant optical fibers under pulsed radiation.

2 EXPERIMENTAL SETUP

Irradiations were performed at RT and LNT using the ASTERIX X-ray pulsed facility (Gramat, France). The dose and dose rate (that can largely exceed than 1 MGy/s) depend on the distance of the sample from the source. The main sample under test are two super-radiation hardened optical fibers: a multimode (MM-SRH) fiber characterized by a graded refractive index profile achieving through the F-doping (largest concentration in the cladding) and a single-mode (SM-SRH) optical fiber containing a low level of F in its core and a larger one in the cladding to ensure an higher refractive index in the fibers' core. Fig. 1 compares the radial distributions of F, as measured by Energy Dispersive X-ray Spectroscopy (EDX), for the two fibers.

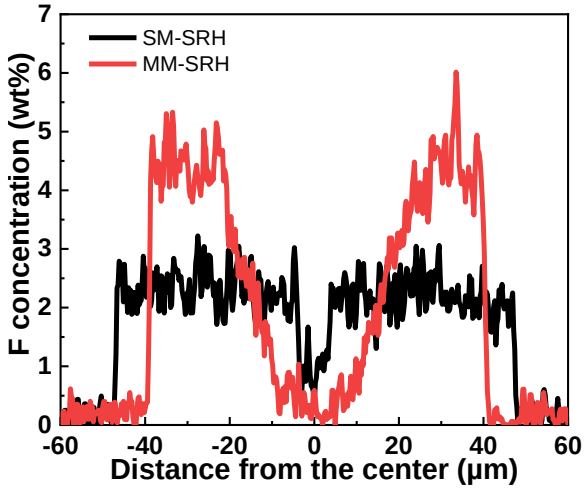

Figure 1. Radial Fluorine distributions measured by EDX along the SM and MM SRH fibers' diameter.

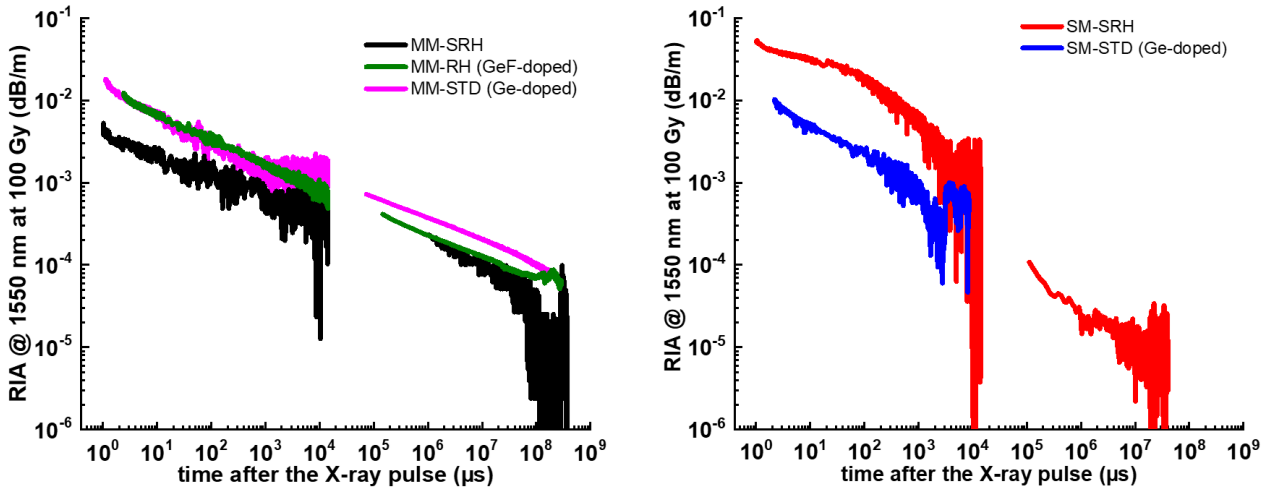

Figure 2. Post-pulse recovery kinetics for the different tested fibers measured at 1550 nm as a function of the time after the X-ray pulse. At right are reported the class of MM fibers: SRH (high fluorine content) in black, RH (GeF-doped) in green and Ge-doped in magenta. At left are reported SM fibers: SM SRH as F-doped in red and SM Ge-doped in blue.

Samples under test consist of fiber coils with diameters of 8 cm and lengths dependent on the investigated spectral range and total accumulated dose. The sample under test are connectorized with fc-pc connectors to fiber pigtails, themselves connected to sources (DH2000 both for the UV/vis and the NIR) and detectors (HR4000 spectrometers from Ocean Optics for the UV-Vis measurements; NIR512 spectrometer NIR measurements). The online RIA technique, used during the experiments, consists in evaluating the transmission loss in an optical fiber just after the X-ray pulse. Moreover, measurements characterized by a fast time resolution, of the order of nanoseconds (ns), are performed using a laser at 1550 nm as the source and fast photodiodes to record the transmission changes. An oscilloscope acquires the photo-generated current in order to measure the RIA.

3 RESULTS

Based on the comparison shown in Figure 2, it is possible to monitor the RIA kinetics at 1550 nm from the nanosecond scale up to several hundred seconds after the pulse. While conventional fluorine-doped fibers as the SM-SRH optical fibers exhibit strong transient RIA shortly after the X-ray pulse (as shown in the right panel of Figure 2), the induced losses in the MM SRH fiber (characterized by a higher fluorine level in the cladding and a gradual doping in the core) are clearly lower than those of other classes of optical fibers, considered as the most radiation tolerant under pulsed X-rays. Furthermore, to better characterize the MM-SRH and SM-SRH fiber transient responses, we performed a Gaussian decomposition of the RIA spectra, acquired a few ms after the pulse, to investigate defect generation and the annealing processes at both room temperature and liquid nitrogen temperature.

The aim of this work, that will be presented at the symposium, is to investigate the role of the fluorine in the glass matrix. This analysis reveals a significant influence of self-trapped hole (STH)-related band contributions in the RIA kinetics, highlighting their nature as matrix-dependent defects, as previously observed in Ge-doped fibers [5]. Indeed, STHs are primarily responsible for the post-pulse attenuation in all types of radiation-tolerant optical fibers. It has also been established that, in conventional F-doped fibers, as the SM-SRH, the presence of this dopant could increase the internal stress within the glass matrix [6], promoting the formation of strain-assisted STHs, as illustrated in the right panel of Figure 2.

In contrast, fibers with a the fluorine gradient exhibit a reduced contribution from strain-assisted STHs, suggesting that with a certain fluorine doping level and profile, the matrix undergoes structural relaxation, which mitigates STH generation processes under pulsed X-rays.

These measurements demonstrate that RIA in optical fibers strongly depends on both fiber composition (e.g., core/cladding dopants) and manufacturing parameters such as fiber treatment, fictive temperature, and density fluctuations.

REFERENCES

[1] S. Girard et al., IEEE Trans. Nucl. Sci. 2005, 52, 1497.
[2] S. Girard et al., Rev. Phys. 2019, 4, 100032.
[3] S. Girard et al., IEEE Trans. Nucl. Sci. 2005, 67, 289.
[3] A. Johan et al, Ann. Phys. 1989, 14, 379.
[4] V. De Michele J. Appl. Phys. 128, 103101 (2020).
[5] S. Girard, Phys. Status Solidi A 2018, 1800547.

Radiation response of different types of germanosilicate multimode optical fibers

Allan Travailleur[1], Sylvain Girard[2,3], Marie-Noëlle de Noirfontaine[1], Nadège Ollier1[1], Mattia Fanetti[3], [1]Olivier Cavani, Antonino Alessi[1,4]
[1]Laboratoire des solides irradiés, CEA, DRF, IRAMIS, CNRS, École Polytechnique, Institut
[2]Laboratoire Hubert Curien, CNRS, Université Jean Monnet, 42000 St-Etienne, France
[3]Institut Universitaire de France, Paris, France,
[3]Materials Research Laboratory, University of Nova Gorica, 5270 Ajdovščina, Slovenia
[4]Department of Physics and Chemistry Emilio Segrè, University of Palermo, Via Archirafi 36, 90123 Palermo, Italy

ABSTRACT

Several multimode optical fibers (OF), responding to the standards of ISO/IEC and named OM1 to OM5, are manufactured by Corning InfiniCor. They correspond to different refractive-index profiles to adjust the bandwidth achievable in data transfer [1].

From several years, Ge-doped silica is used for the production of Telecom optical fibers. Ge doping is widely used to increase the refractive index of the core of the silica matrix and allows second harmonic generation [2]. By contrast, the Fluorine in the cladding leads to a decrease in the refractive index; this combination of doping ensures the guiding of the light inside the core of the OF.

At the same times, the Ge doping also increases the sensitivity to radiations of the silica. Thus, a lot of research has been done to know the radiation effects on microscopic and macroscopic (refractive index or structural modification) properties [3], when this telecom-fibers are used for data transfer in radiation environments.

As a consequence, Ge-doped silica based fibers can be found in various nuclear or space applications. Since the functionality of a fiber is based on its ability to transmit signals, it is crucial to evaluate how radiation can affect its optical properties. Furthermore, since the radiation response of a fiber depends on the production parameters, the modifications introduced in the family OM1-OM5 can implies a difference of sensitivity of these fibers, and this imposes their characterization before a real application.

In addition to optical absorption experiments electron paramagnetic resonance (EPR) measurements can be used to investigate the radiation response of fibers [4]. In the case of Ge doped silica, the literature has highlighted the generation of three well know paramagnetic defects named E'Ge, Ge(1), and Ge(2) [5]. The E'Ge is constituted by an unpaired electron localized on a three coordinated Ge atoms, the microscopic structure of Ge(1) consists of an electron trapped on tetra-coordinated germanium atom. Finally, for Ge(2) is still under debate, but a relatively accepted structure is an unpaired electron localized on a tri-coordinated Ge atom, two normally length and a longer one. Even if their absorption bands are far from the telecom windows, their generations or conversions are related to ionization, electron trapping, or bond-breaking processes. As a consequence, the radiation sensitivity of a specific fiber can be investigated by studying their concentrations as a function of the dose or other irradiation parameters (such as dose rate, temperature, or irradiation source) [2].

This paper aims to highlight the behavior of the OM family irradiated with different doses, dose rates, and types of radiation (X-rays, Gamma rays, and electron beam) as those encountered in different radiation environments to compare their general radiation responses.

PACS Keywords: Radiative response, Irradiation, Germanium point defects, Electron Paramagnetic Resonance spectroscopy (EPR), Telecom Optical fibers.

1 METHODS

To characterise these optical fibres and radiation effects, the chemical composition was characterised by energy dispersive X-ray spectroscopy (EDX). Electron paramagnetic resonance (EPR) measurements were performed to estimate the concentration of germanium-related paramagnetic defects. A JEOL Resonance-ES11030MWU was used for these experiments. All data were recorded at room temperature. Gamma irradiations were performed at room temperature at IRMA in 2022. It's a panoramic irradiation cell used to study the effects of dose or dose rate effects induced by gamma photons on matter. These irradiations were performed with different doses (50, 200, 500 and 1000 kGy) and dose rates: 0.025, 0.093, 0.23 and 0.44 Gy/s. The electron irradiations were performed at SIRIUS (LSI Polytechnic School). The irradiations were performed with the irradiation cell named CIRANO at room temperature with a beam energy of 2.5 MeV, with dose rates of 2.7, 50, 100, 5000 Gy/s and with multiple irradiations. The X-ray exposures were performed on the LabhX facility

located at the Hubert Curien Laboratory in St-Etienne. Different dose rates were used, such as 0.005, 0.01, 0.1, 0.2, 0.448, 1, 2.16 Gy/s.

2 RESULTS

The EDX experiments, **Fig.1A**, show that OM (2-5) optical fibers have a parabolic-like Ge concentration profile (max. 4.5 %At) with a core size of 50µm, while OM1 has maximum Ge concentration of 8.8 %At with a core size of 60 µm. In addition, in **Fig.1B**, all fibers contain similar Fluorine concentration profile in the cladding, except for the OM1, where Fluorine is not detected.

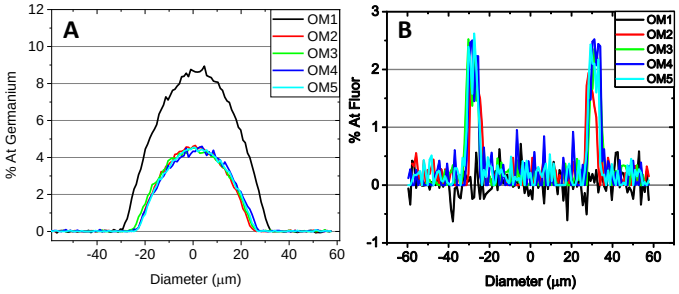

Figure 1: Ge (panel a) and F (panel b) content as a function of the distance from the center of the fiber.

EPR data (**Fig.2**) show that the normalized double integral of the EPR spectra recorded for different samples as a function of the accumulated dose. Panel (a) illustrates the data recorded for the gamma irradiated fibers, while panel (b) and (c) show the data acquired for the electron and the X-ray irradiated one respectively. In all the panels the points reported at 10^{-4} kGy represent the values measured in the pristine samples in which the signal is due to the E'Ge and E'Si generated during drawing. By comparing the different fibers, it is possible to note that the total concentration is within the experimental error the same for all the OM, despite the difference of the doping profiles of the OM1. The only minor dissimilarity is the fact that at some doses the contribution of the E'Ge seems to be slightly higher in the OM1. This can be explained by the fact that OM1 is the only optical fiber with no Fluorine doping in the cladding. And thanks to the literature, we know that doping fluorine decreases stress bonds within the silica matrix. It is important to underline that the fibers feature the same behavior regardless of the type of irradiation and dose rate.

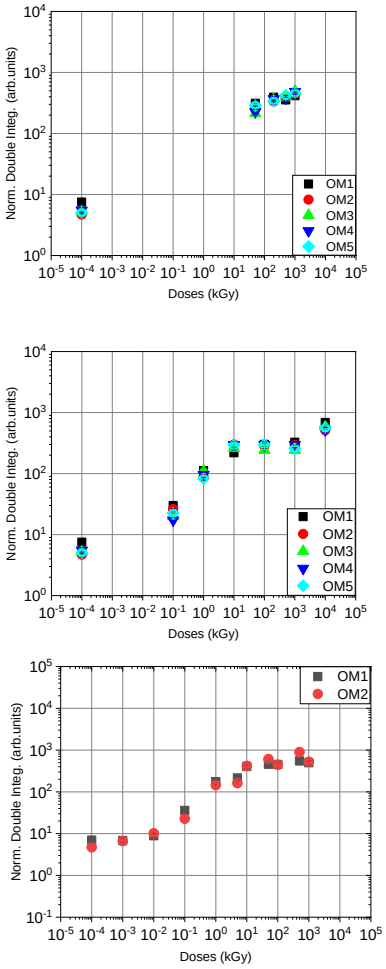

Figure 2: Normalized double integral evaluated as a function of the dose in the different optical fibers after gamma (panel a), electron (panel b) and X-ray (panel c) irradiation.

ACKNOWLEDGMENTS

This work is contributed by slovenian research agency (bilateral aris-cea project nc-24005)

REFERENCES

[1] « CISCO », Understanding the Differences Between OM4 and OM5 Multimode Fiber.
[2] S. Girard *et al.*, *Reviews in Physics*, vol. 4, p. 100032, nov. 2019.
[3] A. Alessi *et al.*, *J Mater Sci*, vol. 52, nº 18, p. 10697-10708, sept. 2017.
[4] D. P. Poulios, *J. Phys.: Condens. Matter*, vol. 12, nº 38, p. 8309-8319, sept. 2000.
[5] L. Giacomazzi, *Opt. Mater. Express*, vol. 5, nº 5, p. 1054, mai 2015.

Radiation Responses of Ultra-Low-Loss/Low Loss Pure-Silica-Core Optical Fibers up to MGy Dose Levels

G. Ciachera[*], A. Morana[*] , M. Darnon[*], M. Fanetti[**], A. Alessi[***,‡], S. Girard[*,†]

[*] Lab. Hubert Curien, Université Jean Monnet, 42000 Saint-Étienne, France
[**] Materials Research Laboratory, University of Nova Gorica, 5270 Ajdovščina, Slovenia
[***]Laboratoire des solides irradiés, CEA/DRF/IRAMIS, CNRS, École Polytechnique, Institut Polytechnique de Paris, F-91128, Palaiseau, France
[‡]Department of Physics and Chemistry Emilio Segrè, University of Palermo, 90123 Palermo, Italy
[†] Institut Universitaire de France (IUF) Paris, 75005, France.

ABSTRACT

We investigated the X-ray radiation induced attenuation (RIA) in the visible to near-IR domains of three different commercially-available ultra-low loss (ULL) / low loss (LL) pure-silica-core optical fibers that were manufactured by the Axial Vapor Deposition (AVD) process.

PACS Keywords: pure silica core fibers, radiation effects, radiation induced attenuation, point defects

1 INTRODUCTION

Nowadays, ULL single-mode optical fibers have become a highly attractive technology for long-distance communication systems. By design, ULL fibers exhibit extremely low attenuation along their entire length, minimizing signal losses at the 1550 nm third telecom windows. This property enables the deployment of terrestrial and submarine long-haul links with a significantly reduced number of optical repeaters and regenerator, as reported in [1] for Pure-advanced fibers type. Consequently, ULL fibers contribute to lowering the overall cost of data transmission by reducing the need for expensive optical amplification systems. One particularity of these fibers is that to reduce the fiber intrinsic attenuation, the core is made of pure silica or fluorine-doped silica glass and not of Ge-doped silica as in older generation of Telecom-grade optical fibers. As a consequence, these fibers are expected to be radiation hardened, at least to steady state irradiations. However, in previous studies [2] [3], an Ultra-Low Loss (ULL) optical fiber from Corning, branded as Vascade EX1000, was tested and associated with an extreme RIA increase up to 3000 dB/km at 1200 nm following exposure to a total ionizing dose (TID) of 2 kGy[SiO_2] [3]. This fiber was manufactured using the Outside Vapor Deposition process [4] [5]. Since that times, more of these ULL fibers from different manufacturers have shown similar radiation sensitivities.

In the present work, we investigate three ULL/Low-Loss Pure Silica Core Fibers (LL-PSCF) produced by Sumitomo Electric Industries via the VAD process [6]. Fibers under investigation are designated ZLL, Z+150 ULL, and Pure-Advance 80 and are all with pure-silica/fluorine doped cores, as proved by EDX measurements (to be shown at the conference). The main objectives of this study are first to characterize the radiation response of these three fibers, second to investigate the origins of the RIA up to 2 MGy[SiO_2] from the visible to near-IR domains.

2 MATERIALS AND METHODS

2.1 Materials

Table 1. gives the main irradiation conditions at room temperature for the RIA measurements. For the irradiation we used the MOPERE-X irradiation machine from LabHC that, when operated at 100 kV, provides X-rays with a mean energy fluence of ~40 keV.

Fiber name	Dose rate	TID	Length (m)	Loss in dB/km @1550nm
Z+150-ULL	7.055Gy/s	2.7MGy	1	0.144
ZLL	7.3Gy/s	2MGy	4	0. 156
PA-80	7.3Gy/s	2MGy	2	0.160

Table 1: Irradiation conditions

2.2 Method

We performed RIA experiments on the optical fiber samples described in Table 1 and calculate the RIA at each time (dose), wavelength, by applying the following formula:

$$RIA(\lambda,t) = \frac{10}{L} \times 10\log_{10}\left(\frac{I(\lambda,t)_{Irrad} - N(\lambda)_S}{I(\lambda,t)_{ref} - N(\lambda)_S}\right)$$

Where L is the length of the fiber, $I(\lambda,t)_{irrad}$ represent the light intensity received by the spectrometer during the irradiation. $I(\lambda,t)_{ref}$ is the intensity of the light received by the spectrometer before irradiation. $N(\lambda)_s$ is the setup noise reference taken by switching off the light source.

3 RESULTS AND DISCUSSION

3.1 Kinetics

The RIA dose dependences at 1310 and 1550 nm are given in Fig 1 (a) and (b) for the three tested optical fibers.

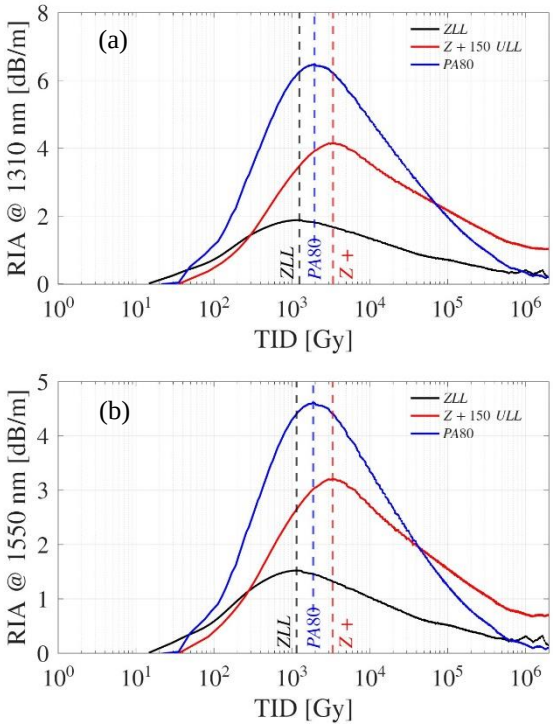

Figure 1: RIA kinetics of ZLL, Z+150 ULL and Pure advanced 80 optical fibers at 1310 nm (a) and 1550 nm (b) in function of the TID.

A detailed analysis will be provided in the final paper. However, preliminary observations indicate that at both wavelengths, all samples exhibit a similar trend, close to the ones reported for the Vascade optical fiber [3], showing a very large and fast increase in RIA, exceeding 1000 dB/km at doses as low as a few kGy(SiO_2), before decreasing during irradiation to lower RIA values at higher doses (recovery phase will be discussed for the final paper). The main probable explanation relies on the contribution of metastable point defects absorbing in the IR domain (probably variant of self-trapped holes, STHs), that are very efficiently generated at the beginning of the irradiation by conversion of pre-existing precursor centers. At longer times (doses), their contribution decreases as most of the defects have been generated and successively bleached by thermal- or photo-assisted processes. This explains that at doses on the order of 1 MGy and above, the RIA stabilizes around 100 dB/km for the ZLL and PA80 fibers, while it remains significantly higher up to 650 dB/km for the Z+150 ULL fiber.

3.2 Spectrum with IR and VIS

To better understand the basic mechanisms at stake, spectral RIA measurements have been performed from the visible to the near-IR regions. As an example, Figure 2 compares the near IR-RIA spectra of the 3 optical fibers at two TIDs, the first corresponding to the RIA peak at a TID of a few kGy and the second one at 2 MGy dose. While a comprehensive analysis will be provided in the final paper, a preliminary qualitative discussion can be made. The transient high RIA peak is explained by the appearance of two IR absorption bands in the three optical fibers, similar to those reported for the Vascade optical fibers and tentatively attributed to STHs [3]. Visible part of the transmission domain will be discussed at the symposium.

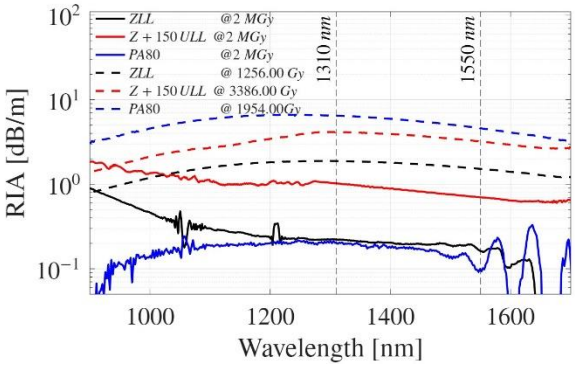

Figure 2: RIA spectra: solid lines represent the results at 2 MGy and dashed ones those at their RIA peak values.

4 CONCLUSION

These AVD-made ULL pure silica core optical fibers are extremely radiation sensitive despite their composition. For the conference, the RIA spectra will be decomposed as the sum of Gaussian absorption bands associated with point defects to better understand the origin of their response.

REFERENCES

[1] S. E. Industries, *T G*, no. 96, 2023.

[2] L. Weninger, et al, *Radiation*, vol. 4, no. 2, pp. 167–182, May 2024, doi: 10.3390/radiation4020013.

[3] A. Morana *et al.*" *Sensors*, vol. 20, no. 24, p. 7254, Dec. 2020, doi: 10.3390/s20247254.

[4] J. Dhliwayo, "OVD_LowLoss_fiber." [Online]. Available:https://www.corning.com/media/worldwide/coc/documents/Fiber/articles/R4030.pdf

[5] "Corning Vascade Optical Fibers", [Online]. Available:https://www.tlc.unipr.it/cucinotta/cfa/datasheet_Vascade.pdf

[6] "Transatlantic and Transpacific Submarine Optical Fibers." Accessed: Apr. 28, 2025. [Online]. Available: https://sumitomoelectric.com/id/project/v06/05

Radiation-Induced Defects and Structural Modifications in SiO_2: Insights from Electron Irradiation

O. Cavani[*], A. Courpron[*], N. Blondeau[*], R. Grasset[*], A. Alessi[*,**]

[*]Laboratoire des solides irradiés, CEA/DRF/IRAMIS, CNRS, École Polytechnique, Institut Polytechnique de Paris, F-91128, Palaiseau, France
[**] Department of Physics and Chemistry Emilio Segrè, University of Palermo, Via Archirafi 36, 90123 Palermo, Italy

ABSTRACT

This paper illustrates the irradiation capabilities of the electron accelerator Sirius, located at the Laboratoire des Solides Irradiés (UMR 7642 CEA – CNRS – Ecole polytechnique) and a member of the EMIR&A network (https://emira.in2p3.fr/). Its design allows for the selection of the electron beam energy in the range of 150 keV to 2.5 MeV and the current impacting the irradiated surface from a few nA up to 30 µA. The accelerator is equipped with different irradiation setups that enable the control of the irradiation temperature from 20 K to 1100K and atmosphere. We also report some of the possible in-situ and post-irradiation measurements that can be recorded and some privies investigation on silica based materials.

PACS Keywords: electron irradiation, point defects, structural modification, TID and DDD.

1 INTRODUCTION

Traveling through a material, electrons interact in various ways with matter. Most of their energy is lost via soft collisions and hard collisions (with atoms or with single electrons, respectively), contributing to the total ionizing dose (TID). Electrons can also collide with nuclei, displacing atoms and creating vacancies and interstitials, a process known as non-ionizing energy loss (NIEL), which leads to displacement damage dose (DDD). Protons and heavy particles can cause similar effects, often initiating collision cascades. In contrast with protons and heavy particles, which tend to create cascades, electrons, due to their low mass, tend to produce isolated defects and penetrate deeper into materials, affecting a larger volume. For such reasons electrons irradiation represents an important tool to study radiation effects in any kind of materials including silica.

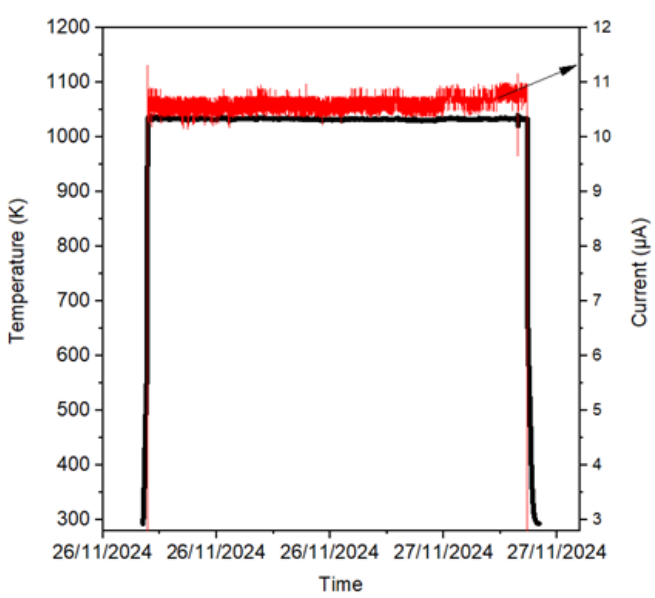

Figure 1: Temperature (measured by a thermocouple close to the sample) and current measured using the irradiation cell as Faraday cup during an irradiation run of about 1 day.

2 EXPERIMENTAL CAPABILITIES

As with many materials, radiation effects in silica depend on dose rate and irradiation temperature. As a consequence, SIRIUS is equipped with different irradiation cells which allow the possibility to explore a large range of conditions. The irradiation temperature range goes from 20 K up to 1100 K allowing to test very extreme conditions that can be encountered in space or in the core of nuclear power plants. Similarly, different radiation environments are characterized by different dose rates. By tuning the beam current and the irradiated surface, irradiations can be performed with dose rates in silica going from about 2 Gy/s up to 20 kGy/s. Figure 1 reports an example of irradiation at about 1000 K with a

current of about 10 µA, which corresponds to a dose rate of about 15 kGy/s.

Furthermore, it is well known that radiation effects like RIA (radiation induced attenuation) and RIE (radiation induced emission) can be metastable so they can disappear completely or in part after the end of the irradiation. As a consequence, the facility is equipped with online or in-situ measurement setups. In the field of silica investigation, it is worth noting the on-line optical absorption and the cathode-luminescence setups.

3 EXAMPLES FROM THE PAST

The possibility of performing irradiation at high dose rates allows the study of high doses at which silica undergoes not only defect generation but also structural modifications that affect the density. This topic is of particular interest as fiber Bragg gratings are used in different nuclear environments, and the radiation-induced modifications of the silica matrix can impact the initial periodic sequence of normal and densified silica and consequently the periodical refractive index pattern. Recent investigations have highlighted a complex scenario regarding radiation-induced density variations [1,2]. One of the most important results was that, at high doses, the densified silica (such as that obtained during the fs-writing procedure) can exhibit a decrease in density. Since the spectroscopic features of optical or paramagnetic signals related to defects depend on the surrounding matrix, a detailed investigation of absorption, emission or electron paramagnetic resonance (EPR) spectra provides access not only to the concentration of defects, but also to their local environment. EPR experiments on samples irradiated at high doses have given new insight on the connection between defect generation and densification [3] or improved the understanding of the structure of silica nanoparticles [4]. In this latter case the data supported the core-shell description of these nanosystems. In fact, by using the E'Si hyperfine signal it was inferred that the core of the nanoparticles has the same structure regardless of the nanoparticles sizes and that this structure is slightly denser than that of the bulk silica [4].

Considering the range of beam energies generated by SIRIUS, the accelerator is a very useful tool to distinguish TID effects from DDD ones. In fact, for many materials such as silica in the range 0.5-2.5 MeV the stopping power depends on the beam energy in a less pronounced way than NIEL does, and however the two dependencies are distinguishable.

This peculiarity has been exploited to study wall collapse under irradiation in mesoporous silica that could be used for immobilization of radioactive waste [5].

Online optical absorption measurements have been performed at LSI since 2003 (when the Van de Graaff accelerator was in use before SIRIUS). Such experiments performed on natural and synthetic silica allowed the detection of the transient nature of both intrinsic and extrinsic centers [6].

The metastable nature of many absorption bands has subsequently been investigated in optical fibers [7] and pushed to a recent improvement of the set-up of the facility that today allows to perform experiments in the range 400-1600 nm.

Cathodoluminescence (CL) experiments are, by definition, online investigations of the radiation effects, in fact, the electron beam is both the source of irradiation and the excitation of the emission. Both processes are related to the electron-hole generation. During a CL experiment, it is possible to study the kinetics of formation or conversion of emitting defects as has been reported for O_2 molecules in silica [8]. Since emission spectra also depend on the surrounding matrix, the spectral analysis allows to obtain not only the signal dose dependence (kinetics of the defects) but also to infer on the structure of the environment of the emitting defects.

REFERENCES

[1] N. Ollier et al., Sci Rep. 9, 1227, 2019.
[2] N. Shchedrina et al., Nanomaterials , 14, 1909, 2024.
[3] G. Buscarino et al., Phys Rev B 80, 094202, 2009.
[4] A. Alessi et al., J. non-Cryst. Solids 423-424, 41, 2015
[5] J. Lin et al., Materialia 32, 101903, 2023.
[6] S. Agnello et al, J. non-Cryst. Solids 322, 84, 2003.
[7] S. Girard et al., Reviews in Physics 4, 100032, 2019.
[8] N. Ollier et al., Sci Rep. 13, 13657, 2023.

The NanoSaintÉtienne platform for surface structuration and functionalization

Arnaud Meyer*, Jean-Yves Michalon*, Arnaud Valour*, Stéphanie Reynaud*, Frédéric Celle*, Nicolas Aimé*, Éric Geai*

*Laboratoire Hubert Curien, Université Jean Monnet Saint-Étienne, CNRS, IOGS, UMR 5516
42000 Saint-Étienne, France

The NanoSaintÉtienne platform is a research infrastructure located in Laboratoire Hubert Curien (Saint-Étienne, France), belonging to the national Renatech+ CNRS network, and dedicated to surface micro/nano structuring and functionalization. It offers equipment for lithography, thin film deposition and characterization of functional layers.

Located on the Manufacture campus of Université Jean Monnet Saint-Étienne, this 600 m² platform is divided in three parts: a 200 m², class 1000 cleanroom (including a 65 m², class 100 room), a room dedicated to thin film deposition through physical processes, and a characterization room.

Deposition of solutions in liquid phase on substrates (cleaned using the ultrasound tanks of the wet bench facility located inside the cleanroom) can be performed using several processes: spin coating from 1 inch to 22 inches, dip coating up to 10 inches, or micro-objects deposition through Langmuir-Blodgett process up to 4 inches. Several oven and hot plates are also available to perform thermal treatment at every step of the process.

Surface structuration is then performed using different means of UV lithography. Two laser interference lithography benches (with three available lasers at 442 nm, 355 nm and 405 nm) can project sine patterns with a period ranging from 300 nm to 1 µm on surfaces up to 4 inches. Two direct-write lithography devices can also be used to produce arbitrary patterns with a resolution down to 1 µm, either using a UV laser with a translation stage (Kloé Dilase 750, dimensions up to 400 × 400 mm²) or a 1000 × 1000 px micro-reflector matrix (DMO MicroWriter ML3, dimensions up to 149 × 149 mm²). Finally, a UV mask aligner (Kloé UV-KUB-3, mask size up to 4 inches) is also available, along with two UV irradiators, for contact lithography or direct irradiation.

Metallic film depositions are performed by four thin film deposition devices: an evaporator and three magnetron sputtering coaters, enabling deposition of a variety of metals such as gold, chromium, aluminum, copper and cobalt. A rapid thermal annealing (RTA) oven also enables surface heating to high temperatures (~1200 °C) in a few seconds, with the ability to work under different gas atmospheres (N_2, NH_3, O_2, Ar), enabling for instance nitruration processes on dielectric substrates.

Produced samples can finally be characterized in-situ using an atomic force microscope (AFM) enabling mapping of the surface topography on the nanometer scale, a profilometer for measuring thin film thickness, and a 4 point measurement for determining conductivity/resistivity of thin films. A scanning electron microscope (SEM) and Raman spectroscope are also available on site.

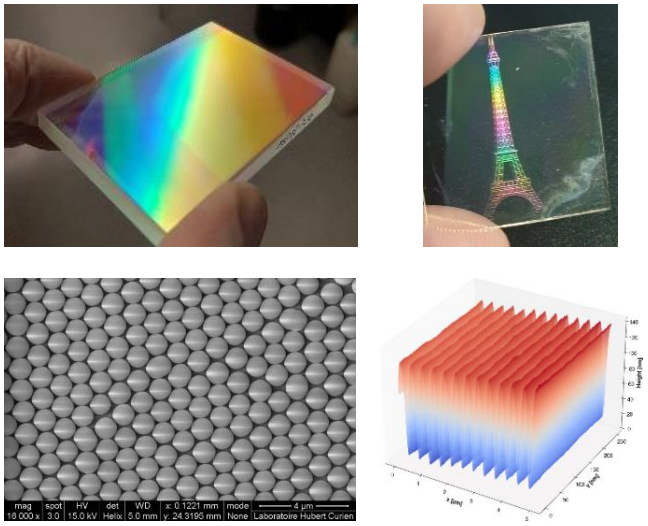

Figure 1: Examples of structures realized on the NanoSaintÉtienne platform. From left to right, top to bottom: 1D grating using laser interference lithography, pattern obtained by direct-write lithography, microball layer obtained by Langmuir-Blodgett process, AFM topography of a 1D diffraction grating.

X-ray Radiation Induced Luminescence of a Medium-OH Pure Silica Core Multimode Optical Fiber: Potential and Limitations for Dosimetry Applications

L. Breccia[*], R. Pecorella[**], L. Weninger[**], M. Ferrari[**], A. Morana[**], F. Fricano[**], S. Bortolussi[*] and S. Girard[**†]

[*]Dipartimento di Fisica – Alessandro Volta, Università degli Studi di Pavia, 27100, Pavia, Italy
[**] Université Jean Monnet Saint-Etienne, Laboratoire Hubert Curien UMR 5516, F-42023, Saint-Etienne
[†] Institut Universitaire de France (IUF) 75005 Paris, France.

ABSTRACT

This work compares the Radiation Induced Luminescence (RIL) of two multimode optical fibers (OF) under X-rays. The first one is Ce-doped and is a reference scintillating OF for dosimetry. The second one is a pure-silica-core (PSC), F-doped cladding OF intended for visible signal transmission in harsh environments. The collected results show that the medium-OH PSC OF exhibits promising response for RIL-based dosimetry showing linear sensitivity as a function of the length up to about 4m and smaller Bright Burn and afterglow effects than the reference Ce-doped OF. On the other side, if used as transport fiber in combination with the Ce-doped OF, its RIL contribution could be considered.

PACS Keywords: dosimetry, optical fibers, silica, X-rays, RIL, dose rate

1 INTRODUCTION

Ionizing radiation can induce point defects in the Optical Fibers (OF) microscopic structure. These defects impact the OF macroscopic properties via three main phenomena: Radiation Induced Attenuation (RIA), Radiation Induced Refractive Index Change (RIRIC) and Radiation Induced Luminescence (RIL). RIA corresponds to the increase of optical losses adding to the intrinsic attenuation. RIRIC is a change in the refractive index, influenced by compaction and RIA. RIL consists in the emission of luminescence light when the fiber is exposed to radiation. Both RIA and RIL are commonly exploited to design OF-based dosimeters.

At the microscopic scale, ionizing radiation leads to the production of electron-hole pairs in the silica matrix, that can be either trapped in defects or in recombination centers. Among these, Ce^{3+} can act as a recombination center by trapping electrons in their excited state. This is accompanied by a luminescent emission peaking around 500 nm. [1] Recombination centers and radiation induced defects can be competitive in trapping electrons. This leads to parasitic phenomena degrading the performances of RIL dosimeters such as the Bright Burn Effect (BBE), associated to an increase of RIL with dose, and afterglow, which corresponds to the residual RIL signal observed after the irradiation stop.

The aim of this work is to evaluate the use of Medium-OH (M-OH) PSC OF for RIL-based dosimetry in comparison to traditional Ce-doped fibers. This work also highlights some limitations in using such fibers as transport fibers in Ce-doped fiber architectures.

2 MATERIALS AND METHODS

2.1 Tested Fibers

Ce-doped OFs strongly luminesce around 500 nm under exposure, for this reason they are among the most investigated OF for dose rate sensors. [2][3]. Nevertheless, their use as dosimeters might be affected by RIA, limiting the usable sample length. Medium-OH (M-OH) is a multimode OF with PSC, F-doped cladding and polyimide coating, manufactured by Exail having an intermediate concentration (27 ppm) of hydroxyl groups. Thanks to their low RIA in the visible, they have been recently used as transport fibers for RIL experiments. [4] Table 1 reports information on these fibers.

Sample	Core Ø	Cladding Ø	Coating Ø
M-OH	112 µm	125 µm	150 µm
Ce-doped	100 µm (50µm doped with Ce)	126 µm	242 µm

Table 1: size of the tested fibers.

2.2 Experimental Setup

The selected OF were irradiated using the X-ray LabHX facility at the Laboratoire Hubert Curien (Saint Etienne, France), using a W target and operating voltage of 100 kV. The setup to measure RIL consists of an OF sample, placed in the irradiation chamber, and connected via a transport fiber to a photomultiplier tube, placed out of the irradiation chamber. In the first campaign, RIL measurements have been performed on a 2 cm long Ce-doped sample and on a

391.5 cm long M-OH sample (M-OH 4m), arranged in a monolayer spool (2.5 cm internal radius). A second measurement was realized reducing the M-OH sample length to 290.5 cm (M-OH 3m). Dose rate was varied between 0.3 and 179 mGy[SiO_2]/s, by tuning the irradiator current. For each current value, the irradiator was kept ON for 2 minutes, followed by 3 minutes OFF. A second campaign targeted the sensitivity of the M-OH as a function of the spool length, that was varied from 59 cm to 190.5 cm, at fixed dose rate of 89.5 mGy[SiO_2]/s. The transport fiber (M-OH OF in all the experiments) was shielded to limit its radiation exposure.

3 RESULTS AND DISCUSSION

Fig. 1 shows the RIL kinetics (in counts per second) for the Ce-doped and the M-OH 4m samples in the first campaign. Each step corresponds to a dose rate value. The reduced afterglow observed in the M-OH fiber represents a key benefit, especially in scenarios where fast signal recovery or minimal background light is critical, in contrast to the more persistent emission seen in the Ce-doped OF.

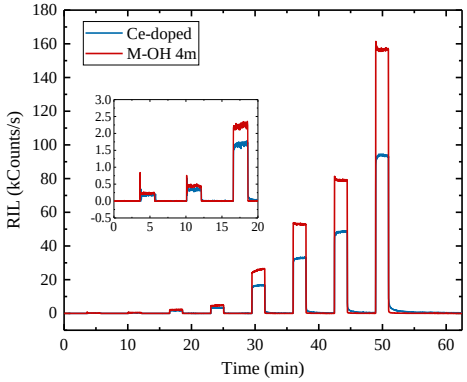

Figure 1: RIL kinetics for the Ce-doped and the 391.5 cm M-OH PSC OF samples. The inset shows a zoom of the three lowest investigated dose rates.

Fig. 2 represents the RIL as function of the dose rate for the first campaign. Both M-OH samples exhibit higher RIL than the 2-cm long Ce-doped one. Fig. 3 reports the length dependence of M-OH OF sensitivity being calculated through the results as shown in Fig. 2. It is then expressed in Counts/s for a given dose rate, as a function of the sample length. In the explored irradiation conditions, sensitivity evolution of M-OH increases linearly with sample length (fit parameters: slope=2.29 Counts mGy^{-1} cm^{-1}, R^2 = 0.998). For comparison, the Ce-doped fiber has a higher sensitivity of 526.2 Counts/mGy. M-OH OF can outperform the 2-cm Ce-doped reference for a sample length exceeding 230 cm.

4 CONCLUSIONS

The collected results suggest that M-OH PSC OF is a promising candidate for RIL-based dosimetry, exhibiting for long lengths a high radiation sensitivity and limited BBE and afterglow, in comparison to the Ce-doped OF. The observed linearity of the M-OH sensitivity with fiber length suggests that the range of observable dose rates can be largely tuned by varying the spool length. Further research is needed to deepen the understanding of the observed behavior and to verify it in different irradiation conditions.

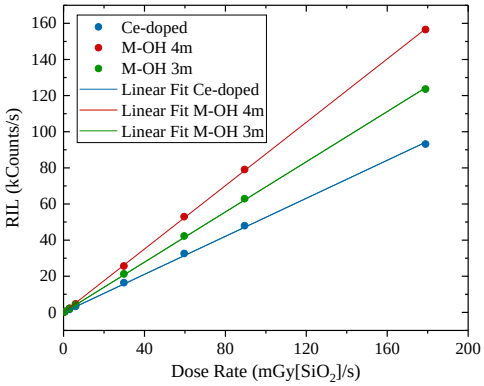

Figure 2: RIL as function of the dose rate for the Ce-doped, M-OH 3m and M-OH 4m samples.

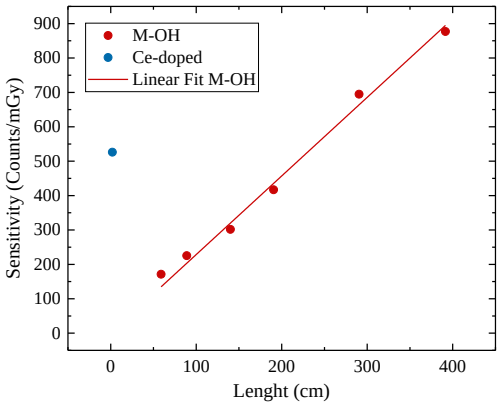

Figure 3: Sensitivity of the two investigated optical fibers as a function of the length.

REFERENCES

[1] S. Girard et al., Overview of radiation induced point defects in silica-based optical fibers. *Reviews in Physics*, 2019, 4: 100032.

[2] F. Fricano, PhD Thesis, Real-time dosimetry: feasibility and optimization of radioluminescent optical fiber sensors, University Jean Monnet, Doctoral School N° 488, 2025.

[3] F. Fricano et al., Reproducibility of dose rate measurements with radioluminescent nitrogen-doped optical fibers. *IEEE Transactions on Nuclear Science*, 2023, 70.8: 1925-1932.

[4] C. Campanella et al., Radiation effects on pure-silica multimode optical fibers in the visible and near-infrared domains: Influence of OH groups. *Applied Sciences*, 2021, 11.7: 2991.

X-ray Radiation-induced Changes on Er^{3+} Ions Cross Sections

Alberto Facchini[1,2], Adriana Morana[1], Luciano Mescia[2], Youcef Ouerdane[1], Emmanuel Marin[1], Aziz Boukenter[1], Thierry Robin[3], Sylvain Girard[1,4]

[1]Université Jean Monnet Saint-Etienne, Laboratoire Hubert Curien, Saint-Etienne, France
[2]Politecnico Di Bari, Bari, Italy
[3]Exail, Lannion, France
[4]Institut Universitaire de France (IUF), Paris, France

ABSTRACT

This work aims to analyze the impact of ionizing radiation on the absorption and emission cross sections around 1550 nm of an erbium-doped aluminosilicate fiber. The study also compares two approaches to calculate the emission and absorption cross sections.

PACS Keywords: erbium, radiation effects, silica, cutback, optical fibers

1 INTRODUCTION

Since the 1990s, Rare Earth Doped Fiber Amplifiers (REDFAs) have revolutionized the world of telecommunications, being used as boosters, pre-amplifiers and in-line amplifiers in communication networks [1]. Given the good performance of these devices in terms of gain, available power and low noise, they have also found application in the space mission context. Indeed, over the past 20 years, numerous investments have been made by private companies and national space agencies to create new satellite constellations [2]. In this development process, fiber-optic systems, including REDFAs, have a key role by providing mass reduction, high transmission rates, secure connections in intra-satellite, inter-satellite and spacecraft-to-ground communication systems [2].

These devices are typically based on Rare Earth Doped Fibers (REDFs) doped with Er^{3+}, Yb^{3+} ions or a combination of both. However, the RE-based systems also have limitations in such harsh environments, because of ionizing radiations (protons, electrons, etc..) present in space, which degrade the gain of the REDFs [2]. The main effect of ionizing radiation on REDFs is radiation induced attenuation (RIA) caused by the generation of point defects in the host glass matrix. In REDFs, those point defects are mainly related to the presence of co-dopants such as Al or P, added to the glass matrix to facilitate the incorporation of RE ions and to prevent the formation of clusters [1]. To improve the tolerance of REDFs and limit RIA impact on the gain of REDFA, various approaches have been proposed, including codoping the REDF core with Ce^{3+} ions and/or pre-loading it with H_2 [2]. Ionizing radiation can also induce changes on fiber spectroscopic parameters including cross sections and lifetimes [3].

Cross sections quantify the ability of ions to absorb and emit light. The cross section of a particular transition between two states of an ion represents the probability that that transition will occur with the simultaneous emission or absorption of light [4]. The goal of this study is to compare the Er^{3+} emission (Em) and optical absorption (OA) cross sections obtained by two approaches, one starting from the measured absorption spectrum and the other starting from the measured photoluminescence spectrum. In this study, X-rays irradiations up to a Total Ionizing Dose (TID) of 3 kGy (SiO_2). We focus on the cross sections in the spectral region that characterizes the signal wavelength in REDFAs, which is around 1550 nm.

2 MATERIAL AND METHODS

In order to estimate Er^{3+} OA and Em cross sections, two approaches have been applied. The first, approach 1 (OA→Em), provides the OA cross section from the experimental measurement of the absorption spectrum of the active fiber (1), via cutback technique [1, 3], and then calculating the Em cross section through McCumber Theory (2). Below mathematical details are shown [3]:

$$\sigma_{abs} = \frac{\alpha^{Er}(\lambda)}{10\log(e) N_{Er} \Gamma(\lambda)} \quad (1)$$

$$\sigma_{em} = \sigma_{abs} e^{-(h\upsilon - E)/kT} \quad (2)$$

λ is the wavelength, α^{Er} is the Er^{3+} absorption spectrum, measured in dB/m, N_{Er} is the Er^{3+} ions concentration, $\Gamma(\lambda)$ is the overlapping factor, υ is the frequency, E is the energy difference between the lower energy level of the manifold $^4I_{13/2}$ and the lower energy level of the manifold $^4I_{15/2}$, T is the temperature, κ and h are the Boltzmann and Planck constants, respectively.

The second approach, approach 2 (Em→OA), in based on the calculation of the Em cross section using the Fuchtbauer-Ladenburg relation (3) and the measured luminescence, then applying McCumber theory (the inverse formula of (2)) for calculating OA cross section. Below the Fuchtbauer-Ladenburg relation is given [5]:

$$\sigma_{em} = \frac{\lambda^5}{8\pi c \tau n^2} \frac{I(\lambda)}{\int \lambda I(\lambda) d\lambda} \quad (3)$$

where c is the light speed in the medium, τ is the radiative lifetime of the $^4I_{13/2}$ energy level, n is the refractive index of

the medium and $I(\lambda)$ is the photoluminescence intensity spectrum.

The studied sample is an Erbium Doped aluminosilicate Fiber (EDF) with an Er^{3+} ions concentration of 0.48×10^{25} ions/m^3 and with ~ 4 dB/m of absorption losses at 1530 nm.

For Approach 2, the photoluminescence spectrum is obtained by exciting the 50 cm long EDF sample with a 20 mW signal at 980 nm, generated by a 1999CHP pump diode by 3S Photonics, and measured through an IR spectrometer (or an Optical Spectrum Analyzer (OSA)). Passive irradiations were performed at MOPERIX facility of Laboratoire Hubert Curien using a dose rate of 0.28 Gy(SiO_2)/s, achieving a TID of 3 kGy(SiO_2).

3 RESULTS AND DISCUSSION

Fig.1 shows the results obtained for the OA cross section.

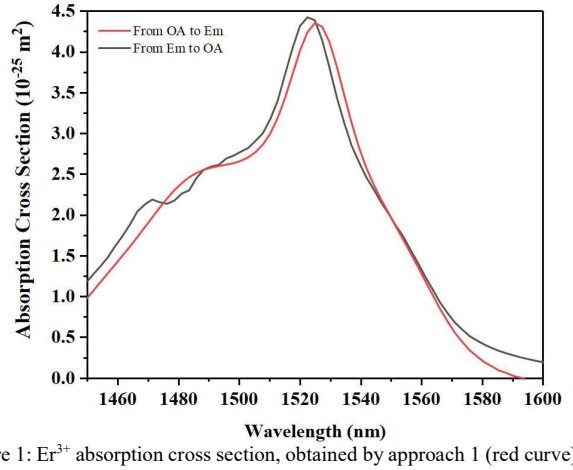

Figure 1: Er^{3+} absorption cross section, obtained by approach 1 (red curve) and approach 2 (black curve).

The two approaches show good agreement over the entire spectral range considered, with an almost perfect agreement at the 1550 nm wavelength, the signal wavelength, with a value of ~ 1.88×10^{-25} m^2. The relative error remains quite low for the entire spectral range, increasing for wavelengths higher than 1570 nm.

Fig.2 shows the obtained Em cross section with the two approaches. The approach 1 produced an Em cross section of ~ 2.76×10^{-25} m^2. The two approaches show good results with a deviation between the two curves of ~ 7% at 1550 nm. In Fig. 2 there is also an insight showing that from 1450 nm to 1570 nm the maximum relative error is ~ 20 %, while for longer wavelengths this increases significantly.

The approach 2 can be interesting, as obtaining a photoluminescence spectrum is easier than obtaining an absorption spectrum through the cutback technique, which requires several acquisitions of the transmitted spectrum of the EDF, using a white light source, at different lengths, making it complex to reuse the fiber for other experiments.

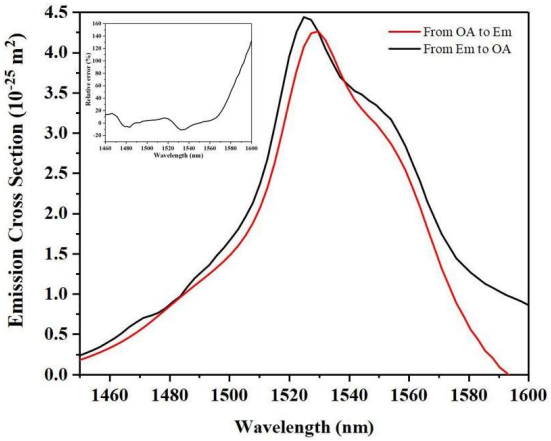

Figure 2: Er^{3+} emission cross section, obtained by approach 1 (red curve) and approach 2 (black curve).

Fig.3 shows the OA and Em cross sections for pristine and irradiated EDFs at 3kGy, obtained by approach 1.

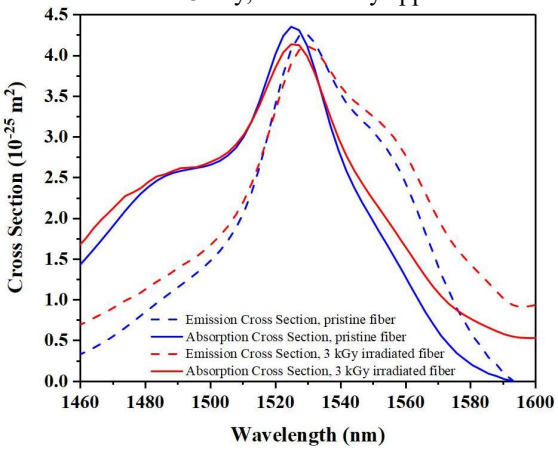

Figure 3: Er^{3+} Em cross sections for pristine fiber (blue dashed curve) and for 3 kGy irradiated fiber (red dashed curve), and of Er^{3+} OA cross sections for pristine fiber (blue solid curve) and for 3 kGy irradiated fiber (red solid curve)

The OA and Em cross sections for pristine EDF and for 3 kGy irradiated EDF have similar peak values around 1530 nm. However, it is necessary to point out that at 1550 nm the irradiated EDFs have higher cross sections, consistent with (3), which shows that as the lifetime decreases the cross sections at 1550 nm increase [5].

For the symposium, this type of study will also be conducted on other EDFs and irradiating the samples at different absorbed doses.

REFERENCES

[1] Desurvire, E., & Zervas, M. N. (1995). Erbium-doped fiber amplifiers: principles and applications.
[2] S. Girard et al. Journal of Optics (2018) 20.
[3] A. Ladaci et al. Journal of Luminescence (2018) 195, 402-407.
[4] P. C. Becker et al. Erbium-doped fiber amplifiers: fundamentals and technology. Elsevier (1999) 234-251.
[5] B. Aull et al. IEEE Journal of Quantum Electronics (1982), 18 (5).

PETRA: an Experimental Platform for X-ray Radiation Testing of Materials and Components

Sylvain Girard[1,2], Adriana Morana[1], Matteo Ferrari[1], Emmanuel Marin[1], Hugo Boiron[2], Arnaud Meyer[1], Maxime Darnon[1], Youcef Ouerdane[1], Aziz Boukenter[1]

[1]Laboratoire Hubert Curien, UJM, UMR CNRS 5516, Saint-Etienne, France
[2]Institut Universitaire de France, Paris, France
[3]Exail, Lannion, France

ABSTRACT

PETRA (Experimental Platform for Radiation Tests) brings together LabHC's irradiation and radiation testing equipment. It is today built around three X-ray machines that enable *in situ* testing of materials, components and systems, across a wide temperature range (-120 to +400 °C) and under controlled atmospheric conditions.

PACS Keywords: Optical Fiber, Radiation Induced Attenuation, Temperature

1 INTRODUCTION

In space and other radiation-rich environments, various technologies such as microelectronics, photonics and functionalized materials, are exposed to radiation that can significantly alter their performance and reliability. The most critical radiation effects include Displacement Damage Dose (DDD), Total Ionizing Dose (TID), and Single Event Effects (SEE). Understanding these phenomena remains crucial to estimate their radiation vulnerability and when needed implement radiation hardening strategies. DDD occurs when energetic particles, such as protons or neutrons, displace atoms from their lattice sites within a material. This displacement creates defects that alter the material's structural and electronic properties. TID results from the cumulative effect of ionizing radiation, primarily impacting insulating and semiconductor materials. Ionizing particles generate electron-hole pairs that may become trapped by radiation induced point defects, causing threshold voltage shifts in microelectronics or increased radiation induced attenuation in glass-based photonic components. In materials science, TID results in chemical and structural changes compromising durability or functionality, particularly in polymers and composite materials. SEE are transient perturbations caused by a single ionizing particle striking a sensitive region of a device. In microelectronics or optoelectronic devices, SEEs can lead to bit flips, latch-up, or permanent damage. Among these effects, TID is particularly relevant when assessing the long-term reliability of electronic, photonic, and material components exposed to radiations. X-ray machines, such as the three ones at the basis of the PETRA platform are well-adapted for studying TID because they offer a low-cost, practical and efficient way to deliver controlled ionizing radiation doses in laboratory settings. This capability makes them indispensable for accelerated testing and reliability assessment, particularly for fundamental studies on new technologies or systematic studies needing long and a large number or irradiation runs. These facilities can also be optimized to combine various environmental constraints in addition to the radiation ones such as temperature of irradiation or ambient atmosphere.

2 PETRA X-RAY MACHINES

Three irradiators are today available at LabHC and accessible to the research community through collaboration: MOPERIX, LABHX, and IDEFIX, illustrated in Figure 1.

Figure 1. From left to right: MOPERIX, LABHX, and IDEFIX

The three facilities share the same operating principle [1]: a tungsten (W) target inclined at an angle of 30° with respect to the incident electron beam, a beryllium window 4 mm thick for IDEFIX and LABHX, and 2 mm thick for MOPERIX. The X-ray tubes are housed in lead enclosures sufficiently thick to ensure safe radiation levels, even during operations at maximum voltage and current, allowing access to the irradiation rooms, that remains public spaces without any restrictions. The enclosures are equipped with openings dedicated to the passage of cables and optical fibers, especially designed to minimize radiation leakage. Those facilities are then well designed to perform *in situ*

characterization of the radiation effects on materials and devices, allowing accessing their associated kinetics.

The emitted photon energy spectrum can be tuned by changing the tube operating voltage or by adding some filtering materials between the X-ray tube and the sample under test [2]. As an example, Fig. 2 [1] illustrates the X-ray spectra calculated using the SpekPy software [3] for different operating voltages and in absence of additional shielding.

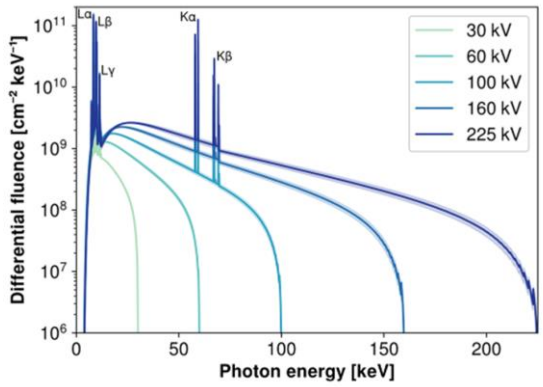

Figure 2. Simulated X-ray energy spectra of LabHX for 5 different source voltages. Main characteristic X-ray emission lines of W are also given [1].

Table 1 gives the main ranges of operation for the three facilities in terms of dose rate and without any shielding. With appropriate shielding, dose rates as low than 1 µGy/s are possible [2]. Before each experiment, a dose rate mapping is performed using ionization chambers, allowing the entire sample surface to be covered. These calibrated dosimetry tools are complemented by Monte Carlo simulation codes, such as Geant4 and PHITS allowing to calculate precisely the dose deposited in the sensitive volume of the material, considering its nature and geometry.

Table 1: Main characteristics of PETRA X-ray machines

	MOPERIX	LABHX	IDEFIX
Max. Operating Voltage	160 kV	230 kV	160 kV
Minimum dose rate (DR)	0.5 mGy(SiO_2)/s	0.5 mGy(SiO_2)/s	0.5 mGy(SiO_2)/s
Maximum DR	60 Gy/s	60 Gy/s	100 Gy/s
Beam size at Min DR	>20 cm	>20 cm	>20 cm
Beam size at Max DR	>2 cm	>2 cm	>2 cm

Of course, one limitation of this class of irradiators with respect to gamma sources is the more limited penetration depth of the X-rays having a mean energy of about 40 keV for a 100 kV operating voltage. This limitation could be reduced by adding filters hardening the energy spectrum by absorbing the low energy photons and enhancing the dose homogeneity within the sample volume, as studied e.g. for the Radiophotoluminescence (RPL) glass dosimeters [4]. For the irradiation of thin materials, such as optical fibers, to ensure good homogeneity of the deposited dose with our X-ray photons, the optical fiber samples are prepared in a single-layer spiral, as illustrated in Fig.3.

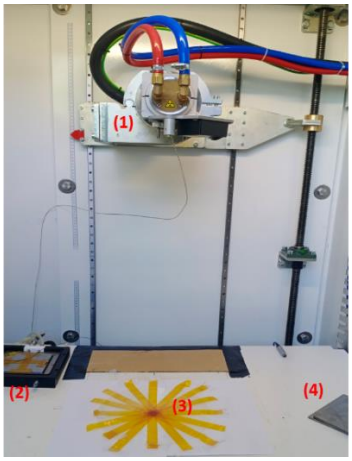

Figure 3. illustration of a radiation test on optical fibers at IDEFIX facility, at room temperature © M. Roche. (1) X-ray tube (2) temperature-controlled plate (3) optical fiber spiral coil (4) Aluminum shielding for transport fibers.

Each irradiator can be equipped with temperature-controlled plates capable of cooling or heating the sample under test. Additionally, the ambient atmosphere can be controlled through gas injection. The three cooling plates, with dimensions ranging from 10×10 cm² to 12×12 cm², use a liquid nitrogen circuit to achieve precise temperature control (±0.1°C) from room temperature down to -40°C for long irradiations, and even down to -120°C for short irradiations. Larger plates, with sizes up to 30×30 cm², can heat samples to temperatures as high as 300°C during long irradiations or up to 400°C for shorter irradiation periods. This setup enables the investigation of combined radiation and temperature effects on the properties of materials and components.

3 CONCLUSION

The main characteristics of the PETRA platform tools are briefly presented. At the conference, examples of results acquired thanks to those facilities will be presented, for optical fiber and fiber sensors, optoelectronics components (LEDs, Silicon Photonics), and materials (RPL, polymers, 3D printing materials).

REFERENCES

[1] Meyer, A.; Lambert, D.; Morana, A.; Paillet, P.; Boukenter, A.; Girard, S. Simulation and Optimization of Optical Fiber Irradiation with X-rays at Different Energies. Radiation 2023, 3, 58–74.

[2] L. Weninger, et al., Combined theoretical and experimental evaluation of the energy dependence of the radioluminescence phenomenon in Ce-doped optical fibers, submitted to SiO2 2025 Conference, 2025

[3] "SpekPy Web." [Online]. Available: https://spekpy.smile.ki.se/

[4] M. Ferrari et al., "Characterization of Radiophotoluminescence Dosimeters Under X-Ray Irradiation at High Doses," in IEEE Transactions on Nuclear Science, vol. 71, no. 8, pp. 1821-1828, Aug. 2024.

First On-Line Optical Glasses and crystals Measurements in a Nuclear Research Reactor for a Future Confocal Chromatic Sensor

Marion Agoyan[*], Guy Cheymol[**], Ayoub Ladaci[**], Sylvain Girard[*], Aziz Boukenter[*], Christophe Destouches[***], Florence Martin[***], Nicolas Thiollay[***]

[*]Université Jean Monnet, Laboratoire Hubert Curien
Saint-Etienne, France
[**]CEA/DES/ISAS/DRMP/LISL
Saclay, France
[***] CEA/DES/IRESNE/DER
Cadarache, France

ABSTRACT

To measure fuel rod swelling in a core research reactor, a sensor is designed. This optical sensor must withstand the harsh environment of a Pressurized Water Reactor. Candidate glasses were irradiated to assess radiation effect. Suprasil was selected for the sensor despite its limited chromatic properties, due to the strong radiation induced attenuation of other more chromatic glasses. Online measurements in a reactor core were successfully conducted for the first time. Post-mortem measurements were also performed.

Keywords: nuclear application, online measurements, high neutrons and gamma irradiation, optical glasses, crystals, radiation induced attenuation, radiation induced refractive index change, compaction

1 CONFOCAL CHROMATIC SENSOR FOR A FUTURE RESEARCH REACTOR

The future Jules Horowitz nuclear research reactor is currently under construction in Cadarache, France. Its core will be able to reach a thermal power of 100 MWth, and numerous locations will be able to accommodate up to 20 experiments simultaneously under a variety of irradiation conditions. Test devices will be placed within the core or at its periphery, for material and fuel tests respectively. These devices are either capsule-type or loop-type, enabling irradiation parameters to be adjusted in real time. One example is the ADELINE loop (Advanced Device for Experimenting up to Limits Nuclear fuel Element), which will be dedicated to power ramp tests. During these power transients, the fuel rod is subjected to numerous stresses, including expansion. A sensor is being developed to quantify this swelling. It is an optical sensor enabling non-contact measurement: the confocal chromatic sensor [1]. The sensor will be positioned along the rod, on the wall of the test device, and the measurement will be carried out transversely. The optics making up the sensor will be subjected to a severe environment (Pressurized Water Reactor type).

It is now well known that when glasses and optical fibers are subjected to high doses and dose rates, high neutron fluxes and fluences, physical phenomena need to be taken into account [2], [3]: such as radiation-induced attenuation, radiation-induced refractive index changes, etc. It is therefore necessary to expose candidate glasses for the chromatic confocal sensor to an environment similar to that of its final application. This will enable us to refine the choice of lenses (removing those showing high RIA) and quantify the change in index and length of others. Indeed, in the state of the art, few data are available at the fluences involved [4], [5], and the data mainly concern pure silica and not the more chromatic glasses we are interested in (in order to generate the measurement range of our sensor: 1.5 mm of axial chromatism). These change in optical path will then be taken into account when designing the chromatic confocal sensor.

2 IN-CORE GAMMA AND NEUTRON IRRADIATION

We then developed measurement modules to characterize the candidate optical glasses: optical path variations (product of the refractive index of the material under test multiplied by its length) and optical transmission. These measurement modules were then used for on-line measurements at Belgian Reactor 2 in December 2023. Glass samples for online measurements were housed in measurement modules of 9-milimeters in diameter, which collected a signal formed by the interference of reflections from both sides of a parallel-sided glass sample. The measurement modules were located in a temperature-controlled portion (400 mm) of a 5-meter-long needle that has been immersed into the reactor core.

During the entire irradiation process, the temperature measured close to the samples was recorded every minute, along with the gamma dose. The neutron fluence reached at the end of the run was of about $1.5 \times 10^{19}\, n_{fast}\ (> 1MeV)/cm^2$. Interference spectra were collected for samples of Suprasil 1 (synthetic fused silica) and Sapphire at the wavelength of 1220 nm. Performing such an interferometric measurement in a reactor core remains difficult, and because of these difficulties, we were unable to fully test other chromatic glasses due to a loss of signal either during the needle installation or during the irradiation.

3 OPTICAL PATH CHANGE

The relative optical path variations obtained have been corrected for thermal effects, assuming independence of the contribution of variations due to temperature and those due to nuclear radiation. When the maximum reactor power was reached and the temperature stabilized, a clear decrease in the optical path value was observed for Suprasil glass; indicating probable compaction. For Sapphire sample, no significant change was observed.

Post-mortem measurements were also being carried out (and still are) on samples that were in the container in one of the needles during the irradiation campaign. It gave information on samples that were not tested during the irradiation (chromatic glass SF6G05 from SCHOTT manufacturer, for example). Unfortunately, this glass was completely dark (even in the NIR domain), making it useless for the future in-core application confocal chromatic sensor. These additional post-mortem measurements gave information about the compaction of the various samples irradiated and helped in decorrelating variations of refractive index and of length for Suprasil and Sapphire (see Figure 1 for Sapphire samples).

4 OUTCOME

Online measurements ensure that the variations measured are not underestimated due to the annealing phenomenon. To our knowledge, this is the first time that such online measurements have been carried out on glass samples in the reactor core.

Post-mortem and on-line measurement allowed to fully characterize Suprasil and Sapphire sample. Unfortunately, more chromatic glasses cannot be used for the future sensor due to the high RIA. Similarly, diamond cannot be used as a window for the sensor (sealing and protection against corrosive water in PWR conditions). It was therefore decided to use Suprasil to generate the sensor's measurement range (which is a challenge for optical design, since this glass is naturally not that much chromatic). Autoclave tests are also planned for zirconia, another candidate material for the sensor's window.

By combining the results obtained during this irradiation campaign with simulations with optical design tools, we will propose an initial design for a chromatic sensor able to operate in highly radiative environment.

Figure 1: Binocular pictures of about 8,25 mm Sapphire samples, about one year after BR2 irradiation. From top to bottom: control sample, non-irradiated, (SA-7) and irradiated samples (SA-6 and SA-3).

REFERENCES

[1] Minsky, "Microscopy Apparatus", U.S. Patent Ser. NO 695,107, filed 1957.

[2] Girard, "Radiation Effects on Silica-Based Optical Fibers: Recent Advances and Futur Challenges", IEEE Transactions on Nuclear Science, Vol.60, n°3, p. 2015-2036, 2013.

[3] Girard, "Growth and Decay Kinetics of Radiation-Induced Attenuation in Bulk Optical Materials", IEEE Transactions on Nuclear Science, Vol. 65, n°8, p. 1612-1618, 2018.

[4] Primark, "Fast-Neutron-Induced Changes in Quartz and Vitreous Silica", Physical Review, Vol. 110, n°6, p. 1240-1254, 1958.

[5] Cheymol, "High Level Gamma and Neutron Irradiation of Silica Optical Fibers in CEA OSIRIS Nuclear Reactor", IEEE Transactions on Nuclear Science, Vo. 55, n°4, p. 2252-2258, 2008.

Thursday, June 26th

Session #8

Radiation Effects on Fibers

Andrei Goussarov, SCK-CEN

Study of optical fibers luminescence for nuclear reactors power measurement

M. Pouradier Duteil[*], G. de Izarra[*], V. Radulović[**], C. Jammes[***]

[*]CEA, DES, IRESNE, Experimental Physics, Safety Testing and Instrumentation Unit
Cadarache, F-13108 Saint-Paul-lez-Durance, France

[**]Reactor Physics Department
Jozef Stefan Institute, Ljubljana, Slovenia

[***]CEA, DRF, IRFM, Heat Flow and Particle Control Experiments Group
Cadarache, F-13108 Saint-Paul-lez-Durance, France

ABSTRACT

Keywords: Cerenkov Radiation, Optical Fiber Sensors, Nuclear Reactor Monitoring, Point Defects

1 INTRODUCTION

Optical fibers are studied in order to be used as power meters in experimental research reactors. Compton scattering of γ-rays inside an optical fiber leads to electrons being emitted at a speed higher than the speed of light in silica. This effect creates Cerenkov radiation which is propagated by the fiber. Such sensors are of great interest for experimental reactors since they provide a passive measurement, are low intrusive, and are immune to electromagnetic perturbations. Wang et al. demonstrated that there is a linear dependence between the Cerenkov radiated power and the reactor γ flux [1]. Later, Brichard et al. measured that the radiated power at 860 nm and 1060 nm is proportional to the reactor power [2]. For nuclear reactor operating in pulse mode, Peric et al. obtains interesting correlations between the maximum radiated power and the maximum reactor power, as well as between the radiated energy and the energy released by the core [3]. One of the remaining issues for this sensor is the delay between the Cerenkov light signal and the real power trace. This has been studied by Gay et al. on the CABRI reactor for high power transients (more than 10 GW). They highlighted that the time at maximum light intensity depends on the fiber OH concentration as well as the considered wavelength [4]. To improve Cerenkov-based power meters, a new experimental campaign has been performed in the TRIGA-Mark II of the Jozef Stefan Institute (JSI) in order to highlight fiber-related issues of such sensors.

2 EXPERIMENTAL SETUP

A low-OH pure silica core (400 µm in diameter) with a fluorine-doped cladding (20 µm thick) manufactured by ArtPhotonics has been used for this campaign. This fiber was placed in the tangential channel of the TRIGA Mark-II reactor (red dashed line in Fig. 1). One extremity of the fiber was placed at the end of the tangential channel, a few centimeters away from the core.

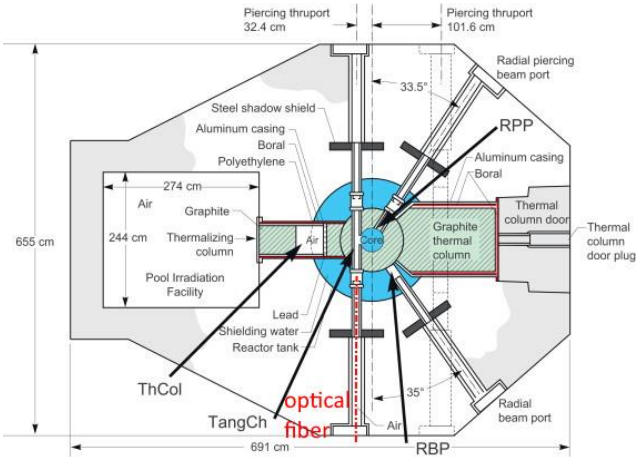

Figure 1 Optical fiber location for luminescence measurement inside the TRIGA of the JSI.

The other extremity was connected to a Hamamatsu single photon avalanche diode (SPAD) in the reactor hall. The quantum efficiency of the SPAD module is optimal in the lower part of the visible spectrum (400 – 600 nm) where Cerenkov light is the most intense. As there are no dopants

in the fiber core, it is assumed that the majority of its radioluminescence comes from the Cerenkov effect.

Each photon detection is associated with a 20ns TTL signal, making the photodiode able to measure luminescence up to 10^8 photons/s. An FPGA module performs the analog-to-digital conversion (TTL to counting rate) and enables the online measurement of Cerenkov radiated intensity.

3 RESULTS AND DISCUSSION

The setup (fiber–SPAD–FPGA) has been used to evaluate the fiber's ability to measure increasing reactor power. Fig. 2 confirms that Cerenkov intensity evolves linearly with reactor power, even considering the whole spectrum and not a single wavelength, which simplifies the setup. Power was increased from zero to 250 kW in 25 kW steps

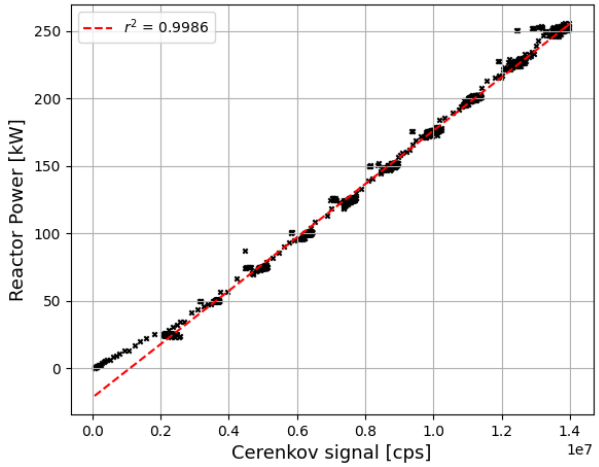

Figure 2 Comparison between Cerenkov light intensity and reactor power during irradiation steps.

Although it seems possible to use an optical fiber as a power meter, this device does not provide a reliable real-time measurement. Indeed, radiated intensity fluctuates during the first minutes of the plateau while the reactor power is stable. This fluctuation, shown in Fig. 3, is more pronounced when the power variation is large. A similar trend was observed by Girard et al. on the transmission of a multimode silica fiber at 780 nm under pulsed X-rays. The signal drop corresponds to point defects creation that reduce transmission, whose kinetics are slower than the Cherenkov response, which is instantaneous [5]. This signal could be explained by point defect creation and a delayed γ signal coming from neutron activation.

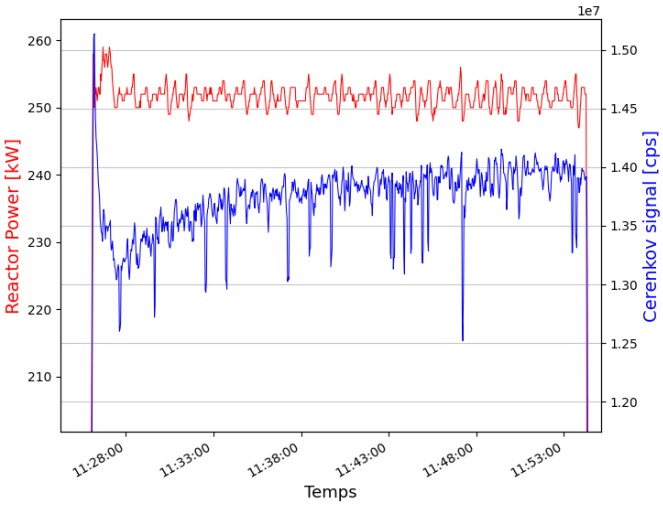

Figure 3 Cerenkov light fluctuation in a 250kW plateau starting from zero power

Bibliographie

[1] Y.-C. Wang, Y.-W. Shi et H.-T. Jiang, *China University of Mining & Technology*, 1991.

[2] B. Brichard, A. F. Fernandez, H. Ooms et F. Berghmans, «Fibre-optic gamma-flux monitoring in a fission reactor by means of Cerenkov radiation,» *Measurement Science and Technology*, vol. 18, 2007.

[3] J. Peric, V. Radulović, L. Barbot et G. D. Izarra, «Radiation measurements in reactor pulse mode at the JSI TRIGA reactor – Power meter based on Cherenkov light intensity measurements,» *EPJ Web of Conferences*, vol. 288, 2023.

[4] G. Gay, A. Gruel, R. Boffy, G. D. Izarra et C. Jammes, «Prompt-critical power excursion measurements with optical fibers in the CABRI experimental reactor,» *Nuclear Instruments and Methods in Physics Research A*, vol. 1067, 2024.

[5] S. Girard, J. Kuhnhenn, A. Gusarov, B. Brichard, M. V. Uffelen, Y. Ouerdane, A. Boukenter et C. Marcandella, «Radiation Effects on Silica-Based Optical Fibers: Recent Advances and Future Challenges,» *IEEE TRANSACTIONS ON NUCLEAR SCIENCE*, vol. 60, 2013.

Temperature Dependence on the Radiation Induced Attenuation of Fluorine-Doped Optical Fibers

Adriana Morana[1], Martin Roche[1], Hugo Boiron[2], Gilles Mélin[2], Emmanuel Marin[1], Youcef Ouerdane[1], Aziz Boukenter[1], Thierry Robin[2], Sylvain Girard[1,3]

[1]Laboratoire Hubert Curien, Université Jean Monnet Saint-Etienne, Saint-Etienne, France
[2]Exail, Lannion, France
[3]Institut Universitaire de France, Paris, France

ABSTRACT

This work focuses on the irradiation temperature (-80°C, room temperature) effects on the radiation induced attenuation (RIA) of a prototype polyimide coated F-doped optical fiber, from the visible to IR spectral range. We highlight the contribution of unstable point defects absorbing at different wavelengths at both temperatures.

PACS Keywords: Optical Fiber, Radiation Induced Attenuation, Temperature

1 INTRODUCTION

Optical fibers (OFs) are more and more employed in harsh environments, characterized by radiations, extreme temperatures, and sometimes also the presence of gases, as space, nuclear power plants, nuclear waste repositories [1]. Radiations generate defects in the OF silica matrix and their absorption bands increase the OF attenuation, known as RIA. RIA depends on the several parameters linked to environment (dose, dose-rate, temperature, …), the OF itself (composition, manufacturing conditions, treatment, …) and also its profile of use (injected signal power and wavelength) [2]. Pure Silica Core (PSC) or F-doped fibers are known to be the most resistant under steady state radiations [2]. However, the manufacturing process can negatively influence the radiation response of this class of fibers; indeed, we observed that an Ultra-Low Loss (ULL) PSC OF, characterized by an intrinsic attenuation at 1.55 µm lower than 0.16 dB/km, is very radiation sensitive, with an IR-RIA exceeding the one of the radiation sensitive P-doped fibers. Its RIA was shown to be strongly dependent on the irradiation conditions and on the injected signal power [3]. Another parameter that affects significantly the radiation response is the irradiation temperature, since it will influence the defects generation and recombination efficiencies [4]. We have already investigated the temperature effects in the IR spectral region on Ge- or F-doped single-mode (SM) OFs, demonstrating that the RIA at 1.55 µm increases from room temperature (RT) to -80°C by a factor 20 for the Ge-doped fibers at 10 kGy (dose-rate being of 0.6 Gy/s) [5] and only 4 for the F-doped OFs up to 100 kGy (with a dose-rate of 6 Gy/s) [6]. In this paper, we investigate the radiation and temperature combined effects on another variant of F-doped SM fiber with a polyimide coating in the spectral range from the visible to the IR, under X-rays up to 100 kGy(SiO_2).

2 MATERIAL AND METHODS

The fiber under test F-doped SM OF, manufactured by Exail and having a polyimide coating. The irradiations were performed at the IdefiX X-ray irradiator of the Laboratoire Hubert Curien (Saint Etienne, France), having a X ray tube with a target in tungsten operating at 100 kV tension to deliver photons with a mean energy fluence of 40 keV. The dose-rate was set at ~6 Gy(SiO_2)/s and the total ionizing dose (TID) at 100 kGy(SiO_2). A heating/cooling plate (Instec HCP204SC) allows varying the irradiation temperature, in our study between RT (~25°C) and -80°C. RIA measurements were performed by acquiring the OF transmission with a halogen source and a spectrometer, in the visible (QE95000) or in the NIR range (NIRQUEST), from Ocean Optics. The acquisition time was ~500 ms. The sample under test was connected to the acquisition system, thanks to two F-doped radiation-resistant fibers shielded from the X-rays with lead plates.

3 RESULTS AND DISCUSSION

Fig. 1 and 2 illustrate the RIA kinetics at two wavelengths representative of the visible and IR ranges: 600 nm and 1550 nm.

At -80°C, the RIA at 600 nm increases monotonically, but at 1550 nm it quickly increases up to 73 dB/km just at the irradiation start (the maximum is reached at a dose of 10 Gy, just few seconds after the irradiation start), then decreases down to ~40 dB/km and starts increasing again more slowly for doses higher than ~30 kGy. At both wavelengths, after the irradiation end, while keeping the temperature still at -80°C, the RIA recoveries quickly by ~96% at 600 nm and ~77% at 1550 nm in only one hour,

indicating that most of the observed losses are due to unstable defects.

At RT, the RIA at 1550 nm increases monotonically, reaching at the maximum TID a value of only 8.8 dB/km (against ~43 dB/km at low temperature); whereas at 600 nm the RIA presents a peak at a dose of 6 kGy. At the irradiation end, the RIA is less than 1000 dB/km, ~16 times lower than at -80°C.

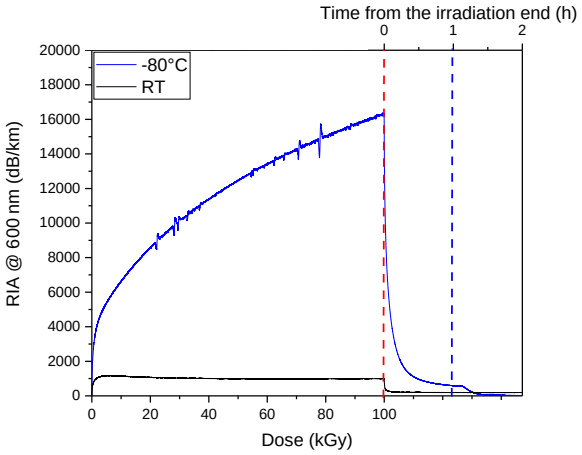

Figure 1: RIA kinetics at 600 nm as a function of the dose (or time) at two irradiation temperatures: -80°C (blue curve) and 25°C (black curve). The red and blue vertical dashed lines indicate, respectively, the irradiation end and the temperature returning at RT.

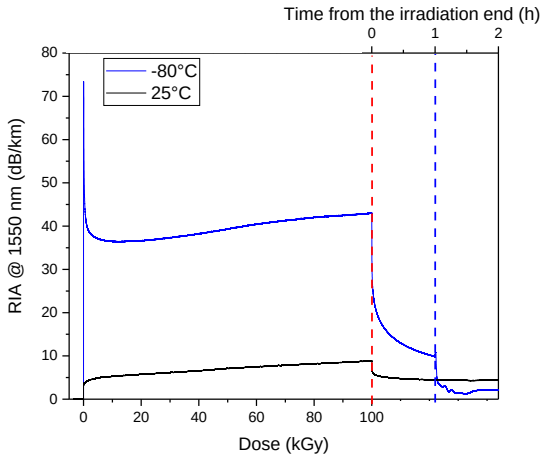

Figure 2: RIA kinetics at 1550 nm as a function of the dose (or time) at two irradiation temperatures: -80°C (blue curve) and 25°C (black curve). The red and blue vertical dashed lines indicate, respectively, the irradiation end and the temperature returning at RT.

These two behaviors observed under radiations let us suppose the presence of unstable defects, that quickly recombine or convert into another center absorbing at a different wavelength. To discuss the possible origins, Fig. 3 reports the RIA spectra at the maximal accumulated dose (100 kGy) and at the dose corresponding to the maximal RIA at 600 nm for the RT irradiation and at 1550 nm for the one at -80°C. At -80°C, the unstable defects absorb around 1500 nm. A very strong IR absorption band associated with unstable defects has already been identified in ULL PSC fibers; however, in that case it was centered around 1310 nm and has been hypothetically related to some variants of Self Trapped Holes (STHs) [3]. The band shift observed for this sample could be linked to the different cutoff wavelength or to a different stress profile inside the OF. At RT, a large band centered around 700 nm is present and this could be associated with the STH absorption bands centered at 660 nm and 760 nm [2]. For the conference, the spectral decomposition will be performed in order to well identify the involved centers and verify if these visible bands associated with STHs are present or not also at -80°C.

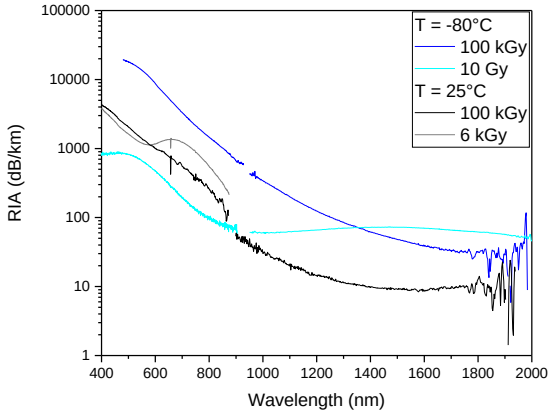

Figure 3: Spectral RIA at -80°C and RT (blue and black lines, respectively) at 100 kGy (darker line) and at the dose of the RIA maximum (lighter line): 10 Gy at -80°C and 6 kGy at RT.

4 CONCLUSION

In this abstract, we investigated the RIA of a F-doped fiber in a large spectral range (from the visible to the IR) at two irradiation temperatures, -80°C and RT, for TID up to 100 kGy, with a high dose-rate of 6 Gy/s. These tests highlighted the presence of unstable defects at both low and room temperatures. The spectral decomposition that will be performed for the conference will allow to better identify the radiation-induced centers. It is still worth noticing that the investigated dose-rate is very high for most of the harsh environments. At lower dose-rate the transient RIA associated to the unstable defect should be lowered in this fiber. This aspect will be investigated for the final paper and symposium, too.

REFERENCES

[1] S. Girard et al., *IEEE Trans. Nucl. Sci.*, vol.60, no. 3, pp. 2015 - 2036, 2013.

[2] S. Girard et al., *Rev. in Phys.*, vol. 4, Article no. 100032, 2019.

[3] A. Morana et al., Sensors, vol. 20, no. 24, Article no. 7254, 2020.

[4] S. Girard, et al., *IEEE Trans. Nucl. Scie.*, vol. 60, no. 6, pp. 4305–4313, Dec. 2013.

[5] A. Morana et al., *IEEE Trans. Nucl. Sci.*, vol. 69(3), pp. 512 – 517, 2021.

[6] A. Morana et al., *IEEE Trans. Nucl. Sci.*, vol. 70(4), pp. 549-555, 2023.

Combined Temperature and Photobleaching Effects on P-doped Optical Fibers

Allan Travailleur[1], Sylvain Girard[2,3], Martin Roche[4], Marie-Noëlle De Noifontaine[1], Nadège Ollier[1], Antonino Alessi[1,5]

[1]Laboratoire des solides irradiés, CEA/DRF/IRAMIS, CNRS, École Polytechnique, Institut [2]Laboratoire
[2]Hubert Curien, CNRS, Université Jean Monnet, 42000 St-Etienne, France
[3]Institut Universitaire de France, Paris, France,
[4]Polytechnique de Paris, F-91128, Palaiseau, France
[5]Department of Physics and Chemistry Emilio Segrè, University of Palermo, Via Archirafi 36, 90123 Palermo, Italy

ABSTRACT

In this paper we focus on the combined temperature (-80°C to +80°C) and the photobleaching process on the radiation induced attenuation (RIA) of multimode P-doped fibers. In particular, we investigated the behavior of the optical absorption spectra in the visible range (of 450-800 nm) after irradiation and laser injection in the fiber.

PACS Keywords: Photobleaching phenomenon (PB), Radiation Induced Attenuation (RIA), Phosphosilicate optical fiber, Phosphorous point defects, Dosimeter.

1 INTRODUCTION

Phosphorous-doped silica is known to play a key role in various domains. For instance, it can be incorporate in telecom fibers to increase the refractive index of the silica or as a co-dopant to avoid clustering of rare earths in amplifier fibers. In addition, Phosphorous in silica induces a higher radiation sensitivity compared to the other fiber composition (Ge, F, PSC…). As a consequence, using P dopant enables to design dosimeters based on optical reflectometry (OTDR) providing spatially-resolved dose mapping [1].
Nowadays, P-doping is then widely used for the production of specialty radiation sensitive optical fibers, optimized to measure the dose of radiation through the radiation induced attenuation (RIA) phenomenon. So, a great deal of research has been carried out on their radiative response, particularly in the near infrared (NIR) and visible region. This research on P doped OFs has resulted in a reliable dosimetry tool operating in NIR. In fact, thanks to these researches this material can provide linear dose response up to 500Gy. For a reliable dosimeter, RIA needs to be independent of the dose, dose rate (lower than <10Gy/s for nIR region), the temperature range (-80 to 120°C) and with different type of particle (X, ɣ, e-...) [2]. For this reason these systems are widely used in large facilities such as CERN [1] and in harsh environments such as nuclear or space, which are subject to extreme conditions of radiations. As for all the silica types, even for P doped silica, ionizing radiation causes the degradation of the optical properties, mainly due to point defects generation and drive the RIA. While in the IR the optical features and dosimetry applications are many due to the P1 defects [1,2,3], in the visible range the main point defect investigated seems to be the phosphorus oxygen hole center (POHC) [3,4]. In ref. [4] it was suggested that there are two types of POHC, the stable POHC (constituted by an unpaired electron located on a non-bridging oxygen atom) and the metastable POHC (in which the unpaired electron is shared by two non-bridging oxygen atoms) [4]. Both are responsible for the high radiation sensitivity (over 100 $dBkm^{-1}Gy^{-1}$) [5] where P-doped fibers exhibit linear response and could serve as dosimeter. One limitation is that at a certain point, the RIA overcomes the dynamic of the acquisition chain and it is becoming necessary to change the fiber or to regenerate it in order to reset the sensor. This second option is available, in fact, the injection of a well-adapted laser light allows to reset the transmission capacity of the fiber through the photobleaching mechanism while maintaining its dosimetry properties at room temperature [2]. So, studying the evolution of the RIA signal under laser illumination can provide further information on the PB mechanism allowing to optimize the regeneration procedure. However, despite different investigation on the PB, the effect of temperature on this mechanism is still not sufficiently unexplored.

2 METHODS

We studied a multimode P-doped optical fiber manufactured by Exail with two levels of phosphorous doping in its core, for each experiments we used samples with lengths of 3 meters. For radiation test we use the X-ray irradiation facility named LabhX from Hubert Curien Laboratory in St-Etienne. This irradiator is an X-ray tube operated at 100kV (with a mean photon energy of 40 keV) allowing homogeneous irradiation from low dose rates (500µGy) to high dose rates (>6Gy/s). This facility is

equipped with a temperature controlled plate (Instec HCP204SC) which allows the control of irradiation temperature in the range of -120°C to +400°C. To ensure maximum dose homogeneity, samples are prepared in monolayer spiral. To measure the visible RIA, the set-up is equipped with a halogen-deuterium white light source (DH2000 from Ocean Optics), a visible spectrometer (Ocean Optics) and a 408nm laser of 4mW. Samples are spliced to radiation hardened transport fibers (doped with fluorine) which are used to connect the sample under test to the instrumentation outside the LabHX. In the first experiments, each sample was irradiated at the total ionizing dose (the energy deposited per unit mass by ionizing radiation) of 5Gy(SiO_2) with a dose rate of 10 mGy/s. Several irradiation temperatures (T_{irr}) within the range of (-80 to 80°C) have been studied. Before to inject the laser we studied a recovery of 20 minutes at the irradiation temperature. After this stage we performed 1 hour of PB at the same irradiation temperature. The laser injection was performed with the same experimental set-up reported in ref [2] which allows avoiding to move the fiber, but that does not allow to record the transmission spectrum during the laser injection. Then, the transmission was monitored during two recovery-step. The first takes place at the irradiation temperature (1 h) while the second one occurs at room temperature (25°C). An example is shown in **Fig1**. During a second set of irradiations we highlight the effect of the PB duration by varying it (1, 10, 20 and 60 minutes) at room temperature (25°C).

3 RESULTS

Fig1 illustrates as example the experiment time sequence with an example of the run performed at T=-40°C. **Fig2**, is an example of experimental results performed at T_{irr} (+80, 0, -80°C). These data allow to study the influence of temperature on the PB mechanism monitoring by the RIA signal. Above 600 nm, there is almost no recovery while below 600 nm, higher the T_{irr}, the more is reduced the RIA after 5 Gy dose. In fact, **Fig2A** shows that 1) higher is the irradiation temperature lower is the RIA, 2) a recovery of the signal takes place at all the temperature and 3) higher is the temperature higher is the recovery after the irradiation. In all the fibers the RIA after PB is very similar in shape and intensity. The residual RIA has the shape of a band peaked at about 550 nm, which remains very stable for the combination of PB and temperature investigated. As a consequence, we can guess that the stable POHC are still present in the fiber, while the strong bleaching at shorter wavelength suggest the destruction/conversion of metastable POHC and of another defect called P2, which can affect the investigated spectral range with the tails of their absorption bands in the UV. **Fig2B** shows that, after the end of the laser injection minor, but detectable, processes take place both at the T_{irr} and at room temperature. In fact, all the RIA feature a slow re-increase. Small differences are observed that can be explained either by small defect kinetics or by some changes in attenuation related to the effect of varying the temperature on the light guiding properties in our multimode optical fibers. A second type of experiments was performed as a function of the PB duration (1, 10, 20, 60 min). This experiment illustrates the efficiency of PB mechanism by changing the duration of PB to see the effect on the RIA signal recovery. Basing on a preliminary analysis the most of the recovery occurs during the first 10 minutes of PB, which is consistent with the work of Martin Roche in [5].

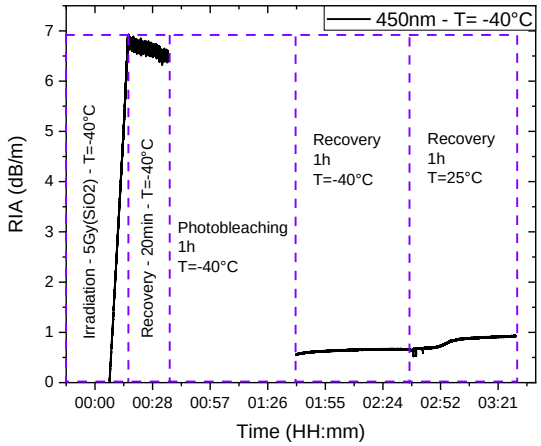

Figure 1: Set-up of the different steps of experiments

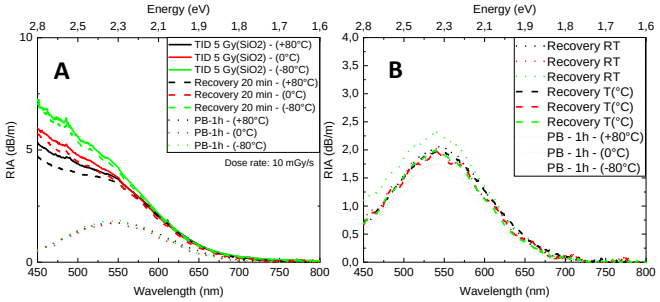

Figure 2: a) RIA spectra at different temperature, irradiated up to 5 Gy, after recovery and after PB; b) RIA spectra recorded during the last two recovery steps.

REFERENCES

[1] G. Li Vecchi *et al.*, *Opt. Lett.*, vol. 45, nº 18, p. 5201, sept. 2020.

[2] D. Di Francesca *et al.*, *physica status solidi (a)*, vol. 216, nº 3, p. 1800553, 2019.

[3] S. Girard *et al.*, *Reviews in Physics*, vol. 4, p. 100032, nov. 2019.

[4] D. L. Griscom et al, *Journal of Applied Physics*, vol. 54, nº 7, p. 3743-3762, juill. 1983.

[5] M. Roche *et al.*, *J. Lightwave Technol.*, vol. 42, nº 9, p. 3416-3422, mai 2024.

Thursday, June 26th

Session #9

Polarization maintaining optical fibers

Laurent Lablonde, Exail

From the micro- down to nanostructuration: an access to new polarisation-maintaining silica based optical fibres

Monika Bouet[1*], Alicja Anuszkiewicz[2,4], Adam Filipkowski[2], Damian Michalik[2], Andy Cassez[1], Géraud Bouwmans[1], Ryszard Buczynski[2,3]

[1]Univ. Lille, CNRS, UMR 8523-PhLAM-Physique des Lasers, Atomes et Molécules, F-59000 Lille, France
[2]Institute of Microelectronics and Photonics, IMiF, al. Aleja Lotnikow 32/46, 02-668 Warsaw, Poland
[3]Institute of Geophysics, University of Warsaw, ul. Pasteura 5, 02-093 Warsaw, Poland
[4]Warsaw University of Technology, Pl. Politechniki 1 00-661 Warsaw, Poland

ABSTRACT

Herein we present a concept and development of new silica optical fibers based on the nanostructuration of the core. This concept permits to induce some new or non-achievable by other techniques properties, such as construction of defined gradient for the GRIN lenses, a birefringence without application of SAP or the multi-material mixing for free-form fiber optics. In this paper, we will describe the design, the manufacturing and the characterization of polarization-maintaining optical fiber with circular core without stress-applying parts (SAP). This approach enables the integration with telecom fiber by the circular design and moreover, permits the construction of multicore polarization maintaining fiber optics.

PACS Keywords: nanostructuration, polarization maintaining optical fibers, silica doped materials, birefringence.

1 INTRODUCTION

The ability to shape the refractive index of silica-based optical fibres is a crucial challenge for flexible engineering, enabling new applications and innovative optical fibre designs. Recently, a method of stacking hundreds of capillaries made from pure and doped silica has been demonstrated to obtain fibres with a gradient index [1,2]. This approach, known as nanostructuring, is based on the Maxwell-Garnett approximation of effective medium theory, as the size of each element in the fibre core decreases to the nanometric scale [3]. Nanostructuring provides access to a myriad of structures with circular and non-circular symmetry and enables the creation of enriched passive and active element-doped fibre designs. Additionally, it allows for the induction of optical properties such as birefringence.

The development of fully solid polarisation-maintaining (PM) fibres was established in the early 1980s [4] and has not shown many evolution since. Commercially available PM fibres typically rely on stress-induced birefringence or core ellipticity, representing a compromise between polarisation-maintaining functionality and compatibility with telecommunications systems in terms of optical and mechanical properties. However, PM fibres with stress-applying parts (SAPs) in the cladding are impractical for multi-core fibre creation, as SAPs can lead to much larger cladding diameters than those of optimal single-mode fibres. This limitation is incompatible with the concept of multi-core fibres, where efficient stacking and packaging of multiple cores in a minimal volume with negligible cross-coupling between cores is crucial. Moreover, the application of stress applying parts in PM fibres induces the application of materials with a different coefficient of thermal expansion (CTE), which makes this fibre sensitive for temperature change and torsions. Consequently, a new PM fibre concept is needed to overcome these difficulties for applications in for instance, multi-core fibres or temperature insensible ones.

2 CONCEPT OF NANOSTRUCTURATION

The concept of nanostructuration of the core of optical fibre is based on Maxwell-Garnett approximation of Effective Medium Theory (EMT) [ref. 3, 5] in which is assumed that doped region of silica materials can be treated as discrete inclusions within a continuous silica matrix. As long as the inclusion size is inferior that the wavelength propagated in the core of optical fiber, the effective refractive index ε_{eff} of those materials can be calculated owing to EMT (see Equation 1).

$$\varepsilon_{eff} = \varepsilon_m \frac{\varepsilon_i(1+2\delta)+\varepsilon_m(2\delta-2)}{\varepsilon_m(2-\delta)+\varepsilon_i(1-\delta)} \qquad (1)$$

Where:

δ – relative proportion of high index material ε_i

ε_i – high refractive index of doped silica

ε_m – refractive index of milieu

This approach simplifies modelling of light-matter interactions in complex nanoscale geometries.

3 RESULTS

The first results were obtained on the development of new polarization-maintaining fibres without any stress-applying parts (SAPs), with an original structure based on an anisotropic pattern induced in the fibre core [6]. The latter structure has different effective refractive indices in directions perpendicular (maximum) and parallel (minimum) to the applied patterns (Fig.1).

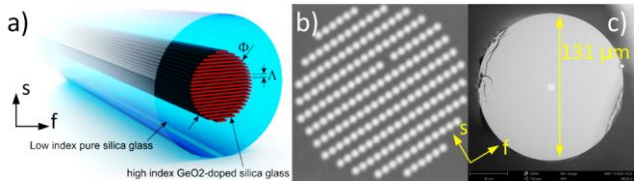

Fig. 1 (a)The design of ZEBRA fiber, (b) the pattern in ZEBRA fibers (7 x7 µm), (c) general view of fiber with dimension.

3.1 Engineering of the design of core and birefringence studies

In order to validate this concept and improve the birefringence properties of single mode optical fibers, another type of inclusions with fluorine doping was added [7]. This material – F-doped silica rods - enables to decrease the refractive index (RI) od silica and by consequence, create the higher gap between high- and low-RI silica doped glasses, and therefore create the contrast of RI in the core of optical fibers (Fig. 2).

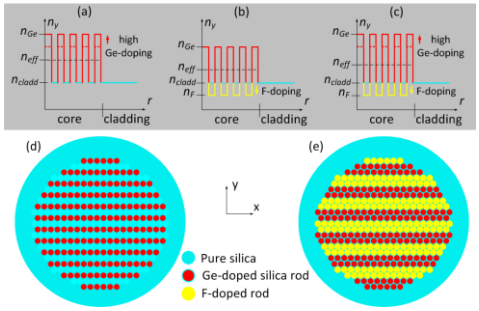

Fig. 2 The scheme of engineering of the pattern in ZEBRA fibers.

	ZEBRA #1	ZEBRA#2	PANDA
Optical losses	0.22 dB/m	0.14 dB/m	0.5-5 dB/km
Birefringence	0.55×10^{-4}	0.74×10^{-4}	5.0×10^{-4}
PER	20 dB	19 dB	23 dB

Table 1: Optical and polarization properties of obtained fibers.

4 CONCLUSION

In this paper we presented a new concept of nanostucturation of the optical fibre cores, which gave us an access to novel polarization maintaining fibers. This concept was validated in case of single mode - single core fibers and will be extended on multi-core fibres or the bundles of OF, which are in perspective to this project.

5 ACKNOWLEDGEMENTS

Authors would like to acknowledge “PHC POLONIUM” program (project number: 51015TM), funded by the French Ministry for Europe and Foreign Affairs, the French Ministry for Higher Education and Research and the Polish NAWA Agency. This work was partially supported by the FiberTech Lille technological platform (https://fibertech.univ-lille.fr/fr/) and IRCICA (UAR 3380) Institute.

REFERENCES

[1] R. Buczyński, M. Klimczak, T. Stefaniuk *et al.* "Optical fibers with gradient index nanostructured core" Opt. Express 23, 25588-25596 (2015).

[2] A. Anuszkiewicz, R. Kasztelanic, A. Filipkowski et al. „Fused silica optical fibers with graded index nanostructured core”.Sci Rep 8, 12329 (2018).

[3] A. J. Waddie, R. Buczynski, F. Hudelist, *et al.* “Form birefringence in nanostructured micro-optical devices,” Opt. Mater.Express, vol. 1, no. 7, pp. 1251-1261, (2011).

[4] J. Noda, K. Okamoto and Y. Sasaki, "Polarization-maintaining fibers and their applications," in *Journal of Lightwave Technology*, vol. 4, no. 8, pp. 1071-1089 (1986).

[5] Michalik, D., Stefaniuk, T., *et al.* “PM optical fibers with an anisotropic core compatible with the SMF-28 standard”, JOSA B, 2020, 37(6), pp.1722-1728.

[6] A. Anuszkiewicz, M. Bouet, D. Michalik et al. "All-solid polarization-maintaining silica fiber with birefringence induced by anisotropic metaglass" Opt. Lett. 47, 401-404 (2022).

[7] A. Anuszkiewicz, M. Bouet, A. Filipkowski, *et al*, "Birefringence Engineering in Nanostructured ZEBRA Fiber," J. Lightwave Technol. 42, 4959-4965 (2024).

Radiation Induced Attenuation of Space-grade Polarization-Maintaining Optical Fibers in the UV-Visible Domains

Boiron H. [*], Villedieu T. [*], Bergont M. [*], Morana A. [**], Steib A. [*], Robin T.[*], Girard S.[**,***]
[*]Exail, rue Paul Sabatier, 22300 Lannion
[**] Laboratoire Hubert Curien, Université Jean Monnet
18 Rue Professeur Benoît Lauras, 42000 Saint-Étienne
*** Institut Universitaire de France

ABSTRACT

We investigate the radiation-induced attenuation (RIA) in a Panda polarization-maintaining optical fiber optimized to ensure single-mode operation in the visible spectrum. The fiber was subjected to steady state X-rays runs up to 3 kGy(SiO_2), with variations in temperature and dose rate. Spectral analysis of the RIA was conducted, and a Gaussian decomposition model was employed to identify and characterize the predominant radiation-induced color centers impacting this spectral domain.

PACS Keywords: UV-Visible, RIA, Gaussian deconvolution, PM-Fiber, PSC-Fiber

1 INTRODUCTION

The deployment of photonic technologies in radiation-rich environments such as space missions, high-energy physics experiments, and nuclear facilities necessitate the development of components with high radiation tolerance. Considerable progress has been made in recent years toward radiation-hardened laser diodes [1-4]. These advances have enabled the miniaturization and increased reliability of photonic systems for critical applications including satellite-based communication, radiation sensing, and quantum technologies. However, the overall performance and longevity of such systems rely not only on the active components but also on the passive optical elements that interconnect and condition the signal propagation. Among these, polarization-maintaining (PM) fibers are essential when preserving the state of polarization is critical, such as in interferometric setups, laser diode pigtailing, RGB optical component integration, and compact UV light sources.

When exposed to ionizing radiation, optical fibers can exhibit RIA due to the formation of point defects or color centers [5]. The use of pure silica core (PSC) fibers for UV-Visible applications means that they are expected to be relatively tolerant to radiation. However, the radiation effects on fibers in the UV spectral range remains poorly studied compared to the visible [6] and infrared [7] domains.

In this work, we present an in-depth investigation of the radiation response of a high-performance PM fiber optimized for the visible range. The fiber was subjected to 40 keV X-rays under controlled conditions, with a systematic evaluation of the spectral RIA as a function of temperature and dose rate until a total ionizing dose (TID) of $3kGy$. Beyond attenuation measurements, we propose a spectral deconvolution model based on Gaussian fitting to identify and characterize the point defects impacting this spectral domain. This approach provides valuable insights into the physical mechanisms responsible for PSC fiber degradation in the UV-visible domain and supports the development of radiation-hardened optical components.

2 MATERIAL AND METHOD

2.1 Sample tested

To operate in the UV-Visible range, the fiber composition must be adapted, and no longer uses germanium as the core dopant, too much absorbing in the UV [8]. To ensure the signal propagation, the fiber core is made of pure silica, while the cladding refractive index is lowered by adding fluorine. The fiber core size is set at 2.1 μm to ensure single-mode operation at 375 nm with a cut-off wavelength below 350 nm. Borosilicate stress rods ensure stress anisotropy and thus the appearance of a slow and a fast axis to maintain polarization.

2.2 Experimental Design

A white light source (DH 2000 BAL) was employed and a visible spectrometer (QE PRO, Ocean Optics) served as the detector. The same PM-SC-375 fiber is used as transport fiber to minimize losses and enhance repeatability.

N°	T ($°C$)	Dose Rate (mGy/s)	TID (kGy)
1	25	{5* ; 40 ; 200}	3
2	{-40 ; 25** ; 80}	50	1

Table 1: Experimental Design (* $TID = 1.25\ kGy$ for 5 mGy/s ; **Dose rate $= 40\ mGy/s$ for $T = 25\ °C$)

The irradiation took place within the LabhX X-ray facility at Lab. Hubert Curien operated at 100 kV. The fiber sample is wound in a monolayer coil and placed on a thermal

plate. The characterization campaign was carried out in two stages, as summarized in Table 1.

3 EXPERIMENTAL RESULT

3.1 Dose rate dependence

In most cases, radiation tests can be considered accelerated. Indeed, for space applications, it is almost impossible to reproduce such low dose rates on Earth while maintaining the same TID. It is therefore important to verify that these accelerated tests are worst-case scenarios, as shown at other wavelengths for pure silica fibers [9]. Figure 1 shows the RIA at 375 nm for 3 different dose rates {5 ; 40 ; 200} mGy/s at fixed temperature (25 °C) of the PM fiber.

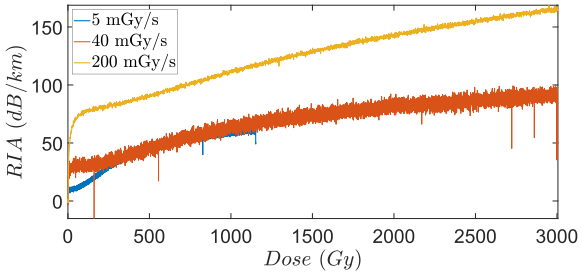

Figure 1: RIA @ 375 nm for 3 different dose rates {5 ; 40 ; 200} mGy/s at fixed temperature (25°C)

The measurement at 40 mGy/s is slightly noisier, as the fiber length used was shorter than for the other dose rates. The RIA at 375 nm increases (non-linearly) with dose rate during irradiation. The final paper will show that this is related to metastable defects contribution while the contribution of RT stable defects does not depend it. In addition, we will examine what happens below 500 Gy, where the RIA increases rapidly

3.2 Temperature dependence

To continue characterization, it is important to test the radiation effects at different temperatures. For space , the temperature range can be significant. Figure 2 illustrates the temperature effect on the RIA at 375 nm for 3 different temperatures {-40 ; 25** ; 80}°C at fixed dose rate (40 mGy / s, **50 mGy/s) for the PM fiber. The RIA is multiplied by 4 when the temperature decreases from 25 °C to -40 °C. We will show that this is due to the temperature dependence of the metastable color centers.

3.3 Gaussian decomposition of defects

Finally, Figure 3 shows a Gaussian decomposition of the RIA of the PM fiber after a dose of 3 kGy at 200 mGy/s. This Gaussian decomposition was based on previous work in the literature regarding the optical absorption bands of defects [5,6].

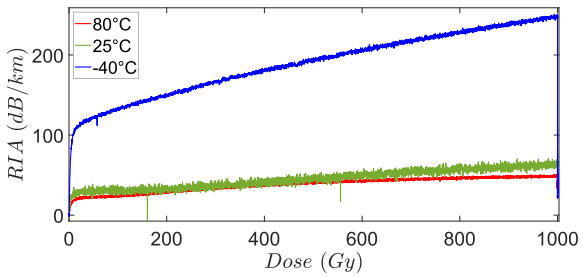

Figure 2 : RIA @ 375 nm for 3 different temperatures {-40 ; 25** ; 80} °C at fixed dose rate (40 mGy/s, **50 mGy/s)

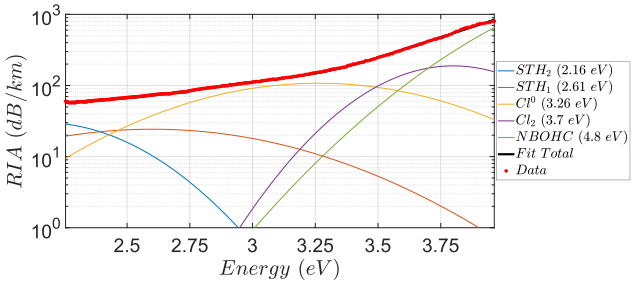

Figure 3: Gaussian decomposition of the RIA of the PM-SC-375 fiber after a dose of 3 kGy at 200 mGy/s

A systematic study of the growth and recombination of the identified defects during the 6 experiments from Table 1 will be proposed in the final presentation.

4 CONCLUSION & PERSPECTIVES

In conclusion, we have characterized the RIA levels and kinetics on a PM fiber adapted to operate in the UV-Visible range, as well as the related influence of temperature and dose rate. A decomposition using a set of known Gaussian optical absorption bands of SiO_2-related defects responsible is also proposed. In the final version, the results will be studied in greater depth and the impact of radiation on the PM properties of the fiber will be discussed.

REFERENCES

[1] C. Phifer, Effects of Radiation on Laser Diodes., 2004.
[2] L. Weninger *et al.*, Electronics 12 (2022) 81.
[3] A. H. Johnston *et al.*, IEEE Trans. Nucl. Sci. 51 (2004) 3564–3571.
[4] M. Li *et al.*, Applied Physics Reviews 11 (2024) 021315.
[5] S. Girard *et al.*, Reviews in Physics 4 (2019) 100032.
[6] C. Campanella *et al.*, Applied Sciences 11 (2021) 2991.
[7] A. Morana *et al.*, IEEE Transactions on Nuclear Science 70 (2023) 549–555.
[8] J. Simpson *et al.*, MRS Proc. 61 (1985) 333.
[9] T. Wijnands *et al.*, J. Lightwave Technol. 29 (2011) 3393–3400.